UNIVERSITAT POLITÈCNICA
DE CATALUNYA
BARCELONATECH

Hot forming behavior of ni-base superalloys and their modeling

UtkuDeniz Ozturk

Universitat Politècnica de Catalunya

Hot Forming Behavior of Ni-Base Superalloys and their Modeling

UtkuDeniz Ozturk

Thesis advisors:
Prof. Dr. Jose Maria Cabrera Marrero
Assoc. Prof. Dr. Jessica Calvo Muñoz
Prof. Dr. Abdelkrim Redjaïmia

Barcelona, 2019

to my family, friends and professors...

Abstract

Numerical and experimental simulation of engineering materials has been an emerging topic for recent decades. Reliable and efficient numerical simulations are only possible through correct and pragmatic modeling approaches. This Ph.D. work is focused on understanding and modeling the hot forming behavior of polycrystalline superalloys. In other words, this is an attempt to comprehend and model the deformation characteristics and microstructural evolution of these alloys during hot forming.

Understanding the hot forming behavior of such alloys is of interest from an industrial perspective due to the fact that the service performance is highly dependent on the final microstructure while the final microstructure is affected by many processing parameters, such as solutionizing time/temperature, deformation rate/temperature or existence and length of dwell time between processing steps.

Within the scope of the current work, a recently developed Allvac 718Plus® is studied. The first part addresses the modeling of flow curves obtained through uniaxial hot compression tests at different temperatures and strain rates. The second part is dedicated to the multiscale characterization of the precipitation behavior and the dislocation-precipitation interaction in Allvac 718Plus®. Apart from uniaxial hot compression tests, stress relaxation tests and various characterization methods such as optical, scanning and transmission electron microscopy are implemented.

Acknowledgements

I would like to express my gratitude to my main supervisors Dr. Jose Maria Cabrera Marrero and Dr. Jessica Calvo Muñoz who welcomed me in Barcelona and gave me the opportunity to fulfill this thesis work. In addition to this, I would like to thank Dr. Abdelkrim Redjaimia for providing me the opportunity to perform a big part of the characterization work at his laboratory within the University of Lorraine.

During this thesis work, although there were rises and falls, I have had amazing time and I have equipped myself with different engineering skills. In this respect, I would like to thank to Dr. Flavio Soldera, for introducing me to the DocMASE world.

This work has been conducted with the financial support of European Union Erasmus Mundus early stage researcher grant. I sincerely acknowledge this support and would like to express my thanks to DocMASE school as well.

I would like to thank Dr. Hugo Guajardo Martinez of Frisa Forgings S.A. (Mexico) who supplied the material.

I also appreciate the help and support provided by Anna Hernandez.

My unreserved thank you goes to Wang Lei for numerous fruitful discussions, for the good time spent in china towns. And discussions with Dr. Pedro Paramo and again, the good time spent are greatly appreciated.

Contents

Abstract i

Acknowledgements iii

List of Figures xv

List of Tables xvii

1 Introduction 1
- 1.1 Brief History of Superalloys . . . 2
- 1.2 Motivation and Focus of the Current Work . . . 3
- 1.3 Overview of Superalloys Strengthened by Ordered γ' Particles and Carbides . . . 4
  - 1.3.1 Introduction . . . 4
  - 1.3.2 Carbides . . . 5
  - 1.3.3 Crystallography . . . 5
  - 1.3.4 Lattice Mismatch . . . 6
- 1.4 Alloy ATI 718Plus® . . . 7
  - 1.4.1 Introduction . . . 7
  - 1.4.2 Development & Chemistry . . . 8
  - 1.4.3 Phases . . . 9

2 Physical Processes Occurring During Hot Forming 13
- 2.1 Compression Tests and Flow Curve . . . 14
- 2.2 Work Hardening and Dynamic Recovery . . . 15

2.3 Dynamic Recrystallization 17
2.3.1 Nucleation of DRX 22
2.4 Other Physical Processes 26
2.4.1 Deformation Induced Precipitation 26
2.4.2 Interaction between Dynamic Recovery & Precipitation 28
2.4.3 Interaction between DRX & Precipitation 29
2.4.4 Behavior of Dislocations upon Facing a Precipitation in γ' Strengthened Alloys 30

3 Experimental Methods, Characterization and Equipment 35
3.1 Thermomechanical Treatment 36
3.1.1 Uniaxial Compression Tests 36
3.1.2 Processing Route 38
3.1.3 Equipment for Compression Testing 42
3.1.4 Cylindrical Samples for Compression Testing and Received 718Plus Billet 47
3.2 Characterization Methods 48
3.2.1 Microhardness Measurements 48
3.2.2 Microscopy Observations 49

4 Modeling of High Temperature Deformation 57
4.1 Dislocation Density Based Hardening Models 58
4.1.1 The Bergstrom Model 59
4.1.2 The Kocks Model 63
4.1.3 The Roberts Model 64
4.1.4 The Estrin - Mecking - Bergstrom Model 65
4.1.5 Accounting for The Effect of the Second Phase Particles 69
4.2 Kinetic Equations of Hot Forming 72
4.3 Modeling Dynamic Recrystallization 74
4.3.1 Avrami Model as a Representation of DRX Kinetics 76

5 Baseline Hot Flow Study of Allvac 718Plus® 79
5.1 Initial Analysis of the Batch Received for this Study . . 79
5.2 Solutionizing Study 81
5.3 Precipitation Behavior 81
5.3.1 Response of 718Plus® to Aging Treatment in the Absence of Deformation 81
5.3.2 Stress Relaxation Tests 83
5.4 Hot Flow Curves 85
5.4.1 Material Constants 87
5.4.2 Modeling of Hardening Behavior 94
5.4.3 Modeling of DRX 96
5.4.4 Summary of Initial Analysis of Hot Flow Curves 97

6 Effect of γ' on Hot Flow Behavior of Allvac 718Plus® 99
6.1 TEM Observations 100
6.1.1 Overview 100
6.1.2 Deformation 103
6.1.3 Morphology of γ', its Relationship with γ Matrix and Symmetry Analysis 109
6.2 Set 2 Results: Tests with Holding Prior to the Deformation 112
6.3 Including the Effect of γ' upon Modeling the DRV Behavior 114

7 Summary and Conclusions 119
7.1 Summary 119
7.2 Future Work 123

List of Publications 125

Abbreviations

APB	Anti Phase Boundary
APT	Atom Probe Tomography
BCC	Body Centered Cubic
BF	Bright Field
DF	Dark Field
DRV	Dynamic Recovery
DRX	Dynamic Recrystallization
EDX	Energy Dispersive X-ray Spectrometry
EELS	Electron Energy Loss Spectroscopy
FCC	Face Centered Cubic
GB	Grain Boundary
GTE	Gas Turbine Engine
HAADF	High Angle Annular Dark Field
HAGB	High Angle Grain Boundary
HCP	Hexagonal Close Packed
HRTEM	High Resolution Transmission Electron Microscopy
LAGB	Low Angle Grain Boundary
PTT	Precipitation Temperature Transformation
RV	Recovery
RX	Recrystallization
SANS	Small Angle Neutron Scatter
SFE	Stacking Fault
SIBM	Strain Induced Boundary Migration
SR	Stress Relaxation
STEM	Scanning Transmission Electron Microscopy
TCP	Topologically Close Packed
TEM	Transmission Electron Microscopy
TTT	Time Temperature Transformation
XRD	X-Ray Diffraction

Variables

α_γ	Lattice Parameter of γ Phase
$\alpha_{\gamma'}$	Lattice Parameter of γ' Phase
σ	True Stress
ε	True Strain
σ_{sat}	Saturation Stress
σ_{wh}	Hardening Curve of Initial Material
σ_{RX}	Hardening Curve of RXed Material
σ_c	Critical Stress

σ_{ss}	Steady State Stress
σ_{sat}	Saturation Stress
σ_0	Yield Stress
Z	Zener-Hollomon Parameter
Ω	Softening Parameter of Initial Material
Ω'	Softening Parameter of RXed Material
U	Hardening Parameter
X_{RX}	Recrystallized fraction

List of Figures

1.1 Cu_3Au Crystal Structure. 6

1.2 TEM of a sample solution treated at $1050^o\,C$ for 1 hour and aged at $850^o\,C$ for 30 minutes. (a) Dark and (b) bright field TEM images, (c) observed diffraction pattern, (d) simulated diffraction pattern. 11

2.1 A representavive stess-strain Curve. 14

2.2 Schematic representation of the microstructural events during dynamic recovery. 17

2.3 Schematic representation of the typical DDRX-Type flow curves (a, b), Necklace grain structure encountered during DDRX (c), Evolution of recrystallized fraction (d) and grain size (e,f). The effects of thermomechanical processing parameters and initial grain size are also shown. 21

2.4 A TEM image of 20% Cr-25% Ni austenitic steel given a strain of 0.23 at $1102^o\,C$ at 0.01s^{-1}. 24

2.5 Heterogeneous "Nucleation" on a HAGB. The difference between the dislocation density is responsible for the driving force. Bulging boundary at the AB interface contributes the reduction of free energy by reducing the total amount of defects towards an equilibrium value. 25

2.6 Schematic representation of a superlattice dislocation pair cutting a Ni_3Al particle in Ni matrix. 31

2.7 Schematic of different strengthening mechanisms, i.e., looping around particles, precipitate cutting and solid solution strengthening (SSS) in development of overall hardening response. 33

3.1 Schematic representation of a compression test sample after small and large deformation. Shaded regions are no-deformation zones. 37
3.2 Temperature variation as a function of strain during uniaxial compression tests conducted at $1000^o C$. 38
3.3 Processing route for Set 1 tests. 39
3.4 Processing route for Set 2 tests. 40
3.5 Processing route for stress relaxation tests. 42
3.6 Baehr 805-A/D dilatometer. View of the setup (left), view of the sample chamber (right). 43
3.7 Control unit of Instron 4507 thermomechanical simulator (upper left), user interface of the control software (upper right) and main frame (down). 44
3.8 Functional block diagram of Instron 4507 thermomechanical simulator. 45
3.9 Received billet of 718Plus (left), an undeformed sample of $7.5\,mm$ diameter (middle) and a deformed sample from 805 A/D machine (right). 47
3.10 Akashi model MVK-HO microhardness testing equipment and integrated computer. 48
3.11 Olympus GX51 used for optical microscopy. 49
3.12 Jeol ARM200F Transmission Electron Microscope. . . . 50
3.13 Schematic of imaging and diffraction in TEM. 52
3.14 Ion milling equipment used for the preparation of some TEM samples. 55
3.15 Electropolishing equipment, Struers Tenupol (left) and its sample holder (right). 56

4.1 Schematic diagram of an experimental flow curve σ_{exp} and the derived work hardening σ_{wh} and work hardening of recrystallized material (σ_{rex}). 69

5.1 (a) & (b) Optical micrographs at 10 and 20x magnification respectively; (c) & (d) Scanning electron micrographs at 150 and 300x magnification respectively. . . . 80

5.2 PTT diagram of 718Plus^{TM}. Red line denotes 245HV limit. Time axis is given in Hours for ease of comparison with the work of Srinivasan and Xie. 83

5.3 Stress relaxation curves recorded after subjecting the samples to a 10% deformation 1s^{-1}. 84

5.4 TEM Dark field (a) and bright field (b) images of the stress relaxation sample of $920^o\,C$ quenched just after the determined precipitation start point. The spots where precipitation can be observed are designated with white dashed circles and superlattice reflection is shown by the white arrow. 85

5.5 STEM Bright field (a) and high angle annular dark field (b) images of the stress relaxation sample of $920^o\,C$ quenched just after the determined precipitation start point. The diffraction pattern shows the composite lattices clearly with weak superlattice reflections and precipitates can be observed in dark field image as bright spots. 86

5.6 Flow curves of Set 1: Hot flow study without prior aging to determine baseline response of the alloy. 87

5.7 Plots that are used to retrieve material constants of apparent approach: (a) n', (b) β, (c) n, (d) A. 88

5.8 Experimentally determined TTT diagrams of 718Plus, (a) from Xie *et al.* and (b) from Stotter *et al.* While (a) is showing both γ' and δ, (b) is showing only δ precipitation 90

5.9 Plots used to retrieve activation energy based on power law (a), exponential law (b) and hyperbolic sine law (c) 91

5.10 Plot used to derive the material constants for physically based approach: α' and B. 92

5.11 A validation plot showing predicted peak stresses by both apparent and physically based approaches versus experimental results. 93

5.12 Dependence of softening and hardening parameters on the Zener-Hollomon parameter. 95

5.13 Material constants Ω, Ω' and U based on the approach of Quelennec and Jonas (see Section 4.1.4) 95

5.14 Curves used to determine the DRX kinetics: From top to bottom: $950°$C, $1000°$C and $1050°$C. 96

5.15 Dependence of k of Avrami model on the Zener-Hollomon parameter. 97

6.1 TEM images after solutionizing at $1050^o\,C$ followed by 30 minutes aging at $850^o\,C$: (a) Low magnification image giving an overview of the microstructure, (b1) Bright field and (b2) corresponding dark field images recorded along [011]γ // [011]γ' zone axis. STEM images, (c1) High Angle Annular Dark Field image and (c2) its bright field image. 101

6.2 TEM bright field (a1 & b1) and corresponding dark field (a2 & b2) images of (a) aged ($850^o\,C$ for 20 mintues) and (b) deformed ($920^o\,C$, $0.01\,s^{-1}$) sample. Both dark field images were recorded using (001) weak superlattice reflection. 102

6.3 EDX maps of aged and deformed samples: (a) $920^o\,C$-$20'$, (b) $940^o\,C$-$30'$ 104

6.4 (a) Bright field TEM image with approximate zone axis [011]. (b2) A close up view of a portion of the image shown on (a). (b1) is the recorded diffraction pattern of the image (b2). 107

6.5 Bright field (a1 & b1) and weak beam dark field (a2 & b2) TEM images of $920^o\,C$-20′ sample after deformation. Weak beam image (g-3g) g=001 recorded along zone axis close to [011]. 108
6.6 Bright field TEM image of $940^o\,C$-0′ sample. (a/2)$<110>$ type of matrix dislocations. 109
6.7 High Resolution TEM (HRTEM) image and its corresponding FFT recorded along $[011]_\gamma$ // $[011]_{\gamma'}$ zone axis. 110
6.8 Hot flow response of different samples aged at $850^o\,C$ for different times. Left: $920^o\,C$, $0.01\,s^{-1}$; Right: $940^o\,C$, $0.01\,s^{-1}$. 112
6.9 Strain to critical stress, critical stress and yield strength; plotted as a function of aging time. 113
6.10 Measured and calculated flow curves based on model given in Section 4.1.5. Solutionized and aged specimens for 30 and 120 mins. are given. 117
6.11 Increase in σ_p at 920 and $940^o\,C$ as a function of aging time. Breakdown of the calculated increase in σ_p (based on Eq. (4.33)) due to different contributing mechanisms (i.e. σ_{cut} and σ_{loop}) are given (continuous and dashed lines). Finally, activity of the cutting mechanism (f_{cut}) is presented as a function of aging time. 118

7.1 Higher level flow of the overall integration of the precipitation model. 122

List of Tables

1.1 Chemical compositions in wt. percent of IN718, 718Plus^{TM} and Waspaloy. 8

5.1 Resulting hardness values in Vickers (1 kg) for various solutionizing treatments. 81
5.2 Hardness results of aged 718Plus^{TM}: Comparison of different studies. 82

6.1 Determination of H, the intersection point group, the elements of which are common to the point groups of γ and γ' phases. n is the number of variants; m, p and h are the orders of the point groups of matrix, precipitate and intersection group respectively. 111
6.2 Calibration of γ' volume fraction and radius evolution of 718Plus with deformation time t 115
6.3 Model parameters and results. 116

Chapter 1

Introduction

The term "superalloy" may be defined as an alloy of VIII elements (nickel, cobalt or iron with high percentage of nickel) with other additions in minor contents. The main characteristic of this alloy group is the relatively high strength at high temperatures together with chemical stability [1].

Be it nuclear reactors, industrial furnaces, biomedical devices or automotive turbochargers, today there are various fields that use the advantage of specific properties of superalloys. However, the main use of these alloys is the hot sections of the Gas Turbine Engines (GTEs) since their introduction, rooting to 1920s [2].

The microstructural evolution of superalloys during the service life or forming processes involves accumulation, annihilation and rearrangement of dislocations, recrystallization and grain growth. Alloying elements, such as W, Ta, Ti, Mo, Nb, Cr, Si, Al can form carbides and/or ordered precipitates (Al, Ti, Nb) affecting the course of the microstructural evolution. For hot deformation, the microstructural evolution that occurs in the material is dependent on the amount of the dimensional reductions, the strain rate, the temperature and the length of the holding times between reductions. For ring rolling, a process used to obtain seamless drum-like forms of superalloys, it is the desired final mechanical and geometrical properties of the work piece that determines the so called operation schedule, which is the setup for the deformation process, i.e.

the amount of reduction, the deformation velocity, number of passes and the temperature.

1.1 Brief History of Superalloys

In the 1920s and 1930s, market demands for higher strength Ni - base alloys drove researchers to develop precipitation hardening nickel alloys. [3] At the time, the metallurgy of nickel alloys was relatively unknown except that the basic structure was austenitic, and therefore the matrix arranged itself in the Face Centered Cubic (FCC) structure. The demands of early marine, naval, and oil and gas applications for higher strength combined with corrosion resistance prompted the research that resulted in the addition of aluminum and titanium to existing Ni-Cu alloys. This would initiate the formation of a second phase when properly heat treated. The second phase is now known as gamma prime γ' [4]. This alloy was later put in the market with K - MONEL name and later MONEL alloy K - 500. This alloy, when compared to the existing Ni-Cu alloys, doubled its yield strength due to γ' precipitation. [5]

The ability to significantly increase the strength of Ni base alloys by precipitation hardening became one of the most revolutionary technical discoveries of the nickel alloy industry in the twentieth century. Due to the remarkable increase in strength/weight ratio made possible by the precipitation hardening alloys, the aerospace industry was stepping into the jet propulsion since the weight of turbine engines could be reduced significantly. The later development of the alloy Inconel 718 further advanced the development of gas turbine jet propelled aircraft. In some engines today, the alloy 718, accounts for over 50% of the superalloy content [6].

1.2 Motivation and Focus of the Current Work

Accurate simulation of the behavior of materials and systems is perhaps one of the most important emerging needs in engineering world of 2000s.

In order for the engineering simulations to be reliable and practical, correct mathematical models and efficient numerical schemes should be implemented.

From the materials science point of view, there are different strategies to model the material behavior. It is hard to claim an advantage of one over the other. For example, phenomenological constitutive models can be expressed as a function of the forming parameters (temperature, strain rate etc.) to consider the effects of these forming parameters on the flow behavior of metals or alloys. A phenomenological model is actually the classical approach for modeling the material behavior. Macroscopic mechanical test results are fit to a convenient mathematical function. On the other hand, physically based models try to establish constitutive models which consider the observable mechanism of deformation, such as dislocation dynamics, thermal activation etc.

The challenge here is to establish a model, complex enough to represent the material behavior and simple enough to avoid fluctuations due to uncertainties. Furthermore, the model should be efficient enough from the computational resources point of view.

It would not be wrong to say that the service performance and formability of alloys are determined by the interaction between the micro- and dislocation structure. For superalloys and other precipitation hardening alloys, the existence of second phase particles make the scene slightly more complex as precipitates interact with many physical processes taking place during deformation.

The aim of the current work is to have an understanding of the response of superalloys to the high temperature forming operations and to explain them with appropriate mathematical models for future use. To this end, compression tests are employed at various temperatures and strain rates. Samples with different thermal treatment histories are used

to understand the effects of initial microstructure, mostly focusing on the amount of second phases particles, instead of grain size.

The material used during this work was ATI ALLVAC 718Plus®. Hot compression and stress relaxation tests are employed for thermo-mechanical treatment of the material. For characterization, optical and scanning/transmission electron microscopy and X-Ray diffractometry are used.

1.3 Overview of Superalloys Strengthened by Ordered γ' Particles and Carbides

1.3.1 Introduction

The precipitation strengthened Ni base alloys generally contain additions of titanium, aluminum and/or niobium that form a strengthening precipitate with nickel after an appropriate heat treatment.

The major phases in most of the superalloys are gamma prime γ' $Ni_3(Al, Ti)$, gamma double prime γ'' Ni_3Nb and equilibrium δ. While γ' and γ'' are metastable phases, δ, is a thermodynamically stable phase corresponding to γ''. Among these, γ' and γ'' are generally accepted as main strengthening phases in superalloys [7].

The extent of strengthening which will be achieved through precipitates is determined by elastic coherency strains in the vicinity of the precipitate, the Anti Phase Boundary (APB) energy, interfacial energy between the matrix and the precipitate, elastic modulus difference and Stacking Fault Energy (SFE). The dominating strengthening mechanism might change with temperature. Of course, in addition to these, the precipitate morphology, size and distribution are very important parameters in precipitation hardening.

The thermal stability and strength of the system depends on the coarsening rate of the strengthening particles at high temperatures. [1,8]. The lattice misfit is responsible to alter the contribution which comes from different mechanisms. Usually, a lower misfit is preferred and

the commonly adopted strategy to achieve this is to use solid solution strengtheners.

In addition to the chemical manipulations, heat treatment is another tool to adjust the properties of precipitates. Usually, superalloys in the industry are used after solutionizing and aging treatments.

1.3.2 Carbides

In superalloys, the rate of grain boundary sliding and migration are usually desired to be low in order to have better creep properties. To this end, a number of alloying elements are used to procure carbide precipitation within the matrix as well as at grain boundaries [1, 7, 8]. However, an optimization problem arises with carbide precipitation when the grain boundary embrittlement is considered. As a rule of thumb, the carbides are desired to co-exist with the ordered main strengthening precipitates so that the low lattice misfit ductility prevents the grain boundary failure.

MC type of carbides are usually said to be stable up to temperatures close to solidus temperature of the alloys. They can be formed by Ti, Ta, Nb, W, Mo, Cr. On the other hand, $M_{23}C_6$ type of carbides are formed below 1250 K with Fe, Mo, Ni, Co, Ti, W, Nb. The latter is the most important carbide type from an industrial perspective. As found by Taylor [9], this type of carbide precipitates at Grain Boundaries (GBs) and may lower the Cr content around it, which may influence the precipitation behavior of γ'.

There are other types of carbides and precipitates (Topologically Close Packed (TCP) phases; laves, sigma mu etc.); however, these are not explained here since they are out of scope of this text.

1.3.3 Crystallography

In γ' strengthened Ni base superalloys, both γ and γ' phases have Face Centered Cubic (FCC) crystal structure. The γ' phase is long range ordered and employs the Cu3Au structure, $L1_2$, shown in Fig. 1.1. This crystal structure consists of a primitive array of gold atoms, with one

copper atom occupying each face of the unit cell. The copper atoms form an octahedron inside the unit cell.

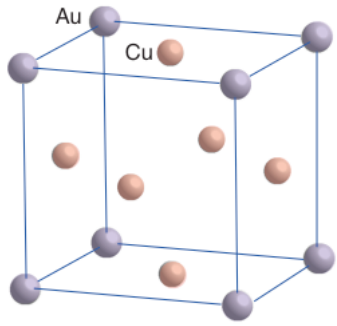

Figure 1.1: Cu_3Al crystal structure. [10]

In the stoichiometric binary Ni_3Al phase, Ni and Al atoms stand on the Cu and Au sites respectively. However, in multi component γ' phases, the exact site preference of the atoms needs to be determined through experimental methods.

The nucleation of γ' phase usually occurs as homogeneous nucleation. The reason behind this is the low interfacial energy between the γ' particles and γ matrix. Zickler et al. [11] have reported this value for 718Plus alloy as 47mJm^{-2} through Small Angle Neutron Scattering (SANS) studies. In their report, they compiled other results focusing on other Ni-base superalloys, whose interfacial energy was ranging from 1 to 140mJm^{-2}. One should be aware of the effects of determination method for this value as each experimental technique has its advantages and drawbacks.

1.3.4 Lattice Mismatch

Unconstrained lattice parameters of individual γ and γ' phases can be measured through direct and indirect methods. Then the lattice misfit (δ) can be calculated according to the following relationship:

$$\delta = (a_\gamma - a_{\gamma'}) / a_\gamma \tag{1.1}$$

where a_γ and $a_{\gamma'}$ are the lattice parameters for matrix and precipitates respectively, when very finely γ' precipitates are "forced" to adjust their lattice parameters to that of the matrix. When the misfit is calculated under these circumstances it is called "constrained lattice misfit".

There are models which relate the precipitation hardening to the degree of lattice misfit [12, 13], this will be briefly mentioned in the section 2.4.4. Lattice constants and lattice mismatch of various alloys and metals can be found in a text printed by Nembach [14].

Another important effect of lattice misfit is on the morphology of the precipitating phases. Previous reports on Ni base superalloys [15–17] show that during the early stages of precipitate growth, morphology is a clear function of both misfit and particle size, since the transition from spheres to cubes will depend on the total matrix precipitate strain present due to the lattice.

1.4 Alloy ATI 718Plus®

1.4.1 Introduction

Inconel 718, the ancestor of ATI 718Plus is the most used Ni base superalloy in gas turbine industry, having a mass ratio between 55% and 70% [18]. However, this alloy has the maximum service temperature capability around $650^o C$. Within the years, as the turbine inlet temperatures rose, seeking higher efficiencies in gas turbines, this maximum temperature limitation of Inconel 718 became a bottle neck for cold section material selection.

Together with this, the alternative alloys had/have costly materials, which makes them financially unfavorable [19]. While there are other alloys such as Rene 41 and Waspaloy, which are used at sections where temperatures achieve more than $650^o C$; these alloys come with challenging forging and welding processes.

The alloy 718Plus has its place for the sections where up to $50^o\,C$ maximum service temperature increase would be necessary, without amplifying the budget or sacrificing malleability and weldability with respect to its ancestor, Inconel.

Table 1.1: Chemical compositions in wt. percent of IN718, 718Plus^{TM} and Waspaloy.

Alloy	Ni	Cr	Mo	W	Co	Fe	Nb	Ti	Al
718	Bal	18.1	2.9	-	-	18	5.4	1	0.45
718Plus^{TM}	Bal	18	2.8	1	9	10	5.4	0.7	1.45
Waspaloy	Bal	19.4	4.25	-	13.25	-	-	3	1.3

1.4.2 Development & Chemistry

The theoretical studies to develop the alloy 718Plus started in the early 90s with the aim of improving the creep and rupture properties of alloy 718 by additions of P and B [20–23]. With these already a $20^o\,C$ temperature capability increase was achieved. Afterwards, an extensive research effort has gone to extend the temperature capability up to $55^o\,C$. To this end, both experimental and computational work has been conducted, starting from the base alloy and looking to the effects of additions of different elements on thermal stability, mechanical properties and structure. An extensive progress history regarding the development stages is reported by Kennedy [19].

One of the first findings from the theoretical studies was the importance of the ratio of Al/Ti. Cao observed that the 4:1 ratio of Al/Ti maximizes the high temperature stability and rupture life. This ratio was 1 in the base alloy. During these studies, there was no sign of embrittlement and the rupture ductility did not show a degradation (if not an increase). In these studies [19, 23] the effect of the Co amount is also highlighted. Thermal stability and rupture life showed peak values around 10% Co.

Finally, the optimum chemical composition for rupture life, thermal stability and strength was achieved with 9% Co, 10% Fe, 1% W. The amount of Nb and Mo remained constant with respect to the alloy 718. As alloys 718 and Waspaloy are well known, the chemical composition of alloy 718Plus is given together with that of these alloys (see Table 1.1). As it can be seen, Cr and Mo amounts are the same for 718 and 718Plus; and comparable to Waspaloy. The increasing content of Co from 718 to 718Plus and Waspaloy is clearly observed as well. The main difference between 718 family and Waspaloy is the absence of Fe and Nb in the latter.

1.4.3 Phases

As mentioned previously, 718Plus contains more Co and less Fe, and the Ti/Al ratio is much lower when compared with 718. This chemical composition, combined with the appropriate heat treatment is observed to provoke the precipitation of γ' (Ni_3[Al Nb Ti]), L12, cubic) and δ while impeding that of γ'' (Ni_3Nb, D022, tetragonal).

The precipitation kinetics of the strengthening & GB precipitates is of interest and there have been a number of studies focusing on this [19, 24–26].

Solution treatment at $1050^o\,C$ for 1 hour followed by double aging at $720^o\,C$ for 8 hours and $650^o\,C$ for another 8 hours is observed to create two different sets of γ' [27]. These sets of particles have a characteristic diameter of 20-30 nm (higher number density), and 100 nm (lower number density) respectively based on the aging treatment.

Another study [25] reports the existence of γ' particles with 25 nm diameter after a solution treatment at 954^oC for 1 h, then 788^oC for 2 h and finally $649^o\,C$ for 8 h. Similar size and single set of particles are reported after similar heat treatments [11]. Cao reported that the volume fraction of the primary hardening phase γ' varies from 19.7% to 23.2% depending on the amount of grain boundary precipitates [24]. The importance of the δ phase in terms of grain size control and stress rupture properties is well known in alloy 718.

Since the appearance and precipitation behavior of the grain boundary precipitates in 718Plus^{TM} were found to be similar to that of δ phase of 718, they were initially identified as δ phase (Ni_3 Nb, D0a, orthorhombic) as well [24, 28, 29]. However, it was later studied in depth by Pickering et al. [30] and reported that the grain boundary (GB) precipitates mainly consist of layers of η phase (Ni_6 Nb [Al Ti], D024, hexagonal) accompanied with δ layers. Considering the similarity of the mechanical effects of GB precipitations between the 718 and 718Plus^{TM}, in this work, the term δ will be used for GB precipitates.

Figure 1.2, from the current study, shows a dark field and corresponding bright field TEM image together with observed and simulated diffraction patterns of a sample solution treated at $1050^o C$ for 1 hour and aged at $850^o C$ for 30 minutes. Images are recorded on $[011]_\gamma$ // $[011]_{\gamma'}$ zone axis and they indicate the weak reflections originate from the very fine precipitates of γ' phase.

Based on TEM observations, Whitmore et al. [31] measured the lattice mismatch of 718Plus to be $\delta = 0.003 \pm 0.002$, $\delta = 0.003 \pm 0.0015$ for single and double aged condition respectively.

It is important to highlight that some of the aging times employed in this study are shorter when compared to these aging times (from 15 to 30 minutes vs 4 to 8 hours), thus assuming these lattice misfit parameters may create uncertainties.

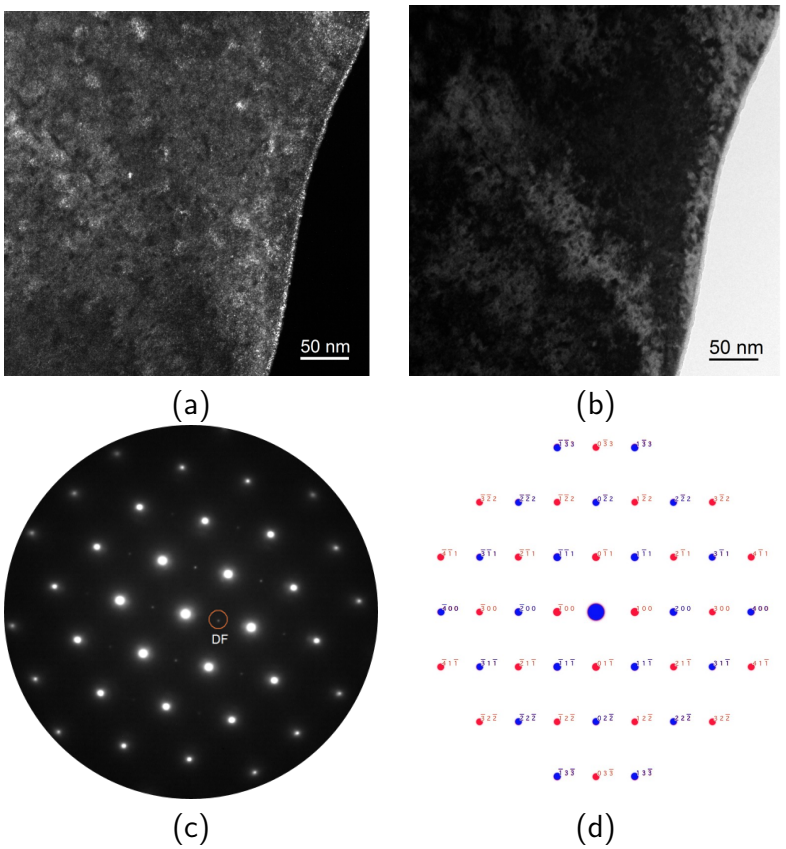

Figure 1.2: TTEM of a sample solution treated at $1050^o\,C$ for 1 hour and aged at $850^o\,C$ for 30 minutes. (a) Dark and (b) bright field TEM images, (c) observed diffraction pattern, (d) simulated diffraction pattern.

Chapter 2

Physical Processes Occurring During Hot Forming

In order to optimize the service live and/or performance of components, apart from an optimum mechanical design, one has to have a strict control of the metallurgical state of the finished component. Undoubtedly, the most important metallurgical aspect to dominate is the microstructure of the material. While there are various different types of metal forming methods, operations at elevated temperatures are favored because of the capability to achieve extended plasticity. However, due to high strains and high temperatures, heavy microstructural modifications are observed as well. Moreover, when dealing with large work pieces, the forming routines consist of many passes due to heat losses during the forming process, leading to loss of plasticity and increase of die forces. Thus, the relationship between the processing parameters and microstructural state of the material must be well known. Furthermore, in alloys strengthened by second phase particles, the hardening and softening processes and their interaction with precipitation is of interest and more complex since the precipitation introduces an additional physical phenomenon to include in the model.

2.1 Compression Tests and Flow Curve

Compression tests are widely implemented to investigate the high temperature deformation behavior of metallic alloys. Since the hot deformation behavior is to be investigated, tests are usually conducted at different temperatures and deformation rates of interest.

The results are usually converted to true stress-strain diagrams to have a comparative picture. In Fig. 2.1, a schematic of stress strain curves for different metallurgical scenarios are superimposed. Most of the time, compression test results are supported with microstructural investigations; however, it is possible to retrieve some important facts solely based on the curves, to explain the hot behavior of the material.

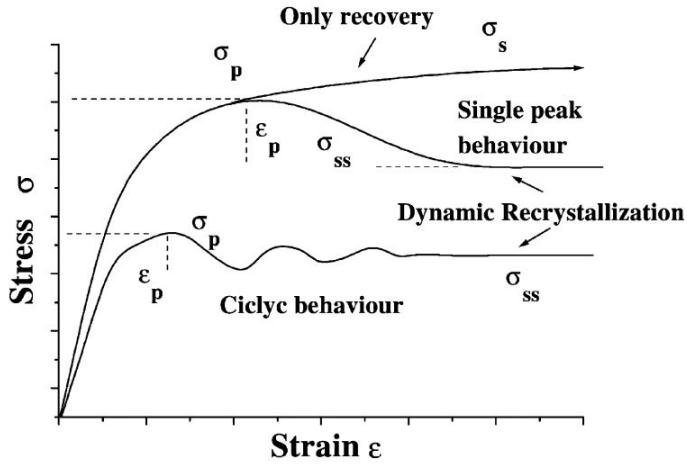

Figure 2.1: A representavive stress-strain Curve. [32]

The flow curve(s) shown in Fig. 2.1, are usually divided into three stages: hardening and dynamic recovery (1), transition stage (2) where a drop in the flow stress is observed due to dynamic recrystallization, and finally saturation or steady-state (3) in which the rate of generation and annihilation of dislocations are equal.

The drop in the transition period can be a continuous drop (referred

as "single peak" behaviour), or a discontinuous (referred as "cyclic" behaviour). In some materials, the drop in the flow stress is not observed. In this case, the material is said to undergo only dynamic recovery. Similarly, the reason of this behavior can be related to deformation conditions or material properties. An important material property driving one or the other as the main softening mechanism is the Stacking Fault Energy (SFE). For example, in aluminum as the SFE is very high the dissociation of a perfect dislocation to partials is not energetically favorable. This is why a perfect dislocation can easily cross-slip (if screw dislocation) or climb (if edge dislocation), favoring the occurence of dynamic recovery. In Ni alloys and γ-Iron, on the other hand, the SFE is considerably lower than that of Al and can be said to have "moderate" SFE which paves the way for dislocation dissociation. For this reason, recrystallization plays a bigger role in the softening of these materials during hot deformation.

When these softening processes occur during hot forming/deformation processes, the term "dynamic" is added to create a distinction from the static softening processes.

2.2 Work Hardening and Dynamic Recovery

The common point in the behavior of the materials with high and low stacking fault energy is the work hardening. It is prevalent that the metals experience work hardening throughout the deformation; however in the initial stages of the stress-strain curve, as the softening mechanisms are not fully activated, it is possible to see the stress increment due to work hardening.

As the metal is deformed, the number of defects i.e. dislocations increase. Through this increase, the material becomes thermodynamically more unstable. At relatively high temperatures the system tends to reduce the free energy through thermally activated processes. When this reduction of free energy occurs after deformation, it is called Static Recovery (SRV), while if it occurs during the course of deformation, then

it is referred to as dynamic recovery (DRV) [33].

As a result of plastic deformation, the number of dislocations per unit volume multiplies. The dislocation multiplication mechanisms will not be discussed here.

However, once there is a driving force for recovery, primary processes are dislocation glide, climb and cross-slip to decrease the stored energy. While the opposite sign dislocations on the same glide plane can annihilate each other at lower temperatures by gliding, if they stand on different glide planes; they must use glide and climb. Since climb necessitates a thermal activation, higher temperatures are required for this to take place. As a result, it can be said that preferred mechanism for the movement depends on geometrical and thermal factors.

The geometrical factors include the number of active slip systems, which in turn depends on the type of crystallographic structure. As mentioned above, climb is a thermally activated process. When the deformation takes place at higher temperatures this becomes the dominating mechanism and, in turn, the deformation is said to be controlled by diffusion. [34, 35]

The stress-strain curve of the materials undergoing only dynamic recovery has a shape similar to what is marked as "Only Recovery" in Fig. 2.1, where a continuous increase is observed. Eventually when the rate of work hardening and dynamic recovery are equal, it is possible to observe a plateau in the stress-strain curve [36, 37].

In general, it can be said that recovery leads to a partial restoration of the dislocation structure and material properties towards the undeformed state of the material [38]. The microstructure can go back to the initial state to some extent through dislocation rearrangement and annihilation.

Through recovery, more homogeneous microstructure evolution is observed when compared to other softening mechanisms. Recovery usually does not involve the high angle grain boundaries' migration [39].

Recovery generally consists of a series of microstructural changes in the material. Humpreys and Hatherly [34] schematically presented these events, as shown in Fig. 2.2. These include the dislocation generation (a), formation of the cell-like structures (b), dislocation annihilation in

the cells (c), subgrain formation (d) and subgrain growth (e).

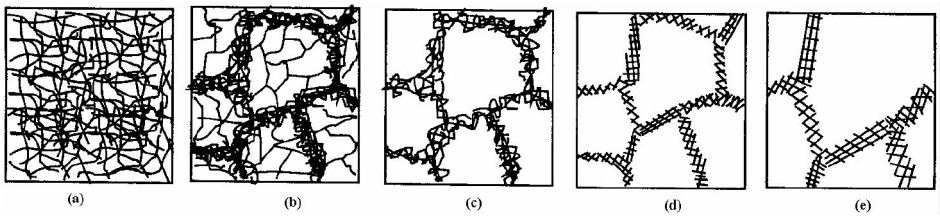

Figure 2.2: Schematic representation of the microstructural events during dynamic recovery. [34]

In the interpretation of the Fig. 2.2, it is important to keep in mind that although the sequence of the events are given in a chronological order, there may be overlaps between them.

As the driving force for DRV is the stored plastic energy (dislocation density) in the material, once recrystallization has started and dislocation substructure has been consumed, there will not be any possibility for recovery to occur.

Likewise, the extent of DRV is important as well for Dynamic Recrystallization (DRX) to take place. If substantial amount of energy is recovered during DRV, DRX will be delayed due to lack of driving force. For this reason, the distinction of these processes is difficult and the onset of DRX is thought to overlap with the final stages of DRV [34].

2.3 Dynamic Recrystallization

Doerth et al. [39] defined recrystallization phenomenon as the process of achieving a new grain structure by the formation and migration of High Angle Grain Boundaries (HAGBs). The driving force of this process is the stored energy introduced by plastic deformation. This is now a generally accepted definition. When recrystallization occurs during the course of high temperature deformation i.e. above the 0.5 x homologous

temperature[1] then it is called as "dynamic recrystallization".

For low to medium SFE metals, the formation of partial dislocations is energetically more favorable. This limits the existence, and in turn migration, of perfect dislocations. In this type of materials, recrystallization is a very strong mechanism for softening. In general, we can name two different dynamic recrystallization types: discontinuous and continuous. In addition to this, there is a type of recrystallization observed in Al alloys, called geometric recrystallization; however, this lays out of scope of this text.

In discontinuous dynamic recrystallization (DDRX), new strain free grains form at suitable places in the microstrucutre and grow while "eating up" the grains where dislocation density is high. When instead, low angle grain boundaries formed through dynamic recovery, evolve and transform into high angle grain boundaries, thus making the cell structures evolve into new grains, it is called "continuous dynamic recrystallization CDRX" [34]. In general recrystallization terminology, when DRX used in a context without any specification, usually DDRX is understood. Here it is important to mention that SFE is not the only parameter determining which mechanism (DDRX or CDRX) is to dominate the softening process.

When dynamic recrystallization occurs, it causes changes both in the microstructure and the stress-strain response of the material. In case of DDRX, it consists of nucleation and growth of new "dislocation free" grains, as mentioned above, [2] which lowers the overall dislocation density of the material. This, in turn, is observed as a drop in the stress levels in the hot deformation response of the material.

When new strain-free grains at the deformed grain boundaries nucleate, the difference in the dislocation density between these grains and adjacent ones create a positive driving force for the boundary migration.

[1] Homologous temperature expresses the temperature of a material as a fraction of its melting point temperature using the Kelvin scale.

[2] The nucleation growth of DRX is a partially accepted theory and believed to be different than classical nucleation growth behavior observed in diffusional phase transformations.

Because of this driving force, DRX is thought to be a more efficient softening mechanism. However, as one can guess, this necessitates attaining a certain level of dislocation density in the material. The strain at which this dislocation density is attained is termed as critical strain, ε_c.

The recrystallization has a big role in determining the final microstructure of engineering alloys. Humpreys el al. states that the research in this field dates back to 150 years ago [34]. In more recent years, from 1960s on, the DRX theory has evolved substantially. A great review paper by McQueen summarizes the developments until 2004 [40].

DRX is influenced by many different factors, including SFE, processing parameters, initial material properties or chemistry. From 2004 on, as Elecron Back Scattered Diffraction (EBSD) technology becomes popular, researchers could achieve very broad information regarding how DRX evolves and how it is affected by these factors. An extensive review paper by Sakai et al. [41] focuses on the recent findings. As DRX is not the only focus of this text, these factors are only briefly covered.

There are a few observations regarding the materials that soften through DDRX. To start with, for DDRX to occur, the material has to be deformed beyond a critical strain [42, 43]. This strain is observed to vary, and there are some authors reporting that it lays around 70-80% of the peak strain. As the peak strain, with decreasing Zener-Hollomon[3] parameter the critical strain for DRX also decreases [44].

The thermomechanical processing parameters (temperature, strain rate) and initial material (grain size) eventually determine if the material will undergo a single or multi-peak DRX softening. As mentioned various times in this text, in the later stages of the deformation, there is a direct correlation between the steady state stress and the Zener-Hollomon parameter which takes into account the combined effect of strain rate and temperature. The initial grain size is said to have no effect on the steady state stress [45]. The overall effect of deformation

[3]The Zener–Hollomon parameter is also known as the temperature compensated strain rate. It is given by $Z = \dot{\varepsilon}\ exp(Q/RT)$ where $\dot{\varepsilon}$ is the strain rate, Q is the activation energy, R is the gas constant, T is the temperature.

It is named after Clarence Zener and John Herbert Hollomon, Jr.

temperature and strain rate on the grain structure, recrystalliztion and grain size is summarized in Fig. 2.3. Usually the grain boundaries of the initial material are used as nucleation sites. In case of newly formed, strain-free grains being much smaller than the original grains, the well known "necklace structure" is formed [46].

Perhaps it would not be wrong to state that when a low/medium SFE material is given more space and time to deal with the stored energy, the kinetics of the DRX is higher. This can be achieved through lower strain rates and/or lower initial grain sizes [44, 48].

Similar to the flow curve behavior, the grain size of the material smoothly approaches to a constant value as the softening process progresses. This constant value is referred to as "saturation grain size" (D_{sat}). Thermomechanical processing parameters and initial grain size will determine whether the final grain size will be coarser or finer than the initial one. Usually the Zener-Hollomon parameter is related to the D_{sat} through a power-law like relationship [45, 49–51].

In this work, while the author does not intend to give an exhaustive review of DRX. In various sections of this text, factors influencing DRX and related kinetics are reported as well, because correct understanding and modeling of DRX is one of the key steps to predict material behavior during hot forming.

A good, applicable mathematical model representing DDRX should foresee the evolution of the grain size(s), recrystallized fraction, texture and stress levels in the flow curve. Of course, this predictive capability should come with an affordable computational cost.

The existing DDRX models can be said to have enough predictive capabilities for abovementioned quantities, except the texture. It is obvious that the ability to predict and control the texture of the material is of interest for industrial processes. However, it is perceived that a correctly occurring recrystallization is a process which makes the microstructure more uniform and homogeneous.

In case of the existence of second phase particles, their distribution within the microstructure, size and number density, and the evolution of these quantities throughout the deformation process should be consid-

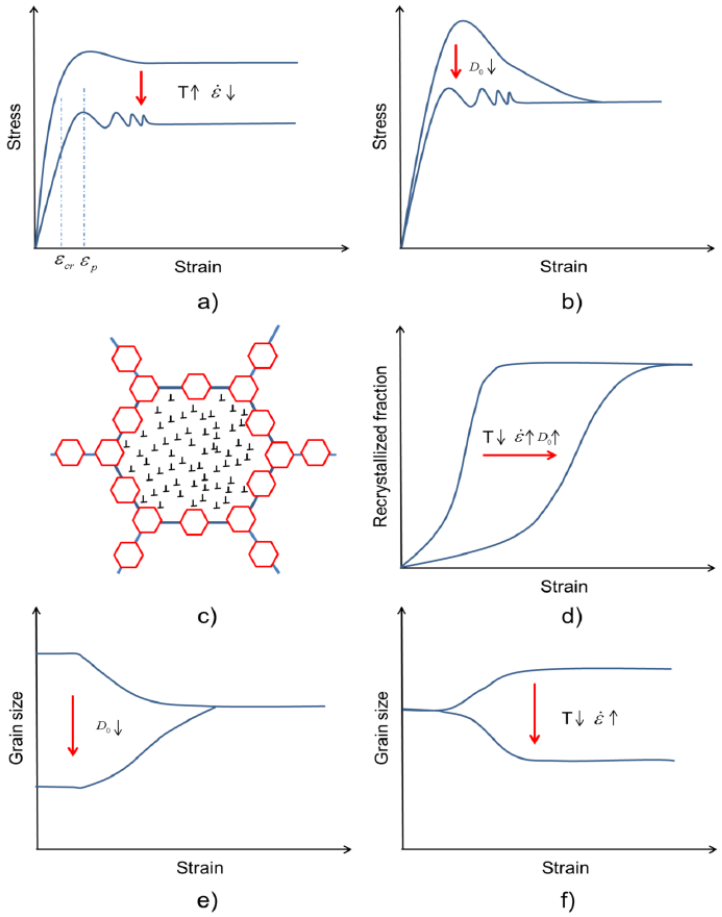

Figure 2.3: Schematic representation of the typical DDRX-Type flow curves (a, b), Necklace grain structure encountered during DDRX (c), Evolution of recrystallized fraction (d) and grain size (e,f). The effects of thermomechanical processing parameters and initial grain size are also shown. [47]

ered. While there are a few authors highlighting the particle stimulated nucleation (PSN) for DRX (such as Lee and Hua [52]) overall, there is little evidence as to the effectiveness of PSN.

It is especially important and of industrial interest to add these secondary effects into the DRX models to accurately predict the material behavior after the critical strain. This being said, it is a challenge to still keep the models simple enough for wide deformation conditions.

This work focuses on the modeling of the nickel base superalloys' response to forming processes at high temperatures. Thus, well known DRX models are adapted and used to model the flow curves after the critical strain for recrystallization.

It is important to know that, metadynamic recrystalization may take place if the sample is deformed beyond the critical strain for DRX initiation and if the quenching process is retarded. This type of softening mechanism is strain-independent and occurs by continued growth of the nuclei formed by dynamic recrystallization during straining, thus it does not require an incubation time. This is important for the current work as in some samples the highest dislocation density for the respective hot deformation is sought to observe dislocation particle interaction without any other mechanisms being involved. Thus, it is important to have sufficient quenching speed to obtain reliable "frozen microstructures" especially to observe the nucleation/evolution of DRX and dislocation structure at the onset of DRX.

2.3.1 Nucleation of DRX

If one needs to control the DRX process is it necessary to understand how it originates and through what parameters it can be better controlled. In addition to this, the size and orientation of the final grains will be determined based on the nucleation of DRX. Because of these facts, substantial amount of research effort is put into the understanding of nucleation of DRX.

For DRX, the interfacial energy between two differently oriented grains is quite large and the driving force (stored energy in the mate-

rial) is very low when compared to diffusional phase transformations. Mittemeijer [38] has conducted a basic feasibility calculation using the classical heterogeneous nucleation model, and found that the nucleation rate of DRX is extremely small. Instead, in more recent theories usually subgrains or other low dislocation density regions are thought to be the incubators of recrystallization. Apart from being energetically favorable, a large orientation difference between these and the neighboring regions is necessary to create successfully growing dislocation free grains, thus nucleating recrystallization. Humpreys [34] summarized different theories regarding the nucleation mechanisms of DRX as follows, including the failing classical nucleation theory. It is reported that Strain Induced Boundary Migration (SIBM) is thought to play the role of initiating the nucleation of DRX which was initially proposed by Becky [53] who made observations on high purity Al.

While SIBM and derivative theories are the ones which better explain the nucleation of DRX exist, this is still a point which is not fully understood.

In the case of discontinuous dynamic recrystallization, as the high angle grain boundaries proceed, the dislocation density in the newly formed grain keeps increasing. Thus, a simple calculation [54] would show the nucleation viable only once the rate of SIBM is relatively high when compared to the dislocation multiplication rate in the newly formed grain.

Huang has performed the energy analysis for a spherical nuclei once more in a review paper in 2016 [47] and according to this, when the nuclei is spherical the critical dislocation density for a spherical nuclei is given as Eq. 2.1

$$\rho_{Crit}^{DDRX} = \left(\frac{16\ \dot{\varepsilon}\ \gamma_{GB}}{3\ bLm\tau^2}\right)^{1/3} \tag{2.1}$$

where γ_{GB}, b, L, m and τ are the grain boundary surface energy, burgers vector, free path of dislocations, boundary mobility and the dislocation line energy, respectively.

The successful nucleation probability for this case is extremely low, as also reported by Christian [55]. As the "genuine" nucleation of new

strain-free grains with high-mobility, high-angle boundary is not favorable, the heterogenity of the deformed microstructure may be the explanation of the DRX initiation. Because of this, strain induced migration of a boundary which separates high & low dislocation density grains is thought to be the key point of the DRX nucleation. In a text printed in 1972, Honeycombe [56] concluded that the most attractive model for DRX nucleation is, just like the static recrystallization, the bulging of the grain boundary between two locking points. After a critical strain, this process becomes energetically more favourable than the localized sharpening of subgrain boundaries. There is indeed a visual evidence for this as shown in Fig. 2.4, where the grain boundary marked as AA, has become serrated by sub-boundary pinning, while the twin boundary, BB, has not. This is schematically shown as well in Fig. 2.5.

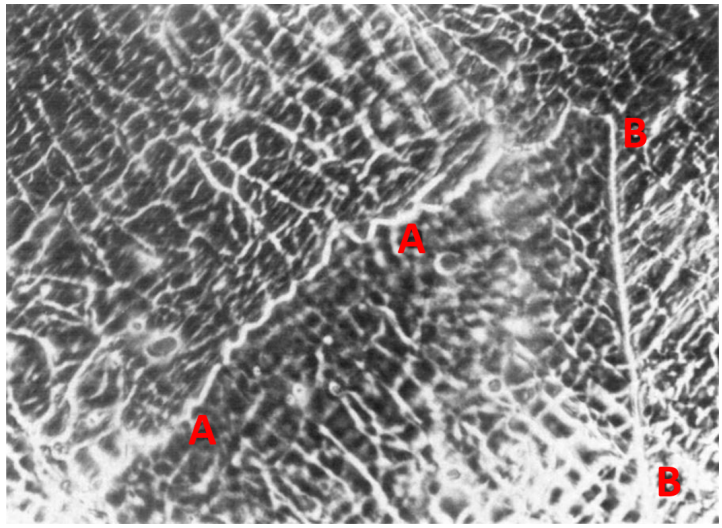

Figure 2.4: A 20% Cr-25% Ni austenitic steel given a strain of 0.23 at $1102^o\,C$ at 0.01s^{-1} showing the bulging process of the grain boundary between two locking point to start recrystallization. [56]

When the calculations made for spherical nucleation are repeated for a bulging nuclei, Eq. 2.1 becomes:

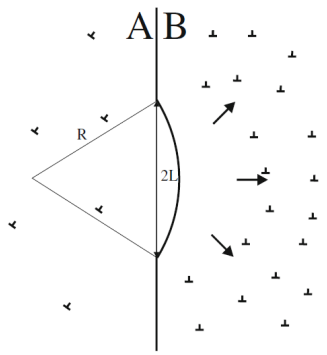

Figure 2.5: Heterogeneous "Nucleation" on a HAGB. The difference between the dislocation density is responsible for the driving force. Bulging boundary at the AB interface contributes the reduction of free energy by reducing the total amount of defects towards an equilibrium value.

$$\rho_{Crit}^{DDRX} = \left(\frac{20\ \dot{\varepsilon}\ \gamma_{GB}}{3\ bLm\tau^2}\right)^{1/3} \tag{2.2}$$

Unfortunately, if one uses a dislocation balance (generation and annihilation) model, then an iterative procedure must be implemented to approximate this critical value as performed by Bernard et al. [57] and Beltran et al. [58].

Although mathematically not modeled, authors who worked on Al-Mg, Cu-Si and Cu systems reported a grain boundary bulging and sliding mechanism for DDRX nucleation [59–61]. In this nucleation theory, due to the orientation difference, during the deformation, the number of geometrically necessary dislocations lead to subgrain formation close to the grain boundaries. As Mittemeijer highlights [38], observations show that recrystallized grains did not resemble those of the apparent parent grains. It may be speculated that in these cases; local, relatively pronounced orientation variations occur in the immediate vicinity of grain boundaries. These observations may be correlated with another mechanism for DDRX nucleation. Regarding the orientation of the newly born grains, generally, the final textured microstructures are attained after

static recrystallization. These are associated with SBIM since there is a particular orientation relationship between the child and parent grains.

Furthermore, there are some reports stating that SIBM mechanism is found to be more dominant in the softening processes after the deformation in lowly strained materials (static recrystallization), yet there are not many publications focusing on characterizing this.

Previously, in Section 2.3, the saturation grain size D_{SAT}, which is attained during the steady state deformation range is said to have a power law-like relationship with the Zener-Hollomon parameter. Interestingly, Luton and Sellars have observed the DRX behavior of Ni and Ni-Fe alloys during high temperature deformation [43] and reported that the final predicted recrystallized-grain size is approximately the same based on bulging and subgrain coalescence mechanisms.

Finally, the origin of DDRX are the inhomogenities in the microstructure, such as precipitations, grain boundaries or any inhomogenity introduced during the deformation process. As the orientation of a recrystallized grain will depend upon the recrystallization site, the types of nucleation site is expected to have a strong effect on the final texture.

In order to have a broad understanding of the DRX behavior of an alloy, one should have deep understanding of the (1) nucleation mechanisms and (2) how DRX evolves i.e. its kinetics. Further discussion regarding this will be given in the Modelling section (Section 4).

2.4 Other Physical Processes

2.4.1 Deformation Induced Precipitation

In the literature, there are some reports showing the effect of deformation on the precipitation kinetics of secondary phases in microalloyed steels and nickel-base alloys.

This phenomenon, which can be named as "strain induced precipitation" or "dynamic precipitation" is particularly important for the industry since the amount of precipitates depend on the processing history of the work piece.

According to previous studies, the dynamics of both matrix and grain boundary precipitates can be affected by the applied strain.

Calvo et al. [62] and Thomas et al. [63] reported dynamic precipitation of both grain and twin boundary δ phase in Inconel 718. In addition to this, other studies can be found, reporting the effect of cold rolling on the precipitation behavior in Inconel 718 [64, 65]. Similarly, Monajati et al. [66] studied the precipitation kinetics in Udimet 720, a nickel-base superalloy, through stress relaxation tests and concluded that the relaxation plateau observed in the stress-time curves is due to γ' precipitation.

The deformation induced precipitation is mostly associated with the increase of the dislocation density upon deformation, thus creating nucleation sites and increasing diffusivity of the elements to precipitate. However, in the work of Lui and Mei [64, 65], the consistent fast precipitation kinetics of δ, even after recrystallization could not be explained by the abovementioned theory. Instead this precipitation is associated with the segregation of Niobium.

Furthermore, in some cases, the deformation may also be associated with the resultant precipitate size. Chen [67] reported the sizes of the nano-carbide precipitation during hot sheet deformation (20-50nm) to be much larger than those forming during winding ($<$5nm). The extent of this effect depends on the characteristics of the precipitate and the elements that form the precipitate.

Apart from the size, some authors also reported changes in the precipitate morphology as a function of straining [68–70]. These authors reported the changes in the δ phase morphology in Inconel 718. While δ is observed to be needle like in the absence of straining, it transforms to have globular morphology upon straining. This tendency increases as the level of strain increases.

Strain Induced Precipitation Behavior of 718Plus®

Similar precipitation behavior can be observed in 718Plus as well. McDevitt [71] has investigated the grain boundary precipitation and found that the amount of δ (sometimes referred to as η or a layered mixture of

the two, this is clarified in the following paragraphs) in the microstructure increases with increasing strain. In line with this finding, Covarrubias [72] has reported similar strain-precipitation relationship for contour rings forged at Frisa Forgings, Mexico. From these studies, it can be inferred that a threshold for solutionizing temperature exists, beyond which the kinetics of grain boundary precipitation substantially slows down.

Here, it is important to mention that since the morphology and precipitation kinetics of the grain boundary precipitates in 718Plus were found to be similar to that of δ phase of 718, they were initially identified as δ as well (Ni_3Nb, D0a, orthorhombic) [24, 28, 29]. However, it was later studied in depth by Pickering et al. [30]. These authors reported that the grain boundary precipitates mainly consist of layers of η phase (Ni_6Nb [Al Ti], D024, hexagonal) and accompanied with δ layers.

Later, Messe et al. [73] and Casanova et al. [74, 75] conducted detailed studies regarding the grain boundary precipitation of 718Plus. Based on the findings of these authors, it can be inferred that η phase can precipitate in two different morphologies. When this phase precipitates in the absence of strain, it adopts a lamellar morphology with coherent/semi-coherent interface with the matrix. However, during subsequent forging processes, these precipitates may be "carried" away from their (relative) original locations and forced to become incoherent, leading to a plate morphology. Thus, it can be concluded that the distribution and homogeneity of the strain within the work piece is of importance to have a good control of the grain boundary precipitation in 718Plus.

2.4.2 Interaction between Dynamic Recovery & Precipitation

The interaction between precipitation and recovery can take place in different ways. First, as the preferred precipitation sites are usually imperfections [76], dynamic recovery can delay the precipitation process. Second, in the opposite scenario, as recovery process is driven by the dislocation mobility, precipitations may reduce the efficiency of DRV. Finally, before the precipitation takes place, the constituents of the precip-

itating phases e.g. γ' forming elements may be impeding the dislocation motion to some extent.

The interaction between DRX and precipitation has been more attractive for researchers through the Zener pinning mechanism; however; as mentioned in the section 2.2, when the overall link between DRV and DRX is considered, the effect of the DRV-precipitation can be even observed in the final DRXed microstructure and should not be ignored.

2.4.3 Interaction between DRX & Precipitation

Similar to the relationship between DRV and precipitation, DRX can interact with precipitiation in a number of ways. The DRX may cause a decrease in the possible precipitation sites for secondary phases via decreasing the dislocation density. Thus, the "precipitation start" point may be delayed. As a second possibility, a finely distributed precipitation structure may cause a delay of the changes in the dislocation structure. This then reduces the probability of the DRX nucleation as it requires substantial amount of dislocation motion.

Moreover, depending on the volume fraction, size and strength, the precipitating particles may impede the motion of the high angle boundaries, slowing down or even stopping the DRX process. A study on the GH 720Li alloy by Zhang et. al. [77] focuses on the effect of primary γ' distribution on the grain growth behavior and reveals that inhomogeneous γ' distribution leads to different DRV and DRX behaviour, resulting in a bi-modal final grain size distribution.

Similarly, Lee and Hou looks at the influence of the precipitated phases on the recrystallization behavior of the alloy IN718 [52] and highlights a "particle stimulated nucleation(PSN)"-like behavior due to the precipitating phases (γ'' and δ).

2.4.4 Behavior of Dislocations upon Facing a Precipitation in γ' Strengthened Alloys

The interaction between second phase particles and dislocations is determined based on the size and coherency level of the matrix-precipitate interface.

When the second phase particles start to precipitate, usually they form a coherent interface with the matrix and their sizes are relatively small, around a few nanometers. As γ' particles grow in size, they are more likely to create a semi-coherent interface with the matrix. In this case, the dislocations can pass through by cutting them. When this interaction type is valid (i.e. particle cutting), the resulting strengthening will be determined based on the elastic interactions between the particles and dislocations. These interactions can be associated with lattice misfit, differences in shear modulus and SFE of the two phases.

The lattice misfit between the matrix and the precipitate will naturally slow down a moving dislocation, resulting in hardening. The shear stress (τ) to overcome when a dislocation faces the precipitate, in this case, is approximated by some authors [78, 79] and can be given as follows:

$$\tau \propto G_{\gamma'}\ \varepsilon^{3/2}\ (rf)^{1/2} \tag{2.3}$$

where ε is misfit strain (proportional to difference in lattice parameter of the two phases), r is the particle radius f and G are the volume fraction and shear modulus of precipitated second phase respectively.

However, the lattice misfit is usually kept small in modern superalloys to maintain coherency even for larger precipitates, this is why the strength contribution of lattice misfit is limited.

The force required for a dislocation to pass the particle will increase as the particle size increases, thus, the overall contribution to hardening will increase. Once a dislocation cuts through a shearable particle, the resulting structure will reveal an additional precipitate–matrix interfacial area which increases the overall energy of the lattice. The interfacial energy of an ordinary coherent particle (low lattice misfit) is relatively small, thus, this hardening mechanism contributes little to the strength

of alloys that contain low misfit precipitates.

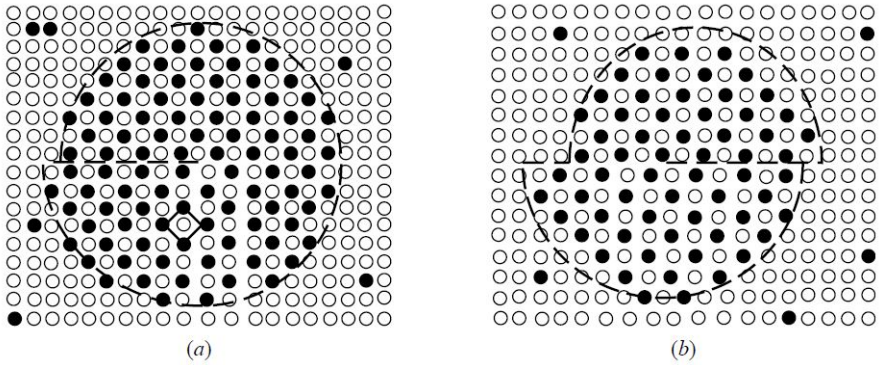

Figure 2.6: Schematic representation of a superlattice dislocation pair cutting a Ni_3Al particle in Ni matrix. [79]

However, when the precipitate is an ordered precipitate such as Ni_3Al in Ni base superalloys, cutting of the precipitate by a dislocation generates an unfavorable rearrangement of the aluminum and nickel atoms. This is schematically shown in Fig. 2.6 from (100) planar perspective. Imagine a dislocation pair traveling through this superlattice. The first dislocation passage (shown on the left hand side) disorders atom pairs along slipped portion of glide plane. The passage of second dislocation (shown on the right hand side) reorders lattice. This "unfavorable rearrangement" is called Anti-Phase Boundary (APB).

Since there is an additional energy associated with the APB, which depends on the degree of order in the lattice, dislocation motion is restricted. In Fig. 2.6 the right side of the particle is still disordered since the second dislocation has not passed through the particle's full diameter. The strengthening by APB is more significant than other factors when coherent, shearable particles are considered. This is due to the high energy of creation of the ABP, which is around ten times greater than interfacial energy in Ni base superalloys [14].

In contrast to the cutting mechanism, when the interface is incoherent, as in the case of overly aged precipitates, or if the particle separation

is relatively high, the cutting mechanism is replaced by dislocations looping around the particles.

In 1948, Orowan [80] reported his approximation of the stress necessary to make a dislocation loop around a particle:

$$\tau = \frac{Gb}{l} \tag{2.4}$$

Here G is the shear modulus of the matrix and l is the distance between the precipitates.

When a series of dislocations pass a particle pair, they will leave loops around the particles. Since these loops will stand at an equilibrium distance to the particles, the effective distance between the particles will decrease. In an analysis, Fisher et al. [81] find that no two dislocation loops are closer than 10 Burger's units.

Figure 2.7 shows the contribution of independent and overall stress increment contributions of different dislocation-particle interactions, i.e., looping and precipitation cutting. For the sake of comparison, contribution of solid solution strengthening is shown as well (marked with SSS).

Further, the overall Orowan stress contribution, which was originally proposed by Orowan [80], is modified by Brown & Ham [78] leading to Eqn. 2.5:

$$\sigma_{orowan} = \frac{MGb}{2\pi\sqrt{1-v}} \frac{1}{L_s} \ln\left(\frac{\pi}{2}\frac{r}{r_i}\right) \tag{2.5}$$

The expression 2.5 was successfully implemented by Ahmadi et al. [82] to simulate the room temperature yield strength of Allvac 718Plus®. Similar expressions have been implemented within this study as well to include precipitation effects. The modeling of precipitation hardening will be elaborated in the Section 4.1.5.

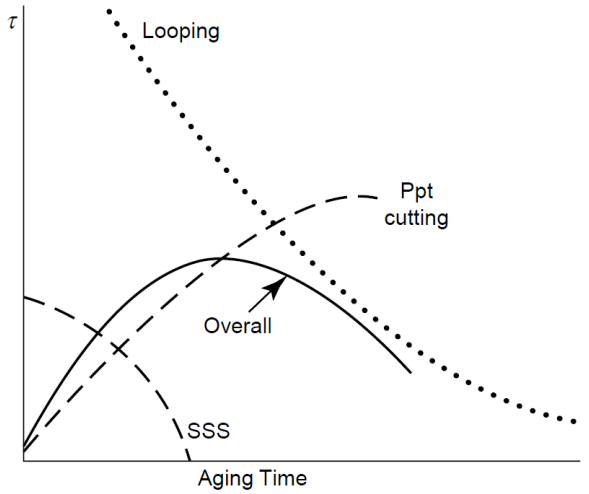

Figure 2.7: Schematic of different strengthening mechanisms, i.e., looping around particles, precipitate cutting and solid solution strengthening (SSS) in development of overall hardening response. [83]

Chapter 3

Experimental Methods, Characterization and Equipment

In order to obtain constitutive representations of the flow behavior and other metallurgically related properties of the alloy studied, a wide range of thermomechanical tests at different temperatures and deformation rates; and a number of characterization and numerical methods were employed.

In order to assess the phenomenological material constants with well known rate equations, the true stress - true strain curves were obtained by using two different thermomechanical simulators, namely Baehr 805A dilatometer and Instron 4507. Initial material characterization was done through SEM, optical microscopy and microhardness measurements. Solutionizing and other heat treatments took place in a handmade horizontal tubular furnace within at the facilities of Materials Science and Metallurgical Engineering Department of UPC. For the indirect observation of the precipitation behavior microindentation was employed. For an in-depth study of the microstructural components such as dislocation structure, precipitate state and interaction of these scanning transmission electron microscopy was used as main characterization tool. Post

processing of the raw flow curve data from compression tests, numerical operations and finding model parameters were done through Matlab 2014 and 2017 releases. This chapter gives somewhat detailed information regarding the most important aspects of these equipment.

3.1 Thermomechanical Treatment

3.1.1 Uniaxial Compression Tests

In order to simulate the industrial forming processes, small scale physical experiments are employed in the laboratory environment.

In the current case, to understand the hot forming behavior of the alloy 718Plus, uniaxial compression tests were employed. This type of mechanical testing is achieved by subjecting a cylindrical (or a cylindrical-like special form usually referred to as 'Rastagaev' geometry) sample to compression between two parallel punches.

Three different compression test approaches are employed, namely single hit compression tests, stress relaxation tests and single hit compression tests with prior holding to assess effect of second phase particles. The details of each test routine is given in Section 3.1.2. These tests are conducted at high temperatures in the range of $900 - 1050^o\,C$ corresponding to industrial deformation windows. The details regarding the equipment used for uniaxial compression tests are given in section 3.1.3.

In uniaxial compression testing, it is known that when the strain levels attain beyond 0.7 the deformation homogeneity and deformation induced self-heating of the sample starts to impede with accurate measurement of the material response. A broad review and guideline on accurate compression testing is reported by Jonas [84]. A representation of a compression test sample being deformed and the no-deformation (dead) zones are shown in Fig. 3.1. Because of these natural limitations, maximum strain is kept below 0.7 for all the tests.

The precipitation or RX kinetics can be determined by metallographic inspection of specimens from interrupted tests. However, onerousness process and the uncertainty added by the cooling process (precipitation

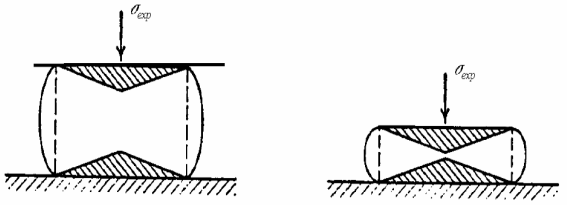

Figure 3.1: Schematic representation of a compression test sample after small and large deformation [85]. Shaded regions are no-deformation zones.

may start and/or continue during the cooling process) are the greatest drawbacks of this method. As an alternative, mechanical testing such as double hit (see author's work [86]) or stress relaxation tests have been proposed. Determination of kinetics of precipitation or DRX through double hit tests require one test for each holding time, which tremendously increases the number of tests necessary to conduct. Stress relaxation tests are appealing because they seem to be the most efficient way to track this kind of processes. In this work Baehr 805 A/D machine is used to perform these. The process details are given in Section 3.1.2.

Upon analysis of the compression tests where self-heating of the sample during deformation is observed to reduce the material stress response, this should be corrected with appropriate models. During some of the test performed within this study, on-sample thermocouples were employed to track the temperature increase during the deformation process.

Figure 3.2 shows the surface temperatures of the samples during the course of deformation for tests conducted at $1000^o\,C$ with different strain rates (1, 0.1, 0.01, 0.001 s^{-1}). As it can be seen the temperature change is below $\pm\ 5^o\,C$, by which it can be inferred that no self-heating correction is necessary.

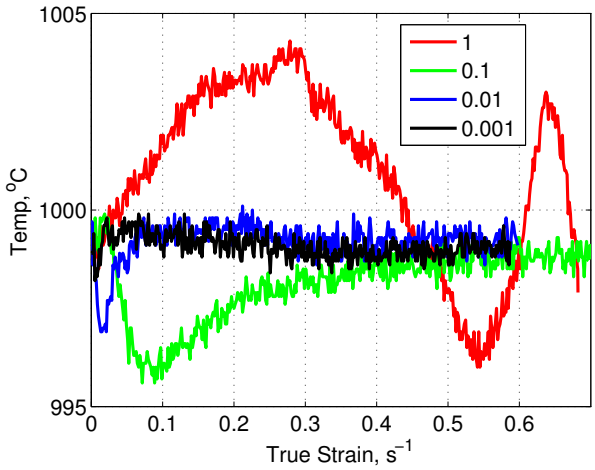

Figure 3.2: Temperature variation as a function of strain during uniaxial compression tests conducted at $1000^o\,C$.

3.1.2 Processing Route

Excluding the stress relaxation tests, all the compression tests performed in this work can be summarized in two sets i.e. hot compression tests without and with prior holding. Within this text, these tests without and with prior holding are occasionally referred to as Set 1 and Set 2, respectively.

Selection of Solutionizing Temperature

As it will be later shown in Section 5.2, a study to determine suitable solutionizing routine was performed based on microhardness measurements. Solutionizing temperatures from 1000 to $1080^o\,C$ up to 1.5 hours solutionizing schemes were investigated. Based on the results, the solutionizing routine selected was $1050^o\,C$ - 1 hour. In the testing routine, this solutionizing treatment was followed by water quench.

Hot Compression without Prior Holding

Tests without holding consisted of four different temperature and strain rates, namely; 900, 950, 1000 and $1050^{o}C$, at strain rates of 0.001, 0.01, 0.1 and $1s^{-1}$. Final strain was varied between 0.5 and 0.65 due to the intrinsic limitations of compression testing, mentioned in section 3.1.1.

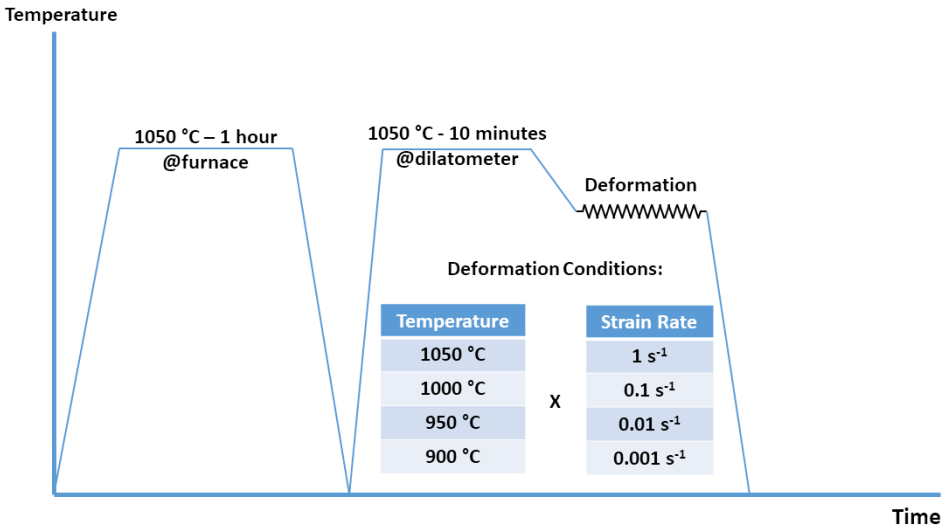

Figure 3.3: Processing route for Set 1 tests.

The thermomechanical cycle consisted of 3 steps. First, solutionizing for 1 hour at $1050^{o}C$ followed by water quench (the average grain size after solutionizing treatment was measured to be $73\,\mu m.$). Then 10 minutes at the same solutionizing (i.e. $1050^{o}C$) temperature followed by cooling down to the deformation temperature (at $1.5^{o}C/s$). Finally, compression testing after allowing a 3-minute interval for homogenization. This thermomechanical process is visualized in Fig. 3.3. After deformation, samples were quenched through the quenching system of

Baehr 805 A/D.

During all the tests, boron nitride powder and/or Tantalum foils were used to reduce the sample-punch friction.

Hot Compression with Prior Holding

Tests with holding on the other hand, were conducted at 920 and $940^o\,C$ with strain rate of $0.01\ s^{-1}$ on the samples held at $850^o\,C$ for a different amounts of time, similar to the approach given in [87]. The selection of the deformation temperatures in this set was based on TTT diagram of 718Plus [26, 88, 89]. Since the nose of the γ' transformation is around $920^o\,C$, this is selected as one condition. Furthermore, since the transformation line for γ' on the TTT diagram becomes asymptotic at $940^o\,C$, this is picked as the second condition.

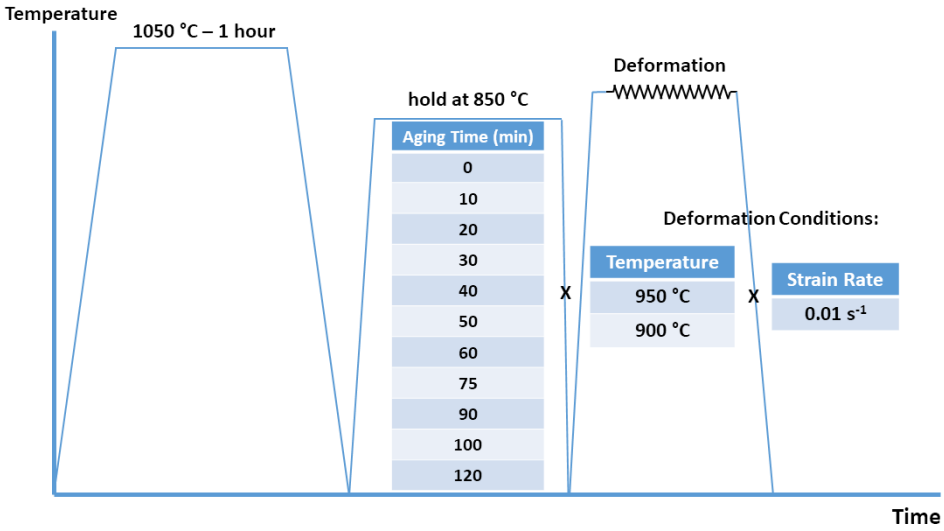

Figure 3.4: Processing route for Set 2 tests.

Deformation was terminated at approximately 0.4 strain in order to

stay below the maximum force capability of the equipment. Some samples were quenched slightly before the peak stress in order to preserve the structure before the DRX initiation and to be able to better investigate dislocation particle/second phases interaction.

The samples were solutionized at the same temperature ($1050^o\,C$) for 1 hour, followed by water quench. Then they were aged at $850^o\,C$ (for different amounts of time) followed by water quench. Finally, samples were heated directly to the deformation temperature and compressed after allowing 3-minutes for homogenization. If the tests are for microstructural investigation, they were interrupted at around $90\pm$3% of the peak stress. These samples were quenched with Argon purge with a rate of $7.5^o\,C/s$. The thermomechanical routine for Set 2 tests is visualized in Fig. 3.4.

Terminology Selection for Tests with Prior Holding

Since the aging temperature ($850^o\,C$) and strain rate during deformation ($0.01\,s^{-1}$) are the same for all samples in the tests with prior holding (Set 2), in the rest of the text these samples will be referred to with their deformation temperature and prior aging time. E.g. a sample deformed at $920^o\,C$ after 120 minutes of aging is named Sample $920^o\,C$-$120'$.

Stress Relaxation Tests

Stress relaxation tests were conducted with Baehr 805 A/D deformation dilatometer at 900, 920, 940, 960 and $980^o\,C$. The 10% initial strain before the start of one hour-relaxation was attained at $1\ s^{-1}$.

Stress relaxation cycle consisted of 3 steps as well. First, solutionizing for 1 hour at $1050^o\,C$ followed by water quench. Then 10 minutes at the same solutionizing temperature followed by cooling down to the deformation temperature (at $1.5^o\,C/s$). Testing after 1-minute interval for homogenization. After 1 hour of relaxation time, samples were quenched as in Set 1 tests. This process is illustrated in Fig. 3.5.

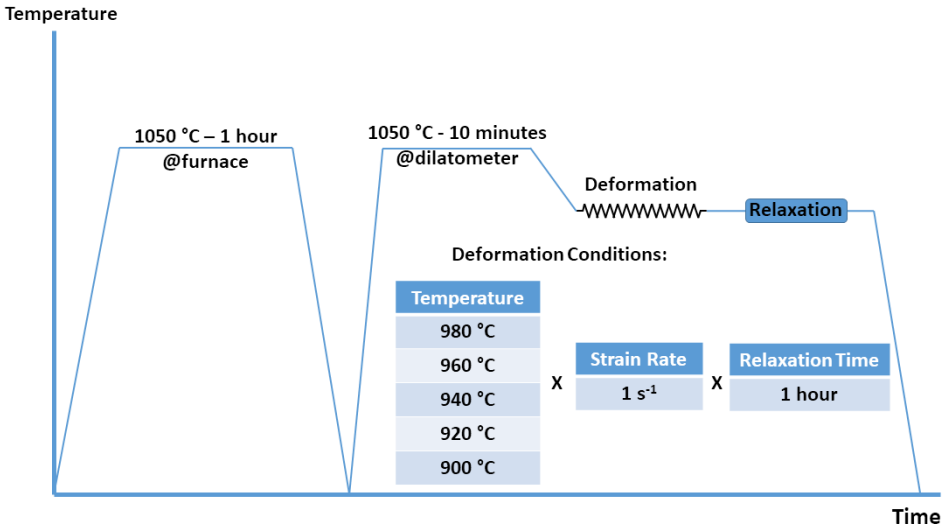

Figure 3.5: Processing route for stress relaxation tests.

3.1.3 Equipment for Compression Testing

Baehr 805-A/D Dilatometer

This thermomechanical simulator model, which is shown in figure 3.6 can be used to determine deformation parameters, to obtain static and post deformation time-temperature-transformation diagrams. The tool can attain heating rates up to $4000^o\,C/s$, quenching rates of $2500^o\,C/s$ and deformation speeds from 0.01 to $125\,mm/s$. Single or multi stage deformation schemes can be programmed easily. However, the machine's maximum allowable force limits the usage to small diameter samples when dealing with high strength alloys (such as superalloys).

Temperature measurement which drives the induction heating is achieved through a thermocouple welded on the sample surface. While the experiment control and sensitivity are extremely satisfactory, the sample size limitation creates a great deal of disadvantage from the characterization

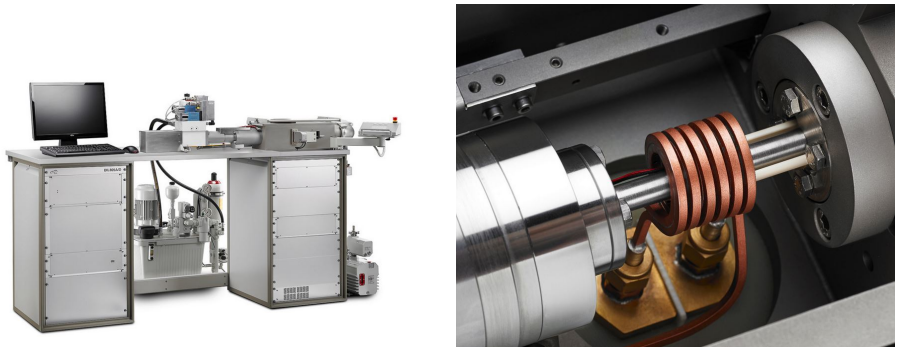

Figure 3.6: Baehr 805-A/D dilatometer. View of the setup (left), view of the sample chamber (right).

point of view.

For instance, the methodology of thin foil preparation for TEM examination requires larger cross-section area (at least a few milimeter larger than standard $3mm$ TEM disk size), thus making the machine unfavorable to produce material for further characterization.

Instron 4507 Thermomechanical Simulator

One of the thermomechanical simulators used in this study is Instron 4507 (see Fig. 3.7 bottom). This system consists of a load frame, in which the sample of the material tested is mounted. The load frame applies a tension or compression load to the specimen. The machine has a control console that provides the calibration, test setup, and test operating controls.

The machine has a crosshead drive and control system to apply loading and an accurate load weighing system which measures the loading of a specimen. Figure 3.8 shows the functional block diagram which summarizes the communication between these systems as well as the information flow in the machine. While this testing machine comes with an operation console and CPU, for the compression tests performed in this study, the machine was driven with an in house code with a simple

user interface on a dedicated PC. This control system is shown in Fig. 3.7 up.

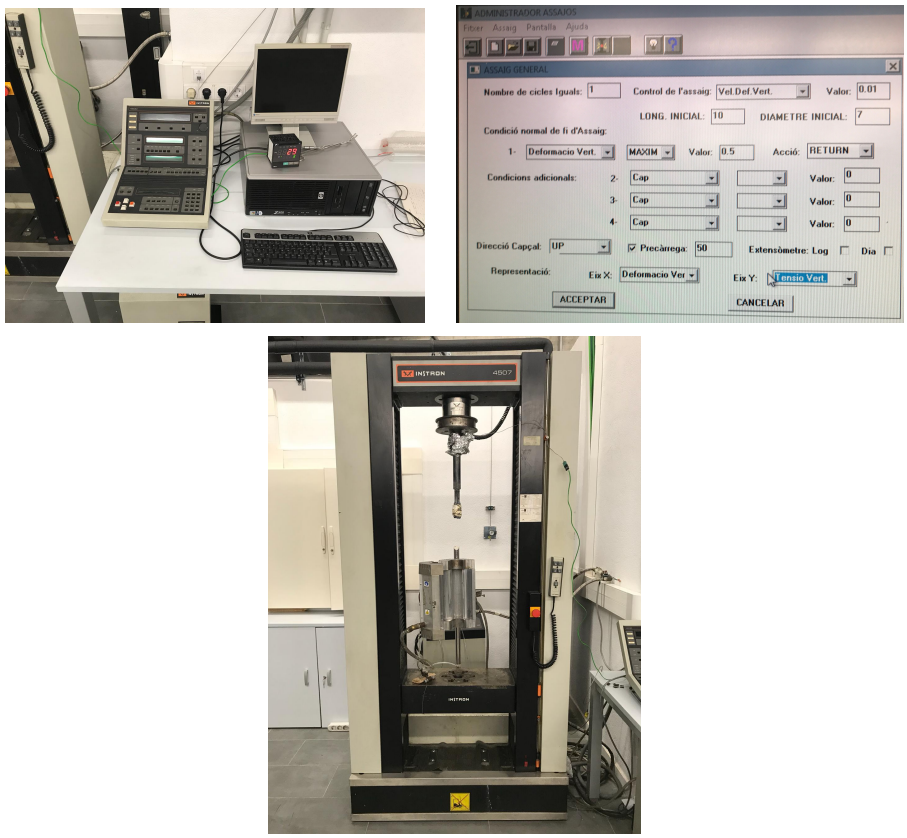

Figure 3.7: Control unit of Instron 4507 thermomechanical simulator (upper left), user interface of the control software (upper right) and main frame (bottom).

For compression testing, the 4507 is doted with a E4 ChamberIR by Research Inc. heating system with maximum heating capability up to $1100^o C$. The heating rate used with this furnace is approximately around $100^o C/min$. When necessary the samples were quenched either by water, with a mechanical system or argon purge was applied attaining

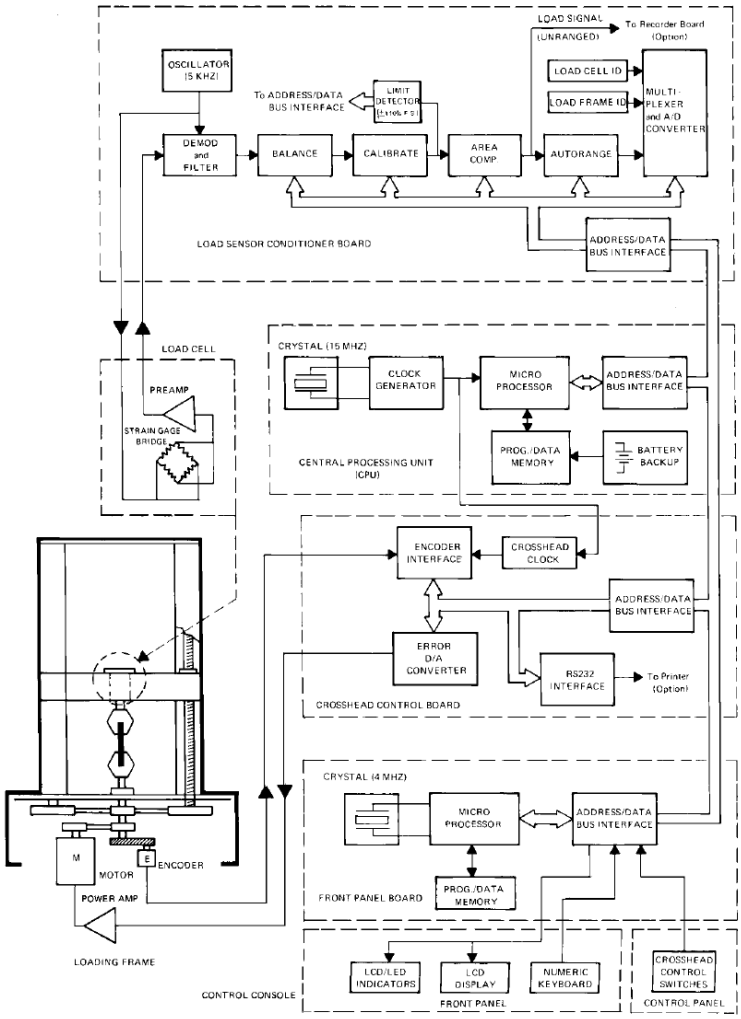

Figure 3.8: Functional block diagram of Instron 4507 thermomechanical simulator.

a rate of cooling around $7.5^o\,C/s$.

3.1.4 Cylindrical Samples for Compression Testing and Received 718Plus Billet

A billet of 718Plus was received as an initial material. The metallurgical investigation of the initial material is given in Section 5.1. From this billet cylindrical samples with diameters of 4, 5 and $7.5\,mm$ were machined. The aspect ratio of the specimens were 2, 2 and 1.5, respectively. The smaller samples with 4 and $5\,mm$ diameters were recommended sizes for the Baehr dilatometer 805 A/D. The bigger samples were used in Instron 4507. The received billed, an undeformed sample and a deformed sample are shown in Fig. 3.9.

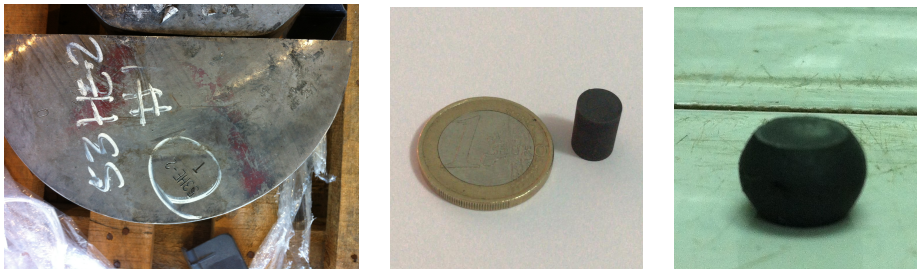

Figure 3.9: Received billet of 718Plus (left), an undeformed sample of $7.5\,mm$ diameter (middle) and a deformed sample from 805 A/D machine (right).

3.2 Characterization Methods

3.2.1 Microhardness Measurements

In order to indirectly assess the precipitation kinetics of the alloy and support the initial material characterization, as given in Section 5.3, microhardness measurements were employed. For the former, the aged samples were examined and compared with the available data in the literature.

To perform the hardness measurements, Akashi model MVK-HO testing machine was used (see Fig. 3.10). Vickers readings were reported after measurements with up to $0.5\,kg$ weight. For each measurement at least 30 readings were performed and the average was reported.

Figure 3.10: Akashi model MVK-HO microhardness testing equipment and integrated computer.

3.2.2 Microscopy Observations

Upon assessment of the larger scale properties such as grain appearances and sizes, optical microscopy and scanning electron microscopy is employed. γ' precipitation and its impact on dislocation is observed through transmission electron microscope.

Optical Microscopy

Specimens after deformation were cut by rotational cutters employing diamond disks. Cut samples were abraded by grit papers from 600 to 2500 sequentially. Following this, the specimens were polished using 6, 3 and 1 micron diamond particle suspensions until mirror like surface was obtained. If required, the final polishing was conducted by OP-S colloidal silica suspension with a particle size of 0.04 microns during 20 minutes.

Polished samples were attacked with Kalling's, modified Kalling's etchants.

Finally, observations were done on an Olympus GX51 type optical microscope with an integrated digital camera and image manipulation software. This setup is shown on Fig. 3.11.

Figure 3.11: Olympus GX51 used for optical microscopy.

Transmission Electron Microscopy

For the specimens to be analyzed in TEM, areas with a maximum thickness of $100\,nm$ were required so that electron transparency could be achieved. The wider these zones are, the more reliable results are obtained. To achieve this, the sample preparation routine is given in Section 3.2.2.

TEM examinations were performed through a Jeol ARM 200F type of microscope, located at Institute Jean Lamour (Nancy, France). An acceleration voltage of 200 kV was used. A representative photo of this tool is shown in Fig. 3.12. All samples were plasma cleaned in order to remove surface oxides and impurities before TEM.

Figure 3.12: Jeol ARM200F Transmission Electron Microscope.

TEM basically consists of a few condenser lenses (electromagnetic converging lenses), to focus the produced electron beam onto the specimen, an objective lens to form diffraction on the back focal plane and the

image of the specimen on the image plane, and finally a number of lenses (sometimes referred to as projector lenses) to alter the magnification of the images and/or diffraction pattern. A schematic representation of image creation in TEM is given in Fig. 3.13

The very first crossing of electron beam is the gun lens. Then the condenser lenses illumination of the specimen is controlled and arranged; for instance to be parallel or converged etc. Modern microscopes may have three or more condenser lenses, making them capable of obtaining wide parallel illumination, up to $50\,\mu m$ and convergence angles without any alteration of objective lens, aperture or beam itself.

When the specimen thickness is low enough, a high rate of incident electrons are elastically scattered, which are then focused through the objective lens to form a magnified image. Recent microscopes have a mini condenser lens just above the upper objective pole and the vertical location of the specimen corresponds to objective lens. Through this arrangement, the pre-magnetic field of the objective lens is created and helps controlling the illumination of the electron beam on the specimen.

To obtain diffraction patterns, a diffraction lens is used whose strength is tuned so that the front focal plane of the diffraction lens coincides with the back focal plane of the objective lens.

To further magnify the image, so called projector (or projective) lenses are used. Other than these, a number of dynamic deflection coils are used in the TEM column to adjust the beam position and angle. These are used to raster the electron beam on the specimen to form STEM images.

Microscopes may as well have image and beam deflection coils, mono chromators, detectors with different functionalities, aberration correctors etc. which help inducing or extracting data from the interaction between source electrons and specimen. Further details regarding the TEM technology may be found in an exhaustive text on TEM by Williams & Carter [90]

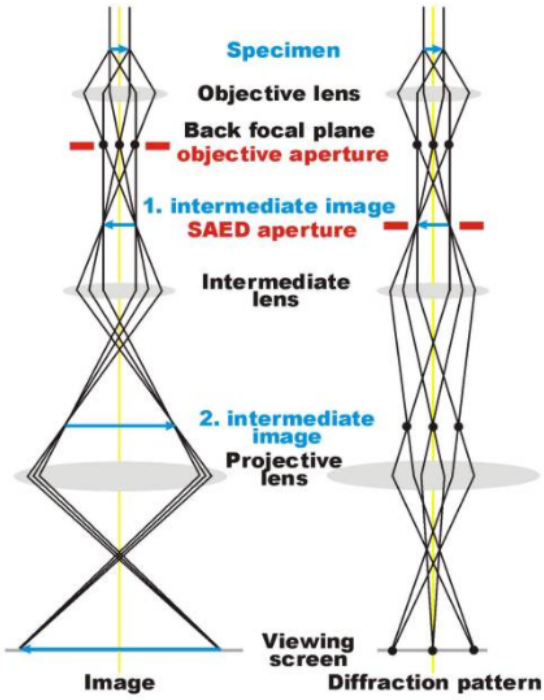

Figure 3.13: Schematic of imaging and diffraction in TEM.

Electron Imaging Mechanisms and TEM Modes

In general four different physics can be discussed regarding constrast mechanisms. Diffraction (1), mass (2), atomic number (3) and phase contrast (4). Diffraction mechanism obeys Bragg's physics. The variation of the diffracted beam intensity induced by the microstructure can be mapped by selecting the desired diffraction spot using small objective apertures. This creates an extremely important mode of TEM, called dark field imaging. The atomic number and mass contrast are due to the difference between the scattering powers of the elements that constitute the specimen. Mass contrast is the main mechanism for high resolution STEM images acquired by a high-angle annular dark-field detector. Finally, phase contrast, which arises from the interference of the primary

beam and the diffracted beams is specifically dominant for more special cases such as Lorentz microscopy and HRTEM. This is responsible for lattice fringe images.

Observations with transmission electron microscopy are based on four different approaches. First one consists of bright and dark field imaging, weak beam dark field imaging and high resolution electron microscopy. These techniques take the advantage of diffraction, mass and phase contrast of scattered electrons. Second approach is the scanning transmission electron microscopy, where focused electron beam is rastered on the specimen and transmitted electrons are collected in reciprocal space. Most of the time, camera length is arranged such that the atomic number contrast is used to form an image which is an extremely important observation technique in modern microscopy. Third approach is referred to as analytical microscopy and it is based on using the signals generated due to the interaction between specimen and incident beam to extract valuable information on the chemistry of the specimen. This method takes the advantage of two tools: energy dispersive X-ray analysis (EDS or EDX) and electron energy loss spectroscopy (EELS). Finally fourth approach is high resolution transmission electron microscopy where low-index zone axes images with high magnifications are used to obtain images of atom columns. In this technique, the signals obtained show contrast variations which can be perceived as discrete peaks. The images formed based on these signals are generally referred to as lattice images and when necessary conditions are satisfied, they correspond to atom columns. As mentioned above, the phase relationship between the electrons leaving the specimen is responsible for the image formation in HRTEM, and the contrast of HRTEM images depends severely on the sample thickness. It should not be forgotten that contrast of HRTEM images do not necessarily have a direct correlation with the atomic positions, thus interpretation of HRTEM images requires image simulation(s).

When the discussion is reduced to TEM only, it can be said that there are two modes of operation, i.e. imaging mode and diffraction mode. In the latter case, the diffraction pattern is projected to the fluorescent screen as mentioned previously. For the other mode, imaging,

on the other hand, different image contrasts may be formed depending on the electrons selected to create the image. If this includes transmitted electrons, then the image formed is referred to as *bright field image*. Bright field recordings appear as grey scale images due to three types of contrast sources: thickness and mass contrast, phase contrast and diffraction contrast. Due to this fact, thin parts and/or parts which are light in mass appear to be brighter and vice versa. In bright field images, parts which satisfy the Bragg condition in a crystalline specimen appear dark while amorphous regions or regions which do not satisfy Bragg condition appear bright.

When the specimen in TEM is examined in diffraction mode, an electron diffraction pattern is obtained which consists of a very intense central point which is formed by the transmitted beam and other points (or rings) relatively lower in intensity formed by diffracted electrons. In crystalline materials this diffraction of electrons occurs at a fixed angle which is driven by the Bragg condition. The beauty of TEM comes into the scene with the ability of selecting one or more diffracting electron beams (preventing others to form part of the image) by employing an objective aperture or by changing the angle of incident beam. An image formed through this process is usually called as a *dark field image*. In dark field images, the zones corresponding to the selected beam(s) appear relatively lighter when compared to other regions of the image.

Interpretation of TEM images is a very complex task and requires prior knowledge and experience of the material examined (or similar). Furthermore, during most of the operations, the analysis is combined with an Energy Dispersive Spectroscopy (EDX or EDS) to obtain information on the chemical composition of the specific regions in the specimen.

Within this work, bright and dark field TEM, weak beam dark field TEM, TEM diffraction, STEM combined with HAADF, ADF and EDX mapping approaches/methods are employed. The analysis of the obtained diffraction patterns are conducted through CrysTBox tool [91]. For contrast adjustments and image post processing such as 2D measurements, Gatan Digital Micrograph tool is used. For precipitate size

measurements, at least 100 measurements were taken.

Sample Preparation for TEM

Samples which were of interest for TEM observation were first cut and then subjected to standard grinding and polishing routines until obtaining a thickness of apprx. 60 micrometers for ion-mill finishing and 20 micrometers for electropolish finishing. The final polishing was always terminated by a grinding paper 2000 or above.

Figure 3.14 shows one of the ion-milling equipment used in this study, Fischione Model 1010 located at the Metallurgical and Materials Engineering Department of Middle East Technical University (METU). After polishing, the specimens were subjected to argon ion-milling with an acceleration voltage of 4-5 kV and an angle of attack about 15 to 20 degrees until a hole is obtained (4-6 hours apprx.). The process was finalized by 10 minutes at 7 degrees and 2 minutes at 3 degrees. Based on this prescription, some samples have shown wide observable areas on TEM while others failed dramatically.

Figure 3.14: Ion milling equipment used for the preparation of some TEM samples.

The alternative to argon ion-milling is electropolishing. Figure 3.15 shows the equipment and sample holder used. Since the sample thickness is extremely small, the sample is first wrapped into an aluminium

Figure 3.15: Electropolishing equipment, Struers Tenupol (left) and its sample holder (right).

foil and then placed into the holder. The foil always contained a hole corresponding to the center of the sample. Samples were electropolished with 5% perchloric acid in ethanol at $32\,V$ at $-10^{o}\,C$.

Finally, some TEM samples were obtained through Focused Ion Beam (FIB), where similar to the conventional argon ion-milling, the specimen is bombarded with ions to extract a thin foil. However, although this technique is very convenient in terms of runtime, the amorphization of the sample is a great drawback.

When all of these methods are considered, the best TEM sample preparation routine is achieved through electropolishing. However there is a great risk of losing or damaging the sample. Thus an optimization of the usage of these routines should be considered.

Chapter 4

Modeling of High Temperature Deformation

As mentioned in section 1.2, modeling the physical processes taking place during hot deformation has great industrial and academic importance.

There are a few remarks which should be mentioned regarding the importance of research in material modeling. Firstly, it has been seen that fully empirical methods which do not consider any physical mechanisms related to the process do not perform satisfactorily when one would like to use them to increase product quality and cost savings. Secondly, there are also microstructural models which satisfactorily express the optimum processing routes and material properties; however, these are doomed to partially rely on empirical expressions. Thirdly, the industrial experiments usually take place at large scales and thus, they are not cost efficient. Finally, physical experiments in the laboratory environment with small scale samples are not capable of simulating the whole processing window.

The material models are constructed based on observations. Thus they help researchers simulate the material under different processing conditions and more importantly they trigger new experimental studies/approaches which in turn augment the knowledge regarding the responsible mechanisms of particular material behaviour during hot deformation. This circuit is completed when new approaches are born to

optimize the material properties and/or processing routes.

In this chapter, the approach of author's hot deformation modeling is given together with necessary background from literature. In the formalism of flow curve modeling, until the initiation of dynamic recrystallization, the overall flow behavior is dictated by the "hardening" curve (sometimes referred to as dynamic recovery curve). To model this section, dislocation density based models are found extremely useful and have been evolving since ever introduced. A summary of relevant models is given in Section 4.1 of this chapter. In the same section, finally *The Estrin - Mecking - Bergstrom Model* is introduced. This model and its derivatives, which are extensively employed in this work, are explained in this chapter. The approach to include the effect of second phase particles is as well explained in Section 4.1.5.

Once the DRX starts, the total flow stress is calculated using a mixture rule as shown in the Eq. (4.1).

$$\sigma = X_{RX}\ \sigma_{RX} + (1 - X_{RX})\ \sigma_{wh} \tag{4.1}$$

where X_{RX}, σ_{RX} and σ_{wh} represent the amount recrystallized, stress response of the recrystallized material and stress response of the work-hardened material, respectively.

With the background provided in this chapter, the reader will understand how X_{RX}, σ_{RX} and σ_{wh} are revealed and used to model the whole hot flow behavior of the alloy.

4.1 Dislocation Density Based Hardening Models

Modelling of forming processes and predicting stress strain behaviour for a wide range of temperatures, strain rates and material chemistry has been a challenge for years. There have been numerous attempts in the past to model work hardening based on dislocation concepts. In this chapter, a number of dislocation density based materials models will be reviewed and compared.

Again, the reasons for formulating materials models based on dislocations is to accurately capture the physical behaviors of materials at a micro-scale. The applications of such models can be used in either creep or constitutive predictions as it will be seen in this chapter.

The development of physical or dislocation based materials models can be traced back to the 1950's. Some of the earliest scientists and metallurgists were working to explain the work-hardening or softening behaviors of various FCC or BCC metals specifically on the stage II hardening[1] of FCC metal crystals. [92]

It was generally concluded by many authors, through experimental studies and theoretical formulations, that a flow stress model for a metal crystal can be formulated by a unique relationship correlating the flow stress and the square root of the dislocation density and an evolutionary equation of the dislocation density.

However, there were no consensus on how exactly the stress-dislocation equation should be formed, and how to describe the complex dislocation evolution phenomenon. Some of the earliest works to formulate the dislocation evolutionary phenomenon include those by Seeger et al. [93] on dislocation pile-ups, and Basinski [94] on forest dislocations.

Some of the earliest comprehensive models were formed by Kocks [95], Bergstrom et al. [96, 97], and later by Mecking and Kocks [98] which was the milestone K-M Model.

4.1.1 The Bergstrom Model

The Bergstrom model was first designed to assess the homogeneous deformation behavior of BCC iron at room temperature. This model can be summarized starting with Eq. 4.2:

$$\sigma = \sigma_i + \sigma^* + \sigma_d \tag{4.2}$$

[1]Stage I occurs only during single slip in single crystals. Stage II is a linear hardening stage with a relatively high work hardening rate and occurs in both single crystals and polycrystals, independently of stage I.

where σ_i is the athermal independent stress, σ^* is the thermal stress which depends on strain rate (ε) and mobile dislocation density (L) according to the Eq. 4.3 and the component σ_d depends on the total dislocation density according to the Eq. 4.4 through the long-range interaction between dislocations.

$$\sigma^* = \sigma_u \left| \frac{\dot{\varepsilon}}{\phi\ bL} \right|^{1/m^*} \tag{4.3}$$

$$\sigma_d = \alpha\ \mu\ b\ \sqrt{\rho} \tag{4.4}$$

where α is a constant related to the efficiency of dislocation strengthening, b is the Burgers vector, μ is the shear modulus, ϕ is an orientation factor and ρ is the total dislocation density.

In Eq. 4.3, $\varepsilon = \phi\ b\ L\ \nu$ [96], where ν is the average velocity of the mobile dislocations which can be calculated as $\nu = \left| \frac{\sigma^*}{\sigma_u} \right|^{m^*}$. In the latter expression, σ^* is the effective stress acting on a dislocation, σ_u is the effective stress giving the dislocation an average unit velocity, and m^* the temperature-dependent material constant.

Through Eq. 4.4 and 4.3, the main equation, Eq. 4.2 can be expressed as follows:

$$\sigma = \sigma_i + \sigma_u \left| \frac{\dot{\varepsilon}}{\phi\ b\ L} \right|^{1/m^*} + \alpha\ \mu\ b\ \sqrt{\rho} \tag{4.5}$$

The rate equation for the immobilized dislocations ρ_i can be expressed as follows:

$$\frac{d\rho_i}{d\varepsilon} = U - \frac{dr}{d\varepsilon} - \frac{da}{d\varepsilon} \tag{4.6}$$

where U is the rate at which the mobile dislocations is increased by the creation and/or re-mobilization processes, $\frac{dr}{d\varepsilon}$ is the rate at which immobilized dislocations are re-mobilized, and $\frac{da}{d\varepsilon}$ is the annihilation rate. It has been assumed that the mobile dislocation density is much smaller than the total dislocation density, thus the total dislocation density ρ can be approximated as the immobile dislocation density ρ_i. U can be

calculated as inversely proportional to the mean free path of the mobile dislocation as follows:

$$U(t) = \frac{v\ L}{s(t)} \tag{4.7}$$

The term $\frac{dr}{d\varepsilon}$, the rate at which immobilized dislocations are re-mobilized can be simply written as the following

$$\frac{dr}{d\varepsilon} = \theta_1 \rho_i \tag{4.8}$$

where θ_1 is a material constant independent of strain, and ρ_i is the immobile dislocation density. The annihilation term $\frac{da}{d\varepsilon}$ is divided into three processes by Bergstrom. They are mobile dislocation annihilating each other, mobile and immobile dislocations annihilate each other, and mobile dislocation annihilating with microstructure surfaces such as grain boundaries. It has been postulated by Bergstrom that the mobile dislocations annihilation rate is proportional to the square of the mobile dislocation density. The immobile and mobile dislocation annihilation rate is proportional to the product of mobile and immobile dislocation densities, and the mobile to surface annihilation rate is proportional to the product of the strain independent annihilation space L and the mobile dislocation density. $\frac{dr}{d\varepsilon}$ can then be expressed as the following:

$$\frac{da}{d\varepsilon} = \lambda_1 L^2 + \lambda_2 L \rho_i + \theta_2 N L \tag{4.9}$$

where λ_1, λ_2 and θ_2 are strain independent constants. From Eqs. 4.7, 4.8 and 4.9, 4.6 can be written as the following, assuming that the mobile dislocation is time independent.

$$\frac{d\rho_i}{d\varepsilon} = U(\varepsilon) - \theta_1 \rho_i - \lambda_1 L^2 - \lambda_2 L \rho_i - \theta_2 N \rho \simeq \frac{d\rho}{d\varepsilon} = U(\varepsilon) - A - \Omega\rho \tag{4.10}$$

$$A = (\lambda_1 - \lambda_2)\, L^2 + (\theta_2 N - \theta_1)\, L \tag{4.11}$$

$$\Omega = \theta_1 + \lambda_2 L \tag{4.12}$$

If U, the rate of immobilization and annihilation of mobile dislocations are assumed to be strain independent, and Ω, the probability of re-mobilization and annihilation between immobile and mobile dislocations is assumed to be small, then the following stress strain relation can be attained.

$$\sigma = \sigma_{i0} + \alpha G b \left\{ \frac{U - A}{\Omega} \left(1 - e^{-\Omega\varepsilon}\right) + \rho_0 e^{-\Omega\varepsilon} \right\}^{1/2} \tag{4.13}$$

$$\sigma_{i0} = \sigma_i + \sigma_u \left[\frac{\dot{\varepsilon}}{mbL} \right]^{1/m^*} \tag{4.14}$$

The above model has been extended to predict behaviors of FCC polycrystal [97]. Accordingly Eq.4.7 can be expressed as follows:

$$U(\varepsilon) = \frac{1}{100\theta b s(\varepsilon)} \tag{4.15}$$

where θ is an orientation factor about 0.5 for BCC and 0.32 for FCC. For FCC, due to fewer slip systems and limited cross slip, the dislocation evolutionary equation can be modified to be the following:

$$\frac{d\rho}{d\varepsilon} = \frac{1}{100\theta b \left[s_0 + (s_1 - s_0)\, e^{-k\varepsilon} \right]} - \Omega\rho \tag{4.16}$$

where s is the mean free path of mobile dislocation. s_0 is an equilibrium value, and s_1 is the initial condition of s at $\varepsilon = 0$. If $\Omega = 0$, then the stress strain relation can be revised to be the following:

$$\sigma = \sigma_{i0} + \alpha G b \Big[\rho_0 + U_0\, \varepsilon + \frac{U_0}{k} \ln\Big(\frac{s_0 + (s_1 - s_0)e^{-k\varepsilon}}{s_1}\Big) \Big]^{1/2} \tag{4.17}$$

where $\rho_0 = \rho$ at $\varepsilon = 0$ and $U_0 = 1/100\theta b s_0 = 1/b s_0$. The reports by Bergstrom et al, [96] and [97], are limited to uniaxial strain with homogeneous deformation under ambient temperatures. Modified versions

of these models have taken higher temperature deformations into consideration [99]. It was proposed by Bergstrom from experimental studies that the recovery parameter Ω should be separated into an athermal and a thermal term as follows.

$$\Omega = \Omega_0 + \Omega(\dot{\varepsilon}, T) \tag{4.18}$$

The validity of the above model has been shown by many, including [96, 97, 99], to correlate quite well with experimental results. Despite its well organized dislocation evolutionary equation (three parameters, U, A, and Ω), its treatment on the contribution of various types of dislocations (mobile, immobile) would be further advanced by other models [100].

4.1.2 The Kocks Model

During high temperature deformation of metallic materials, the evolution of dislocation density is accepted to follow a balance between the generation and annihilation of dislocations. The following differential equation can be given to express this:

$$\frac{\partial \rho_{mobile}}{\partial \varepsilon} = \left.\frac{\partial \rho_{mobile}}{\partial \varepsilon}\right|_{stored} - \left.\frac{\partial \rho_{mobile}}{\partial \varepsilon}\right|_{recovered} \tag{4.19}$$

Kocks [101] showed that the Eq. 4.19 can be expressed as follows:

$$d\rho_m/d\varepsilon = (K_1\sqrt{\rho_{mobile}} - K_2\rho_m) \tag{4.20}$$

here ρ_m is the mobile dislocation density. The first term on the right hand side is associated with the dislocation generation. The glissile dislocations[2] are assumed to travel along a "mean free path" before becoming sessile (immobile). The mean free path is usually inversely proportional to the square root of dislocation density. Thus the generation term is proportional to the latter.

[2]The extended dislocation, consists of Shockley partials and a stacking fault, which can glide within its own glide plane; therefore, the accepted notation is glissile dislocation

The second term in Eq. 4.20 is assumed to obey first order kinetics. The coefficient K_1 can be given as follows:

$$K_1 = 2 \cdot \left(\frac{\theta_{II}}{\mu}\right) \cdot (\alpha' b)^{-1} \tag{4.21}$$

where θ_{II} is the athermal hardening rate. According to Eq. 4.21, since shear modulus is a function of temperature, K_1 can be said to be a temperature dependent constant.

K_2 on the other hand, which resembles the softening through recovery, is a function of strain rate and temperature. This is intuitive since the recovery process is thermally activated.

Furthermore, the hardening rate of a material can be given as follows:

$$\theta = \left.\frac{\partial \sigma}{\partial \varepsilon}\right|_{\dot{\varepsilon},T} \tag{4.22}$$

When the Taylor's equation (Eq. 4.4) is plugged into the dislocation balance formulation (Eq. 4.19) the following is obtained:

$$\theta = \theta_o \left(1 - \frac{\sigma}{\sigma_s}\right) \tag{4.23}$$

where θ is the initial athermal hardening rate which is associated with the second stage hardening rate (θ_{II}) and σ_s is the saturation stress in the absence of DRX (hypothetically for the cases where this is not applicable), α' is a constant. Here, it is seen that the hardening rate θ is linearly dependent on the stress σ.

4.1.3 The Roberts Model

The observation of hardening rate being linearly dependent on $1/\sigma$ (except lower deformation levels) lead Roberts [102] to consider the following relationship:

$$\theta = C\left(\frac{\sigma_{ss}}{\sigma} - 1\right) \tag{4.24}$$

where C is a constant. When the Taylor's equation (Eq. 4.4), dislocation density balance equation (Eq. 4.19) and hardening rate equation (Eq. 4.22) are plugged into Eq. 4.24, the following is obtained:

$$\frac{\partial \rho}{\partial \varepsilon} = k_1 - k_2\sqrt{\rho} \tag{4.25}$$

which gives the approach of Roberts in terms of dislocation density. Here one can note that the generation term k_1 is constant. This can be the case where the mean free path of dislocations (mentioned in the Model of Kocks) is restricted due to finely distributed second phase particles in the microstructure, or if very fine grain structure is dominating etc. The softening term, on the other hand, is proportional to the square root of dislocation density.

This approach is known to fail for low deformation levels, which already violates the first postulation of the model.

4.1.4 The Estrin - Mecking - Bergstrom Model

This model, considering the limitations of the previously mentioned models, proposes a hybrid hardening rate expression as follows:

$$\theta = \frac{\partial \sigma}{\partial \varepsilon} = \frac{A}{\sigma} - B\sigma \tag{4.26}$$

This is a linearly combination of σ and $1/\sigma$ type of dependencies. Through this combination, a wide range of validity and accuracy is expected to be achieved.

As in the previous section, if Eq. 4.26 is expressed in terms of dislocation density, one gets:

$$\frac{\partial \rho}{\partial \varepsilon} = U - \Omega\rho \tag{4.27}$$

Interestingly, Estrin-Mecking couple and Bergstrom arrive to the expression 4.27 from very different paths and considerations.

Here, Estrin-Mecking sees the deformation process as a balance between the hardening and softening, which is a view shared by Kocks.

Thus, they come up with a logical modification of the hardening term stating that the dislocation mean free path should not be $\sqrt{\rho}$ when it is further limited (by second phase particles or very fine grain sizes). In this case, replacing this with a constant is more logical.

The thinking of Bergstrom which goes to Eq. 4.27 is extremely different than that of the abovementioned approach. In this case, the dislocation density consists of two different parts, sessile and glissile dislocation densities. In addition to this, he postulates that the glissile dislocation density is independent of deformation while the sessile dislocation density during deformation is determined by the creation, immobilization, re-mobilization and anihilation of dislocations.

The complete expression which resembles this, is Eq. 4.10; however, for better comparison it can be shortened as follows:

$$\frac{\partial \rho}{\partial \varepsilon} = U - A - \Omega \cdot \rho \tag{4.28}$$

as mentioned in the section dedicated to Bergstrom Model, U is the rate of immobilization/annihilation of the glissile dislocations and Ω is the re-mobilization/annihilation rate of sessile dislocations. Finally, the extra term A is the rate of annihilation of glissile dislocations in grain boundaries or free surfaces. Obviously when it is considered that $U >> A$, the expression 4.28 becomes very similar to what Estrin-Mecking proposes.

The integration of Eq. 4.27 is quite complex when the terms U and Ω are thought as functions of deformation. However, as it is mentioned, one can assume first-order kinetics apply for the softening term, Ω and U remains constant if the grain structure is fine and fine particles exist in the structure. One can obtain the follwing relationship with the ease of these assumptions:

$$\sigma = (\sigma_{sat}^2 - (\sigma_{sat}^2 - \sigma_0^2)\ exp\ (-\Omega\varepsilon))^{1/2} \tag{4.29}$$

where $\sigma_0 = \alpha' \mu$ b $\rho_0^{1/2}$ and $\sigma_{sat} = \alpha' \mu$ b $(U/\Omega)^{1/2}$. Here, σ_o is the yield stress, σ_{sat} is the saturation stress which is defined as the

hypothetical stress level to be attained in the absence of dynamic recrystallization, α' is a geometrical constant, b is Burger's vector and μ is the shear modulus.

Work Hardening of the Recrystallized Material

As it will be covered later in this chapter, in Section 4.3.1, Avrami kinetics have been extensively employed to model DRX. In the use of Avrami kinetics, a common way to quantify the amount of softening is calculating the fraction of instantaneous stress with respect to peak stress (σ_p). An alternative approach to this is, finding the difference between the work hardening curve pertaining to the as-yet unrecrystallized grains and the experimental flow curve [103].

In a study published in 2011, Quelennec and Jonas [104] propose a new method for quantifying the amount of softening produced by DRX that is expressed in terms of the fractional recrystallization.

Conventionally, the normalization of the softening used to be based on the saturation stress (σ_{sat}). Rather than this, softening in this approach is described as the volume fraction of material that has undergone recrystallization. As a result, the current state of the material is correctly represented, and the fractional softening is described in a more physically appropriate manner. The biggest advantage of this method is that it does not require knowledge of the large strain steady state stress, which is extremely important if compression tests are employed.

While compression tests are used most widely to extract the parameters for modeling a specific material, some of the flow curves obtained by compression tests cannot reach the steady state flow while maintaining deformation homogeneity due to the natural limitations mentioned in Section 3.1.1. This newly proposed method addresses directly this limitation.

Furthermore, the hardening model given in Section 4.1.4 is generally implemented in such a way that the only hardening considered is the hardening of the initial material. However, it is well known that a fully softened grain will not experience the same hardening story as this 'new

hardening' will take place after DRX initiation. The hardening of a newly recrystallized grain is depicted in Fig. 4.1 by the curve denoted as $\bar{\sigma}_{rex}$.

The proposed method introduces the term σ_{RX}, which is defined by Eq. (4.30). σ_{RX} represents the average flow stress of the grains that have already undergone dynamic recrystallization.

If Eqs. (4.29) and (4.30) are compared, it is possible to see that the latter employs the critical stress as the analogy of saturation stress in Eq.(4.29). This is physically reasonable as it signifies that the stress required to continue the DRX after all the grains have undergone at least one cycle of recrystallization (and continued to work harden) is the same as the initial critical stress which was required to start the DRX process.

$$\sigma_{RX} = (\sigma_c^2 - (\sigma_c^2 - \sigma_0^2)\ exp\ (-(\Omega')\varepsilon))^{1/2} \tag{4.30}$$

where σ_{RX} is the work hardening behavior of the grains that have already undergone DRX, σ_c is the critical stress. Note that the softening rate parameter, Ω' is different from Ω as the former takes into account the birth of newly recrystallized grains, which are completely softened, thus different than the ones considered in σ_{wh} calculation.

Finally it should be mentioned that the saturation stress and critical stress are related to the softening parameters through the relationships:

$$\sigma_{sat} = \alpha\mu b\ (\frac{U}{\Omega})^{1/2} \tag{4.31}$$

$$\sigma_c = \alpha\mu b\ (\frac{U}{\Omega'})^{1/2} \tag{4.32}$$

This new approach is schematically represented in Fig. 4.1.

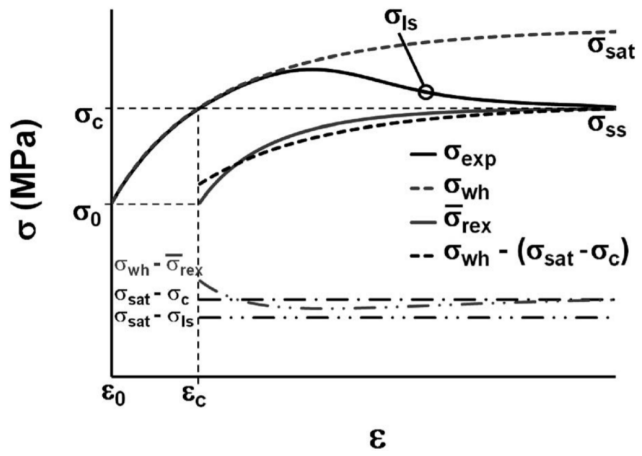

Figure 4.1: Schematic diagram of an experimental flow curve σ_{exp} and the derived work hardening σ_{wh} and work hardening of recrystallized material (σ_{rex}). Adopted from Quelennec and Jonas [104].

4.1.5 Accounting for The Effect of the Second Phase Particles

In the formalism of work hardening which is as well covered above, the following relationship given in Eq. (4.33), extended version of the well known Taylor's Equation (4.4) is accepted to well form the bridge between the flow stress (σ) and dislocation density (ρ).

$$\sigma = \sigma_i + m\mu\alpha b\sqrt{\rho} \tag{4.33}$$

In this relationship, α is a proportionality factor, μ is the shear modulus and b is the magnitude of the Burgers vector.

As mentioned in Section 4.1.1, σ_i is usually referred to as friction stress. The definition of this term is somewhat ambiguous [105] even if some authors relate it to the contribution of grain size hardening, precipitation hardening, solution hardening etc. Within this study, as the model results of the aged samples will be compared with the reference (solutionized) condition, the only contribution is assumed to be originating

from precipitation hardening. Thus, within the context of "accounting for the effect of second phase particles" it will be named σ_p.

To be fully described, the second term in Eq. (4.33) necessitates a model describing the evolution of the dislocation density fed in. To this end, the model given in Section 4.1.4, which is finally summarized in Eq. 4.28 is adapted to include the strength contribution of second phase particles during hot forming. According to this, the dislocation evolution in the time domain through Eq. (4.34):

$$\frac{d\rho}{dt} = U\frac{d\varepsilon}{dt} - \Omega\rho\Big[1 - \frac{g}{\sqrt{\rho}}\Big]\ \frac{d\varepsilon}{dt} \tag{4.34}$$

where t is time and ε is the strain. Similar to the original model constants, U is the athermal work hardening and the second term in the Eq. (4.34) represents dynamic recovery. The first term, U, has the form of $(= \frac{m}{b\ L})$, where L is the mean free path of dislocations, on which dislocations can travel until immobilized by a barrier (pile up) and/or obstacle (second phase/precipitate). Ω is a strain independent material constant representing the dislocation re-mobilization in the absence of precipitation. Note the damping term attached to this term which represents the effect due to the precipitation which was first proposed by Engberg *et al.* to limit the softening due to climb only [106–108].

In the second term, g can be expanded as $g = \ C\ (f_{prec}/r_{prec})$, where f_{prec} and r_{prec} represent volume fraction and radius of the second phase particles and C is a parameter, similar to the dislocation density factor introduced by Dutta et al. [109]. Here, it is important to mention that in this work, only up to moderate volume fractions of γ' with spherical morphology are considered, agreeing with the TEM observations.

The mean free path of dislocations is calculated based on the subcell diameter and precipitation. They were assumed to additively contribute to the immobilization of the dislocations which is given in Eq. (4.35).

$$\frac{1}{L} = \frac{\sqrt{\rho}}{K_{cell}} + \frac{K_{prec}}{L_{prec}} \tag{4.35}$$

where K_{cell} and K_{prec} are parameters which define the immobilization

effectiveness [110]. The original model [111] assumes an evolution from L_{start} to L_{end}. In the current case, this is assumed to be constant, which is a fair considering the original treatment was on ferrite. Moreover, for the solutionized material it is assumed that the cell spacing is smaller than precipitate spacing. Therefore, the hardening contribution from the precipitates is ignored in this case. The exact value of L_{prec} is calculated based on a statistical representation [112] of randomly distributed spherical particles whose reduced form is shown in Eq. (4.36):

$$L_{prec} = \sqrt{\frac{log(3)}{2\pi Nr} + \frac{8}{3}r^2} - \frac{8}{3}r^2 \tag{4.36}$$

where N and r are the number density and particle radius respectively.

Furthermore, in order to define both Eq. 4.36 and Eq.4.34, one needs a description of the volume fraction and particle size of the precipitates. For the alloy 718Plus, these can be obtained through numerical models for precipitation or based on experimental data. The radius data is presented by Radis and Zickler *et al.* [113,114]. As it will be retouched later, the static precipitation data of these authors are found to under-estimate the second particle radius when compared to the current findings for temperatures below $940^o C$. Thus, upon application these models have to be calibrated according to γ' radius observed in the deformed samples.

Precipitation Stress (σ_p) and its Components

During (hot) deformation, when a dislocation meets a precipitate, it can either loop around the particle, or cut through it. The former is usually called Orowan mechanism, the latter occasionally referred to as precipitation shearing. The stress contribution (the stress necessary to make a dislocation overcome all the obstacles on its way) of these mechanisms are given by Eq. (4.37) and Eq. (4.38) respectively.

$$\sigma_{Loop} = \frac{2.43\mu b_\gamma}{4\pi(L_p - 2r)}\ \beta\ ln\left(\frac{L_p - 2r}{2b_\gamma}\right) \tag{4.37}$$

$$\sigma_{Cut} = \frac{m\ \mu b_{\gamma'}}{r\sqrt{\pi w_q}}\ k_c\ \sqrt{f}\ \left(\frac{2\ \gamma_{APB} w_r\ r}{\mu b_{\gamma'}^2}\right)^{3/2} \tag{4.38}$$

where μ is shear modulus, b is the magnitude of Burgers vector, L_p is the interparticle spacing, r is the precipitate radius and γ_{APB} is the energy density of the planar anti-phase boundary. w_r and w_q are constants [115]. β and k_c are calibration constants taken from the approach of Fisk *et al.* [110].

Although the activity of these mechanisms can be observed qualitatively through TEM observations, the contribution of each cannot be quantified. Because of this, the overall contribution is assumed to be a weighted average of the two as given in Eq. (4.39).

$$\sigma_{Total} = f_{Cut}\ \sigma_{Cut} + (1 - f_{Cut})\ \sigma_{Loop} \tag{4.39}$$

where f_{Cut} is the volume fraction of precipitates passed by shearing mechanism. A straightforward solution would be obtained through calculating the fraction of sheared (cut) precipitates by using a size distribution function and assuming a critical size for mechanism transition from cutting to looping. However, in the current case, an inverse approach is used and f_{Cut} is reported as a function of aging time. Constants β and k_c are found based on the assumption that after two hours of aging at $850^o\,C$ the dominating mechanism is particle looping.

4.2 Kinetic Equations of Hot Forming

In the literature a simple and widely used approach could be found which relates the flow stress to the temperature compensated strain rate, known as Zener-Hollomon parameter (Z).

$$Z = \dot{\varepsilon}\ exp(\frac{Q}{RT}) = f(\sigma) \tag{4.40}$$

In Eq. (4.40), Q is the activation energy of deformation. Previous studies [116, 117] show that hot deformation process can be treated as

a thermally activated process and could be well described by strain rate equations similar to those implemented to describe creep. The parameter Z could be related to the flow stress via the following equations:

$$Z = \dot{\varepsilon}\ exp(\frac{Q}{RT}) = f(\sigma) = A'\sigma^{n'} \tag{4.41}$$

$$Z = \dot{\varepsilon}\ exp(\frac{Q}{RT}) = f(\sigma) = A''exp(\beta\sigma) \tag{4.42}$$

$$Z = \dot{\varepsilon}\ exp(\frac{Q}{RT}) = f(\sigma) = A[sinh(\alpha\sigma)]^n \tag{4.43}$$

where A, A', A'', n, n', β and α are material constants. In this context, α is usually referred as an adjustable stress multiplier (not related to the α in the previous sections) and chosen based on the behavior of $ln(\dot{\varepsilon})$ vs. $ln(sinh(\alpha\sigma))$. At the same time, it is possible to regard α as the inverse stress at which the Eq. (4.42) breaks.

These equations are mostly referred as "power law", "exponential law" and "hyperbolic sine law", respectively. While the power law is usually implemented in the cases with relatively lower stress levels, exponential law is used for higher stresses. On the other side hyperbolic sine law could be used in a wide range of deformation conditions.

The activation energy of deformation, Q, depends on the material being considered; however, upon the calculation the internal microstructural state is not taken into account. With the assumption of microstructure remaining constant, it is derived from an Arrhenius plot. Because of this assumption, the above mentioned constants (A, A', A'', n, n', β and Q) are usually referred as "apparent" material constants and therefore, this method is called the "apparent approach".

The readers interested in the origin of the Hyperbolic sine equation may refer to Hosford's and Cabrera's texts [85, 118].

Modification of the Apparent Approach

If the deformation mechanism is controlled by dislocation glide and climb, some modifications could be introduced to Eq. (4.43) to include more physical meaning in its modeling capabilities.

It was shown by Cabrera *et al.* [119] that if the temperature dependence of the elastic modulus and self-diffusion coefficient are taken into account, it is possible to take creep exponent as 5 and use self-diffusion activation energy instead of hot deformation activation energy.

Rewriting Eq. (4.43) for strain-rate and introducing the above mentioned modifications, Eq. (4.43) becomes:

$$\frac{\dot{\varepsilon}}{D(T)} = B \left[sinh(\frac{\alpha' \sigma}{E(T)}) \right]^{n=5} \tag{4.44}$$

In Eq. (4.44), $E(T)$ is the elastic modulus and $D(T)$ is the self-diffusion coefficient. These could be calculated for temperatures of interest via the following equations:

$$D(T) = D_0 \; exp(\frac{-Q_{sd}}{RT}) \tag{4.45}$$

$$E(T) = 2(1+\nu) \; \mu \tag{4.46}$$

where the temperature dependence of μ is obtained through [120]:

$$\mu(T) = \mu_0 \; exp \; (1 - \frac{T - 300}{T_m}) \tag{4.47}$$

For Ni-base superalloys, it is possible to take the Poisson's ratio, ν as $1/3$. Other appropriate values for μ_0, Q_{sd} and D_0 can be found in Ref. [120]. For Nickel, the self-diffusion activation energy is given as $Q_{sd} = 285$kJ/mol, and the diffusion constant D_0 as $1.6\text{x}10^{-4}$ m^2/s.

4.3 Modeling Dynamic Recrystallization

As mentioned previously in Section 2.3, Dynamic Recrystallization (DRX) is the responsible mechanism for softening which can be directly observed on hot flow curves. For correct modeling of DRX, a good understanding the mechanisms which play role on the initiation and progress of this process is necessary. To this end, Luton and Sellars [43] looked into

the DRX process in nickel and nickel-iron alloys during high temperature deformation. They draw a few important conclusions, some to be criticised afterwards. Firstly, the recrystallized grain size is uniquely determined by the flow stress, independent of temperature. The second important conclusion is that the stress dependence of the critical strain to initiate recrystallization is less than that of the strain occurring during recrystallization. This results in periodic recrystallization below a critical flow stress and continuous recrystallization above it. Furthermore, they report that the activation energy for deformation is determined mainly by the activation energy for dynamic recrystallization. In the light of this study, a few years after, Sah *et al.* [121] extended the original work and reported observations on multiple peak DRX. Later in 1979, Roberts *et al.* [122] published their findings on the kinetics of DRX. According to these authors, at a given temperature and strain rate, with larger initial grain size, a significant increase is observed in the critical strain for dynamic recrystallization and the strain to the maximum stress. While the maximum stress is independent of initial grain size, as the initial grain size is reduced, an increased work hardening rate prior to the onset of dynamic recrystallization is observed. In addition to increased work hardening rate, the time (deformation) necessary to reach steady state stress after the peak stress is significantly reduced as well. Furthermore, the steady-state stress and the dynamically recrystallized grain size are reported to be independent of the initial grain size. Perhaps the most important conclusion of this work is that the kinetic data can be described by an Avrami law with n = 1.2-1.3 and with n insensitive to changes in initial grain size.

There are some other models (see [123–128]) as well which attempt to involve more physically based representations such as the one reported by Montheillet in 2000 [123], where grains are modeled as spherical objects having a diameter and dislocation density. However, these models are more complex than phenomenological approaches (such as Avrami type of description) and do not necessarily agree with each other. Thus, within this work, DRX modeling is performed based on an Avrami approach which is explained in the next section (Section 4.3.1).

4.3.1 Avrami Model as a Representation of DRX Kinetics

While there is still an ongoing fundamental discussion about how to better model DRX nucleation and evolution, a long-standing approach is Avrami representation. From a certain point of view, DRX may be accepted as a solid state phase transformation with nucleation and growth. Based on this, the fractional softening is given, as a function of time as shown in the Eq. (4.48):

$$X = 1 - exp(-Bt^k) \tag{4.48}$$

here X is the recrystallized fraction, k is the Avrami constant, associated with the nucleation mechanism; t is the DRX time and B is the parameter associated with the nucleation rate and growth. The peak strain, ε_p is used as a reference strain to derive the time in the Eq. (4.48) as follows: $t = (\varepsilon - \varepsilon_p)/\dot{\varepsilon}$.

Together with Eq. (4.48), the relation co-used to assess the stress level is as follows:

$$\sigma = \sigma_{sat} - (\sigma_{sat} - \sigma_{ss})\ X \tag{4.49}$$

where the σ_{ss} is the stress level attained due to the balance between work hardening and dynamic softening. Here X is defined as the difference in the stress between the work hardening curve and the flow curve obtained through compression tests. Thus, X is expected to approach the unity when the steady state is achieved.

Upon the calculation of the term B in the Eq. 4.48, the half time for DRX, t_{50} was used. This reduces Eq. 4.48 to Eq. 4.50.

$$t_{50} = (\frac{0.693}{B})^{1/k} \tag{4.50}$$

Finally t_{50} is fit to Eq. (4.51):

$$t_{50} = K_t d_0^{m_t} \dot{\varepsilon}^{n_t} exp(\frac{Q_t}{RT}) \tag{4.51}$$

where, K_t, m_t, n_t are constants and Q_t is the activation energy for DRX process. As the initial grain size was the same for all the samples throughout this work, the term d_0 is ignored.

Chapter 5

Baseline Hot Flow Study of Allvac 718Plus®

In this chapter, the essential parameters of flow curves are extracted. By baseline, it is meant that the alloy is initially free of precipitates and grain size is large enough not to intervene with any parameter estimation. The parameters extracted are the peak stress and strain values, recrystallization kinetics, the saturation stress and their behavior as a function of processing parameters. The hot flow behavior observed based on the results first presented here form a basis to interpret the further relevant results, i.e. hot compression tests of aged specimens to reveal the effect of γ' precipitates.

5.1 Initial Analysis of the Batch Received for this Study

Triple melt (VIM, ESR, VAR) 718Plus^{TM} was received from Frisa Forgings, Mexico. The received material had a billet form having an average grain size of 62 μm. The Fig. 5.1 shows the optical microscopy (a) & (b), and scanning electron microscopy (c) & (d) of the received material. The investigated piece was cut from the center of the billet and prepared

with a modified Kalling's etchant. One can note the existence of annealing twins in the microstructure. At high magnification Fig. 5.1-(d) the presence of fine precipitates is evident.

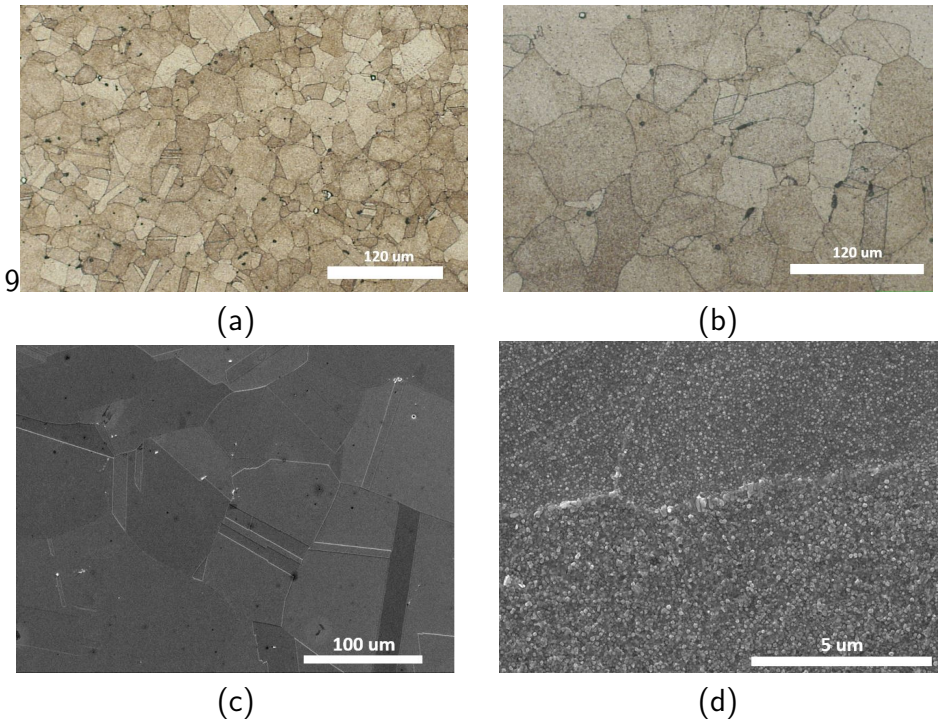

9

(a) (b)

(c) (d)

Figure 5.1: (a) & (b) Optical micrographs at 10 and 20x magnification respectively; (c) & (d) Scanning electron micrographs at 300 and 10k x magnification respectively.

The hardness value of the initial material is measured as 406HV, which implies that the material is neither in the solutionized, nor fully aged condition.

5.2 Solutionizing Study

The correct solutionizing treatment for this study should result in a precipitate-free initial microstructure with the smallest possible grain average size. To this end, a study was conducted in the range of $1000 - 1080^o\,C$; covering 30 minutes, 1 hour and 1.5 hours holding times. The resulting hardness values are shown in Table 5.1. Accordingly $1050^o\,C$ - 1 hour combination was selected. Although it is interesting to note that the hardness values indeed increase with increasing solutionizing temperature from $1000^o\,C$ to $1040^o\,C$, this fact is not further investigated due to the selected scope of the work.

Table 5.1: Resulting hardness values in Vickers (1 kg) for various solutionizing treatments.

^oC/Hold Time	5 mins	30 mins	60 mins	90 mins
1080	-	-	-	186
1060	-	201	191	188
1050	-	212	**192**	190
1040	-	220	217	204
1020	210	214	203	199
1000	212	206	200	195

5.3 Precipitation Behavior

5.3.1 Response of 718Plus® to Aging Treatment in the Absence of Deformation

As mentioned earlier in this chapter, the received material had a hardness of 406 HV. The average grain size was 62 μm. After solutionizing at $1050^o\,C$ for 1 hour, the hardness value was recorded as $192\,HV$.

Before starting the hot flow studies, one needs to understand the phase transformations which the material can undergo within the pro-

cessing window. To this end, the material was subjected to a series of heat treatments from 750 to $950^o\,C$ up to 1 hour hold times and hardness response was recorded for each treatment. Table 5.2 shows a comparison of the results of this work with previous studies for the common/similar data points. It can be seen that the difference in reported hardness values for the same data points can be as high as $100\,HV$, especially in the range of $900 - 925^o\,C$ where the precipitation kinetics are very fast. Thus, one can understand the importance of accurate time measurements in the heating cycle and quenching rates after treatment. Current study shows good agreement for the 6 minutes aging time with Ref. [26]; however, it differs somewhat from Ref. [89] as it can be seen on Table 5.2.

Table 5.2: Hardness results of aged 718Plus^{TM}: Comparison of different studies.

Source:	Srinivasan [89]			Xie [26]			Current Work		
C^o/ time	6 min	30 min	1 hr	6 min	15 min	1 hr	1 min	6 min	15 min
950	283	283	-	224	227	226	199	205	-
925	-	-	-	246	229	228	247	281	-
900	373	345	-	300	270	221	256	297	-
850	407	-	407	303	329	391	-	325	357
800	395	-	424	-	-	417	-	255-345	345
750	-	-	-	-	-	409	-	255	251
750	353	-	405	-	-	-	-	-	-

Based on the hardness values shown in Table 5.2 a PTT diagram (see Fig. 5.2) is constructed, in which the dots represent the resulting hardness measurements and are painted as a function of hardness (red color is highest). Although Xie. [26] noted that the hardness corresponding to initial γ' precipitation is 225 HV, **the transformation line in Fig. 5.2 was plotted for 245 HV**. At 850°C after 30 minutes, softening was recorded and this is in agreement with the study of Srinivasan [89].

This PTT plot is used to shed some light to the interpretation of the hot flow studies that are explained in the following sections.

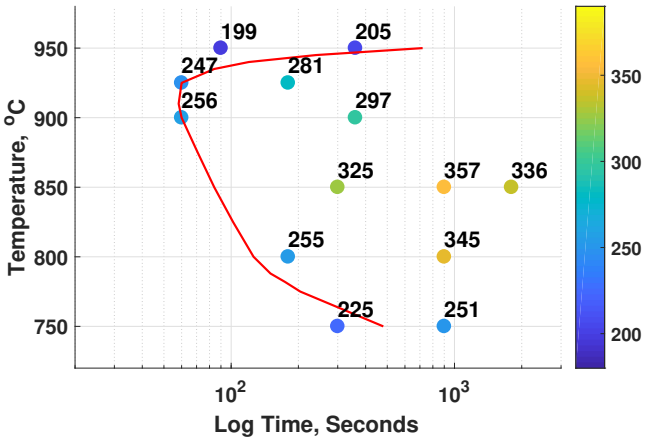

Figure 5.2: PTT diagram of 718Plus^{TM}. Red line denotes 245HV limit. Time axis is given in Hours for ease of comparison with [26, 89]

5.3.2 Stress Relaxation Tests

In addition to the short time aging treatment of the alloy without deformation as mentioned above (Section 5.3.1) an attempt has been made to track the initiation of precipitation when the alloy is predeformed. To this end, stress relaxation technique is used.

Figure 5.3 shows the obtained relaxation curves following a 10% deformation at a strain rate of $1s^{-1}$, and in the temperature interval from 900 to $980°C$.

Upon interpretation of these results, the relaxation of behavior is compared with those reported in the literature regarding superalloys [66, 129–131]. Based on this the relaxation curves observed at 960 and $980°C$ show a $\sigma = \sigma_{init} - S'' \ ln(1 + \beta t)$ like behavior (S'' and β are material constants and t is time), the tests conducted at $900°$C, $920°$C and $960°$C slightly differ from this definition when precipitation start is

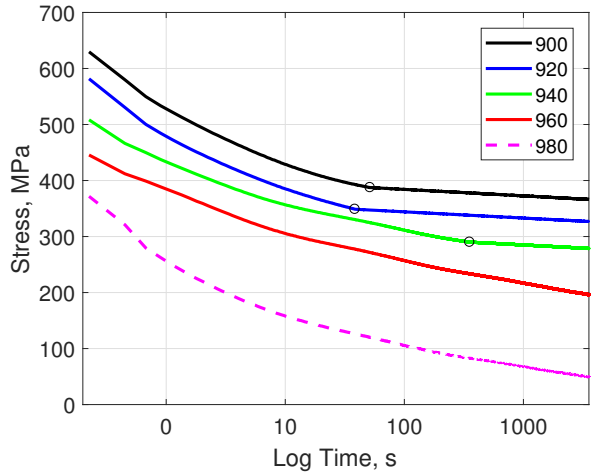

Figure 5.3: Stress relaxation curves recorded after subjecting the samples to a 10% deformation $1s^{-1}$.

captured. A less negative slope is observed when the material resists the relaxation, which is thought to be a natural effect of precipitation. The points where the recorded curves at 900, 920 and $940°C$ differ from the $\sigma = \sigma_{init} - S''\ ln(1 + \beta t)$ regime are marked with a dot on each curve. These points correspond to 39.8, 63.0 and 316.2 seconds for 900, 920 and $940°C$ respectively. When this is compared with the PTT curve (Fig. 5.2) a slight shift towards the shorter times is seen for precipitation start. For instance, while in PTT curve it is accepted that precipitation starts after around 120 seconds at $900^o\,C$ this value is around 40 seconds after 10% of prestrain.

The precipitation of γ' is confirmed by the TEM observations. A selected relaxation sample, $900^o\,C$, quenched slightly after the corresponding precipitation start point is selected for observation. Figure 5.4(a) and (b) show a dark field and bright field TEM image. Based on this recording, effectively, a fine precipitation took place in the matrix (the bright spots in the dark field image). The diffraction pattern shows the composite lattices clearly with weak superlattice reflections. The

precipitate and the matrix exhibit an orientation relationship. Dark field image have been recorded using 001 superlattice reflection, revealing the fine γ' precipitation (more on phase identification is given in Chapter 6). Furthermore, highly deformed microstructure of the sample together with precipitates can be observed on Fig. 5.5 where STEM BF and HAADF images are shown.

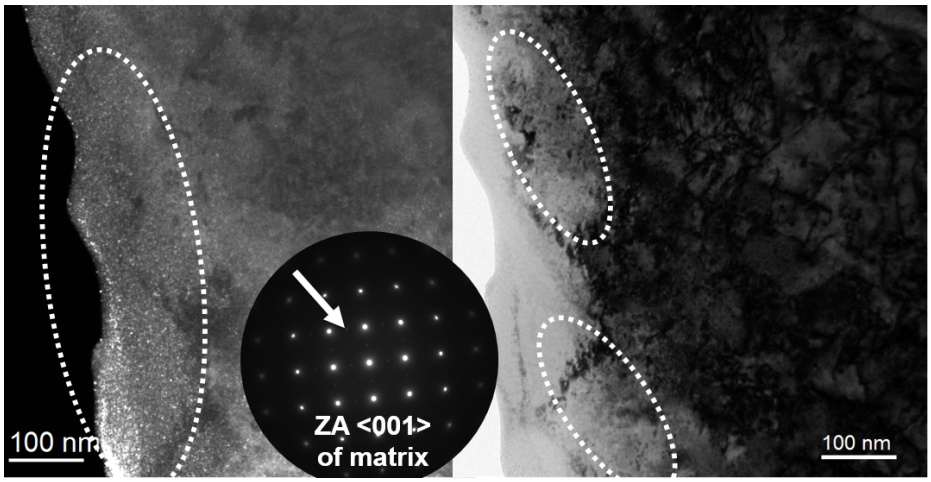

(a) (b)

Figure 5.4: TEM Dark field (a) and bright field (b) images of the stress relaxation sample of $920^o\,C$ quenched just after the determined precipitation start point. The spots where precipitation can be observed are designated with white dashed circles and superlattice reflection is shown by the white arrow.

5.4 Hot Flow Curves

Figure 5.6 shows the curves until ϵ=0.6. In general, the flow curves show strong natural DRX response with single peak behavior except for the 900°C-0.01 s^{-1} test where a continuous gradual increase in the flow stress is observed.

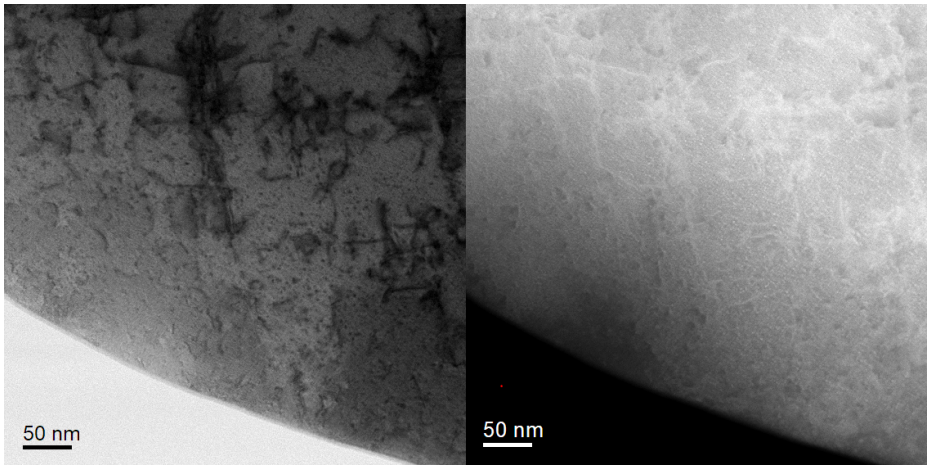

(a) (b)

Figure 5.5: STEM Bright field (a) and high angle annular dark field (b) images of the stress relaxation sample of $920^o\,C$ quenched just after the determined precipitation start point. The diffraction pattern shows the composite lattices clearly with weak superlattice reflections and precipitates can be observed in dark field image as bright spots.

As the DRX nucleation becomes easier at higher temperatures, it is natural to observe a decrease of critical stress for DRX initiation. In addition, because of the increased grain boundary mobility at high temperatures, the kinetics of DRX become faster. Thus, it is expected to see a decrease in peak and steady state stress at higher temperatures. For some cases the steady state region could be observed beyond ϵ=0.65. However, generally, the steady state was not reached until ϵ=0.7. For this reason a special treatment suggested by Quelennec *et al.* [104] is used to correct some material parameters in the following sections.

5.4.1 Material Constants

Apparent Material Constants

The apparent material constants were found according to the relations given by Eqs. 4.40 to 4.43. By taking the logarithm of each side of these and re-ordering as instructed in previous studies [132–134] it can be seen that partial differentiation with respect to temperature makes it possible to retrieve material constants n', β and n. The slope of the

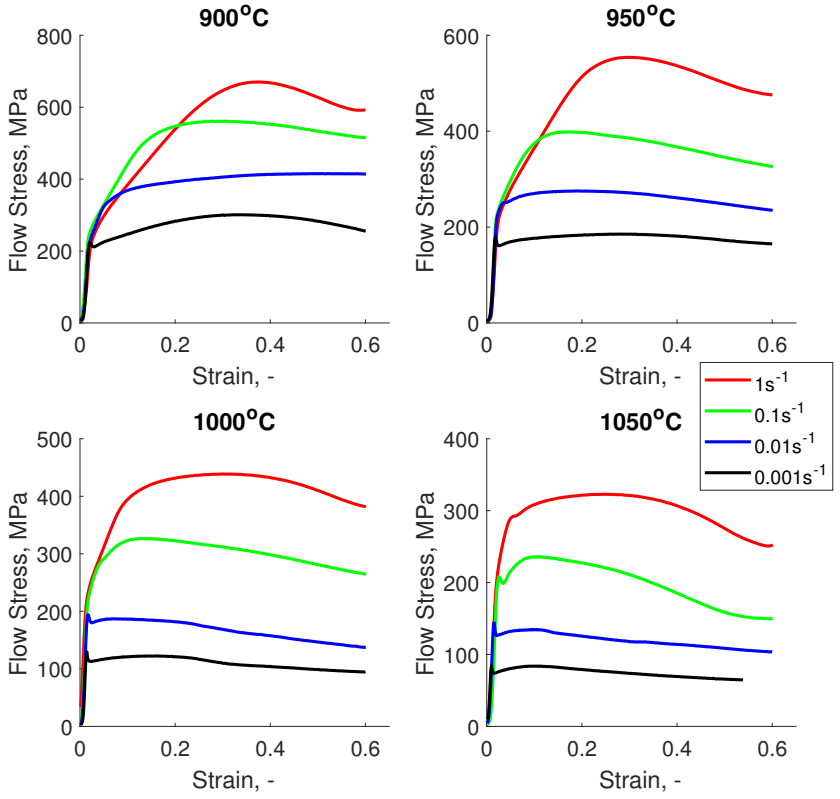

Figure 5.6: Flow curves of Set 1: Hot flow study without prior aging to determine baseline response of the alloy.

plot of $\ln\dot{\epsilon}$ vs $\ln\sigma$ and the slope of the plot of $\ln\dot{\epsilon}$ vs σ can be used to obtain the values of n' and β, respectively. These are shown in Figs. 5.7 (a) and (b). The linear fit of these via least squares method over 4 different temperature range gave an average n' as 6.21 and β as 0.0221. Accordingly α $(=\beta/n')$ was found to be 0.0036. Minimum R^2 observed was 0.956.

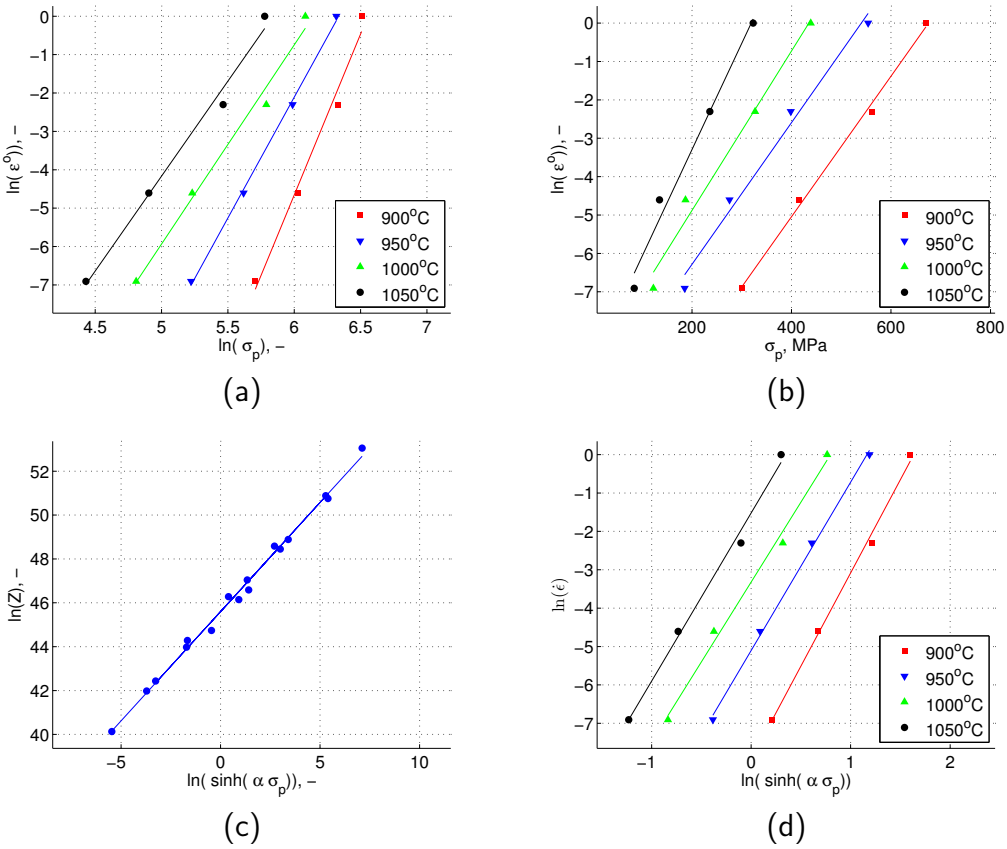

Figure 5.7: Plots that are used to retrieve material constants of apparent approach: (a) n', (b) β, (c) n, (d) A.

Values of n' for temperatures $900°$C, $950°$C, $1000°$C and $1050°$C

are obtained as 8.39, 6.29, 5.18 and 4.95, respectively. Interestingly, an immediate increase of n' is observed when the deformation temperature decreases. If the deformation process is controlled by glide and climb, it is stated that the value n' should be equal to 5 [120], as in the case of $1050°$C and $1000°$C. This increase is expected for $900°$C because the PTT diagram shows that massive precipitation is expected even for exposure times as low as 1 minute. However, according to the TTT diagrams from literature, shown in Fig. 5.8 (a) and (b), at $954°$C the precipitation is not expected before 6 and 12 minutes, respectively. As the slowest test in this study was finished in 11.7 minutes, based on the PTT and TTT diagrams mentioned here, under static conditions precipitation would not be expected for tests conducted in this study. On the other hand, the observed increase of n' at $954°$C could be a sign of dynamic precipitation behavior. A similar behavior is observed by Suave *et al.* [135, 136] for the Ni-base alloy where certain phases are found to be precipitating faster under dynamic conditions. Moreover, Thomas *et al.* [63] reported a similar acceleration in the precipitation behavior of alloy 718 as well as a drift of the transformation lines to higher temperatures.

Furthermore, for the temperatures $950°$C and above, the δ - γ' precipitation sequence is changed and δ starts to form earlier. Therefore, a detailed study of the alloy in this range (i.e. from $950°$C to the δ solvus temperature) could be interesting from the design perspective of the last stages of hot forming processes.

Similar to the treatment for n' and β; n can be calculated from the slope of the plot $ln\dot{\varepsilon}$ vs $ln(sinh(\alpha\sigma_p))$, as shown in Fig. 5.7(c). The average value of n was found as 4.45. After taking the logarithm of both sides and rearranging, the partial differentiation of Eqs. 4.40 to 4.43 with respect to strain rate makes it possible to calculate Q, the activation energy of deformation. The plots used for these calculations are shown in Figs. 5.9(a), (b) & (c) for power, exponential and hyperbolic sine laws respectively.

The linear regression results of power law estimates Q as 535.7 kJ/mol. This value is 541.4 kJ/mol for exponential law and 525.5 kJ/mol

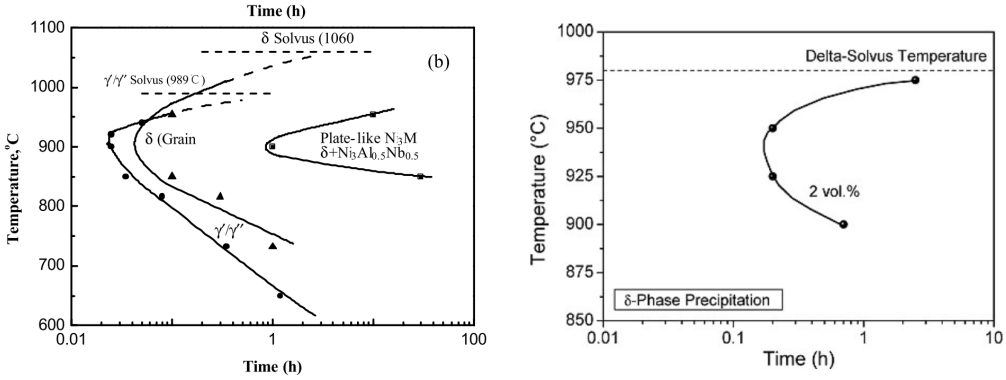

(a) (b)

Figure 5.8: Experimentally determined TTT diagrams of 718Plus, (a) from Xie *et al.* [26] and (b) from Stotter *et al.* [29]. While (a) is showing both γ' and δ, (b) is showing only δ precipitation

for hyperbolic sine laws respectively. The goodness of the fit is the highest for the hyperbolic sine law with R^2=0.978 (for power and exponential law, R^2 is 0.973 and 0.969, respectively). Thus for further calculations Q is selected as 525.5 kJ/mol.

Finally the the Zener-Hollomon parameter, Z and σ_p, can be fit via Eq. 4.43, as shown in Fig. 5.7 (d). The constant A was found to be $3.5797\text{x}10^{20}m^{-2}$.

Material Constants of Physically Based Approach

As one can note, in the Eq. 4.44, there are only two unknowns (B and α') and it is relatively simple to implement this physically based approach.

The $(\dot{\epsilon}/D(T))^{1/5}$ is plotted against $(\alpha'\sigma)/E(T)$ in Fig. 5.10. It is immediately of interest that the $900°$C data behave differently than the rest. The PTT study shows that the kinetics of γ' precipitation is very fast at temperatures around $900°$C-$925°$C, thus the different behavior of observed for $900°$C is indeed an expected result.

Non-linear regression was applied to the available data to fit the Eq. (4.44). Since the hot forming behavior of the alloy at $900°C$ is dramatically different from the rest, two sets of parameters are prepared for further processing. When the precipitation is not expected at deformation temperature (or temperature range) the constants of Eq. (4.44); B and α' are 1300 and 311, respectively. However, when massive precipitation is expected, B should be taken as 340.7 and α' as 617.2.

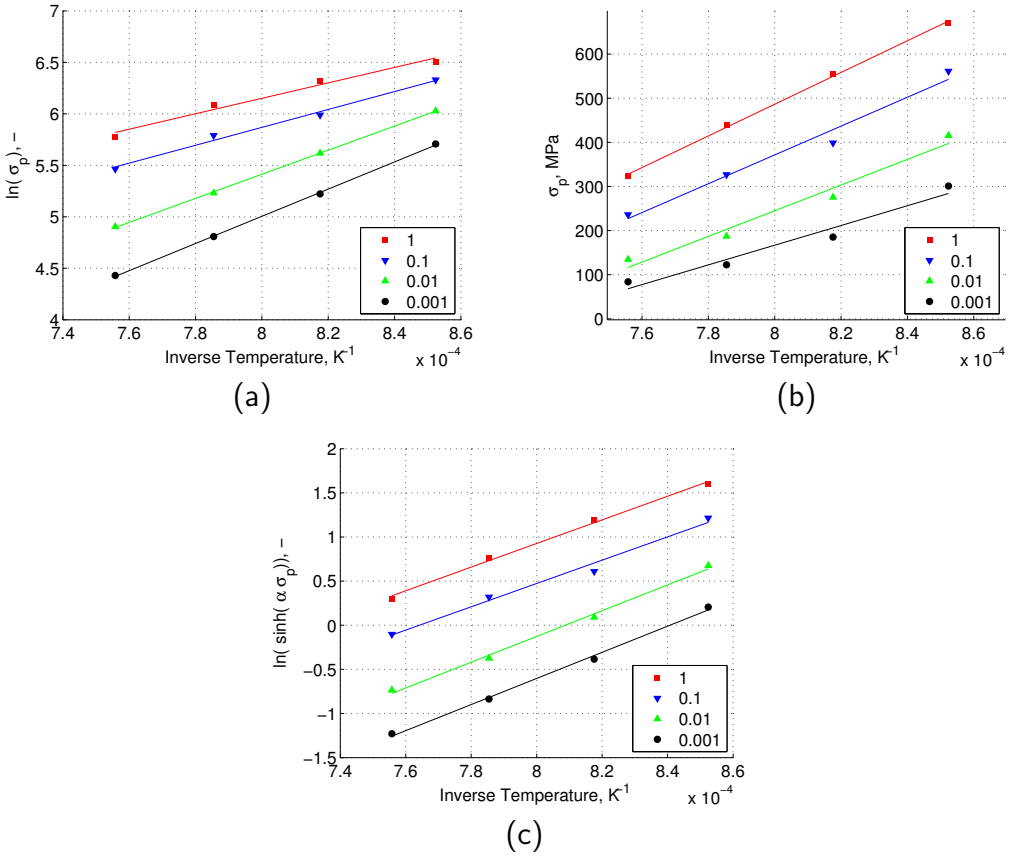

Figure 5.9: Plots used to retrieve activation energy based on power law (a), exponential law (b) and hyperbolic sine law (c)

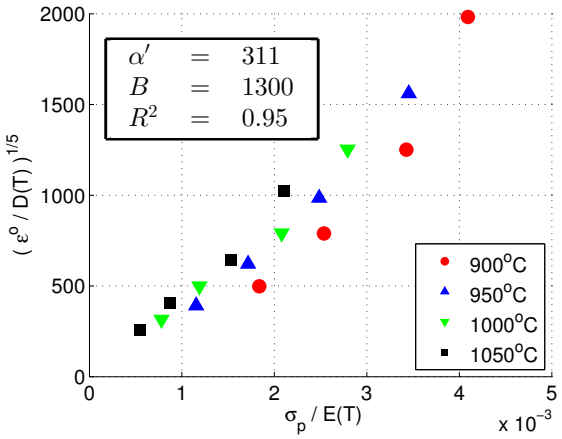

Figure 5.10: Plot used to derive the material constants for physically based approach: α' and B.

Comparison of Apparent and Physically Based Approaches

Figure 5.11 shows a validation plot, where the calculated and measured peak stresses are presented together. In the case of physically based approach, two sets of parameters were suggested based on the precipitation behavior, while in the case of apparent approach, only one set of parameters was suggested as mentioned in the respective section above.

However, for the sake of a good comparison, in Fig. 5.11, only the results of "no precipitation" case from the physically based approach were included. As one can see, both approaches give satisfactory results; yet, it is thought provoking to see that although a massive precipitation process is going on at $900°$C, it is not possible to observe any deviation in the apparent approach even though only one parameter set was used. Maximum difference between predicted and experimental peak stress is 22.2 MPa for the apparent approach. On the other hand, physically based model deviates around 90.4 MPa for $900°$C tests, which underlines the necessity of using two sets of constants (B and α').

Apart from the $900°$C tests, where precipitation is already expected

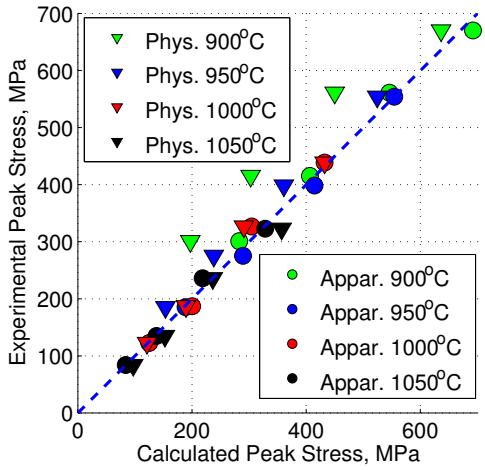

Figure 5.11: A validation plot showing predicted peak stresses by both apparent and physically based approaches versus experimental results.

based on the PTT and TTT results, from Figs. 5.10 and 5.11 one can observe a slight deviation for the 950°C tests as well (blue triangular points in both plots). At 950°C, the average deviation of physically based model is 34 MPa, as observed in Fig. 5.11. Since PTT and TTT diagrams do not foresee any precipitation at 950°C for short holding times, this behavior could be attributed to the acceleration of precipitation process under the deformation conditions covered in this work. This acceleration could be defined as the drift of transformation lines either to shorter times and/or to higher temperatures. As mentioned in "Apparent Material Constants" section, there are some studies which report similar precipitation behavior under dynamic conditions [63, 135, 136].

The overall interpretation of these results suggests that physically based approach is more sensitive to the microstructural changes than the apparent approach. This is in agreement with their natural definition. From Fig. 5.11 it can be seen that apparent approach performs "better"; however, when two set of parameters are used for physically based model, a better fit can be obtained, which is more consistent with

the microstructural evolution of the alloy. To be able to develop more flexible and physical models, having a model which reflects the changes in the microstructure is more important than having a more accurate but less physical model.

5.4.2 Modeling of Hardening Behavior

The terms Ω and U (refer to the Section 4.1.4) were determined for every test condition in Set 1. The section of the stress-strain curves considered for this calculation was until the peak strain. The evolution of these constants as a function of Zener-Hollomon parameter is shown in Fig. 5.12. Under the circumstances where the mean free path of dislocations are constrained by the factors such as GB or second phase particles or dislocation pile-ups, the parameter U should remain constant [137, 138]. However Fig. 5.12 reveals that a certain dependence of U on Z exists.

The linear regression plots in Fig. 5.12 are based on the equations $\Omega = K_\Omega \ Z^{m_\Omega}$ and $(\alpha' b)^2 U = K_U \ Z^{m_U}$. Here the constants of K_Ω and m_Ω are found to be 8020, -0.1155; K_U and m_U are found to be $5.083x10^{-6}$ and 0.1069, respectively. These values are in the same order with those reported in literature, mostly concerning Inconel 718 [63, 139, 140].

Work Hardening Behaviour of Recrystallized Material

In Fig. 5.13, the material constants Ω, Ω' and U are given as a function of Z. This relationship can be defined through $\Omega = K_\Omega \ Z^{m_\Omega}$ and $(\alpha' b)^2 U = K_U \ Z^{m_U}$. Previously this linear relationship was defined regardless the state of the material which is undergoing hardening. The DRV rate parameters given here do not take into account the precipitation effects; however, they do take into account the hardening behavior of recrystallized material, which is not the same as the work hardening of the initial material (Section 4.1.4). Ω' is calculated through the Eqs. (4.31) and (4.32).

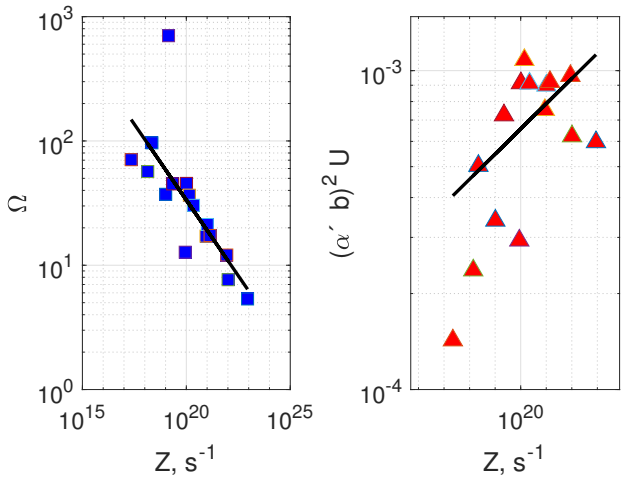

Figure 5.12: Dependence of softening and hardening parameters on the Zener-Hollomon parameter.

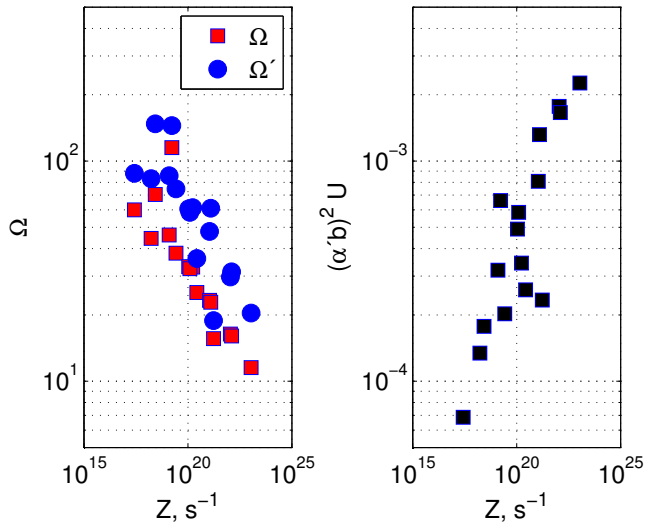

Figure 5.13: Material constants Ω, Ω' and U based on the approach of Quelennec and Jonas (see Section 4.1.4)

5.4.3 Modeling of DRX

As mentioned in Section 4.3.1, Avrami kinetics were implemented to assess the DRX behavior. In Fig. 5.14 one can find the $ln\big(ln(1/(1-X))\big)$ vs. time. Where the time was calculated based on strain via $ln\big((\varepsilon-\varepsilon_p)/\dot{\varepsilon}\big)$.

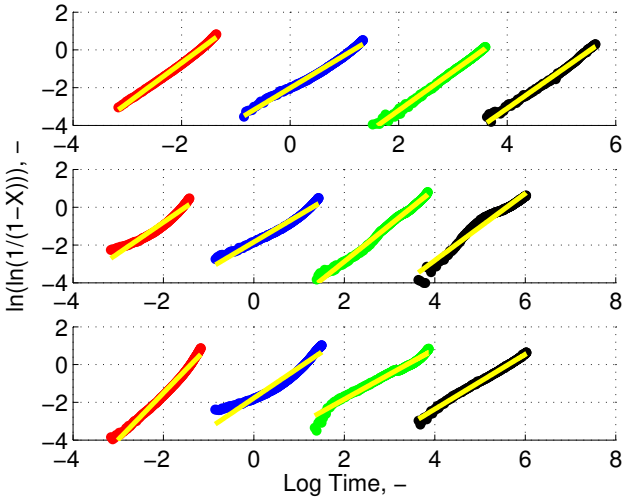

Figure 5.14: Curves used to determine the DRX kinetics: From top to bottom: $950°$C, $1000°$C and $1050°$C.

The k values calculated with the help of Fig. 5.14 are plotted against Zener Hollomon parameter in Fig. 5.15 and do not seem to have a definite dependency on Z. This is indeed a natural behavior as the Avrami model is based on a constant nucleation rate [55, 85]. In the current model the average value of k was found to be 1.798, The value of k can normally have a variation between 1 and 4; however, when this value is constrained between 1 and 2, it is said that the nucleation is mainly occurring on the grain boundaries [55].

Equation (4.51) was used to define the relation between half-time of DRX and strain rate. Accordingly, the activation energy of DRX was found to be 120kJ/mol. Constansts K_t and n_t were retrieved as

$4.491x10^{-6}$ and -0.883, respectively. The order of magnitude of these material constants (k, K_t, n_t), are in agreement with other studies found in literature [141–144].

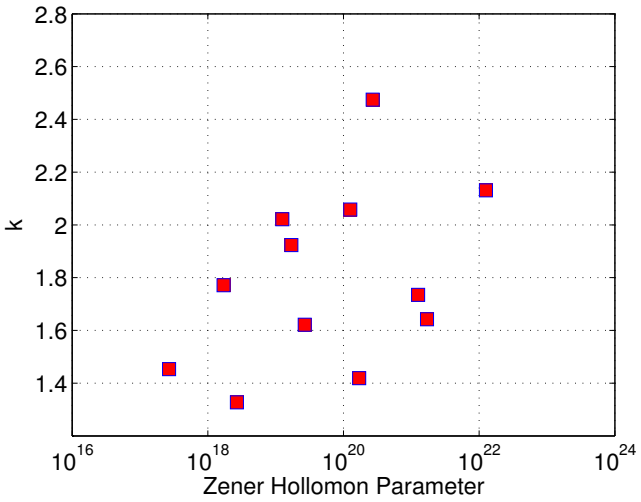

Figure 5.15: Dependence of k of Avrami model on the Zener-Hollomon parameter.

5.4.4 Summary of Initial Analysis of Hot Flow Curves

The initial analysis of the hot flow curves starts with apparent approach to assess the material constants n', β, n, α and A. This is later combined with the physically based approach where material constants B and α' are found. In Section 5.4.1, these two approaches are compared and how they react to the ongoing precipitation behavior is discussed. In order to assess the dynamic precipitation behavior, stress relaxation tests are employed. The relaxation curves are fit to a $\sigma = \sigma_{init} - S''\ ln(1 + \beta t)$ type behavior and deviations from this behavior are considered as precipitation effects. This is later confirmed with microscopy studies. Initial modeling of the hardening section of the flow curves are done

based on the model presented in Section 4.1.4). Accordingly, Ω and U constants are estimated. Finally in order to construct the whole hot flow behavior, one needs to approximate DRX behavior, which is accomplished through Avrami approach where constants K_t and n_t are found and presented.

Chapter 6

Effect of γ' on Hot Flow Behavior of Allvac 718Plus®

In Chapter 5, the hot flow behavior of 718Plus® is investigated through known material models and their derivatives. This investigation is called "baseline" due to the fact that the initial material is free of precipitates.

In this chapter, an attempt to observe, quantify and model the effect of γ' precipitation in the hot flow behavior 718Plus® is presented. The findings of this sub-study may be particularly relevant to the final passes of industrial forging processes.

In this chapter the Set 1 and Set 2 test campaigns will be extensively referred. While detailed explanation of these together with processing routes was given in Section 3.1.2, a brief summary will be beneficial for the reader:

Set 1: *Tests without holding consisting of four different temperature and strain rates, namely;* 900, 950, 1000 *and* $1050^o\,C$, *at strain rates of 0.001, 0.01, 0.1 and* $1s^{-1}$. *Maximum final strain attained is apprx. 0.65.*

Set 2: *Tests with holding prior to the deformation (at* $850^o\,C$ *for a different amounts of time), deformation at* 920, 940, *at a single strain rate of* $0.01s^{-1}$. *Maximum final strain attained is apprx. 0.4.*

6.1 TEM Observations

6.1.1 Overview

Figure 6.1 shows a series of TEM and STEM images of an undeformed sample aged at $850^o\,C$ for 30 minutes. A bright field TEM image giving an overview of the microstructure is given in (a). γ' precipitates accompanied by sparse amount of twins are observed together with stacking faults (SF).

In general, all observed samples point out two different families of γ'. One consisting of fine ($<$10nm) densely distributed population, the other consisting of larger, spherical (faceted) and homogeneously distributed precipitates; different in size depending on the aging time. The appearance of two different γ' population is found to be more pronounced for samples in Set 2 (deformed after pre-aging). This is in line with the findings of Whitmore et al. [31] where the authors analyzed single and double aged 718Plus and reported both treatment routines result in a very fine (1-2 nm) γ' as a secondary precipitate population. The smaller γ' size for their case is expected as the aging temperature was below $790^o\,C$ for Whitmore *et al.* [31].

These γ' particles can be observed both in Fig. 6.1-b1 & b2 and 6.1-c. The former pair represents bright field (BF) TEM images and corresponding dark field (DF) TEM image recorded using (100) superlattice reflection. The latter is bright field and High Angle Annular Dark Field (HAADF) STEM images recorded in a region where γ' is observed accompanied with planar defects which might be twins, SF or Anti-Phase boundary (APB).

As mentioned in the experimental section, Set 2 samples were deformed up to near critical strain after different aging treatments. Bright field and corresponding dark field TEM images using (001) superlattice reflection from two different regions of the $920^o\,C$-$20'$ sample are shown in Fig. 6.2.

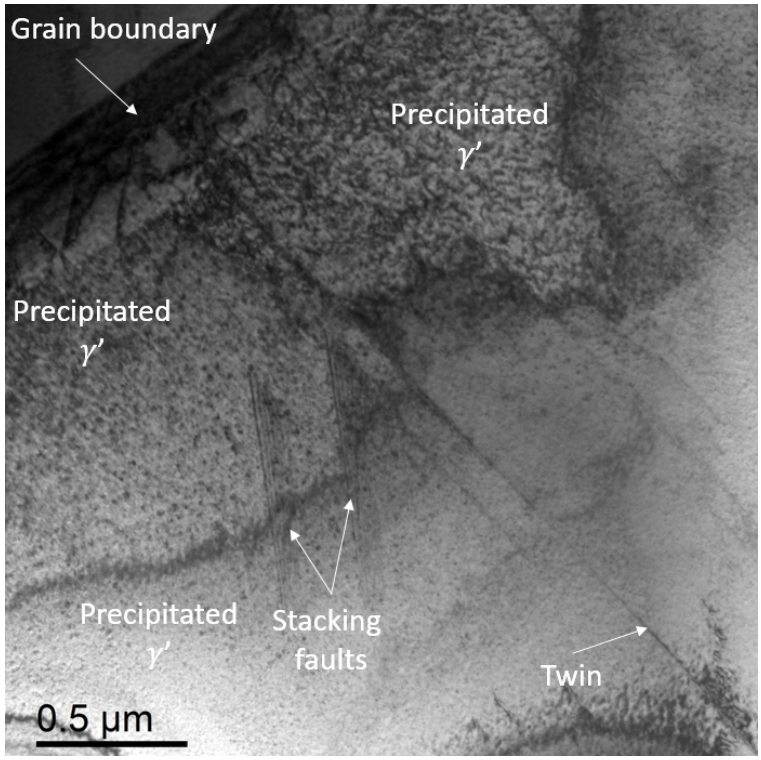

(a)

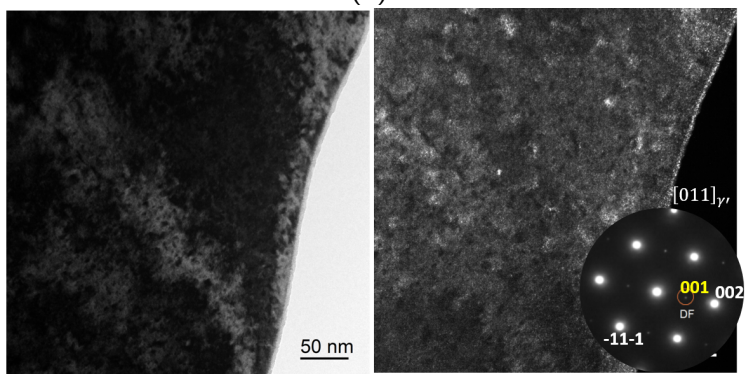

(b1) (b2)

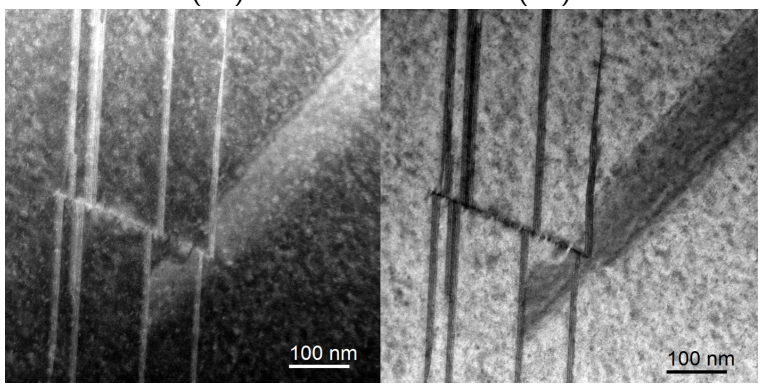

(c1) (c2)

Figure 6.1: TEM images after solutionizing at $1050^o\,C$ followed by 30 minutes aging at $850^o\,C$: (a) Low magnification image giving an overview of the microstructure, (b1) Bright field and (b2) corresponding dark field images recorded along [011]γ // [011]γ' zone axis. STEM images, (c1) High Angle Annular Dark Field image and (c2) its bright field image.

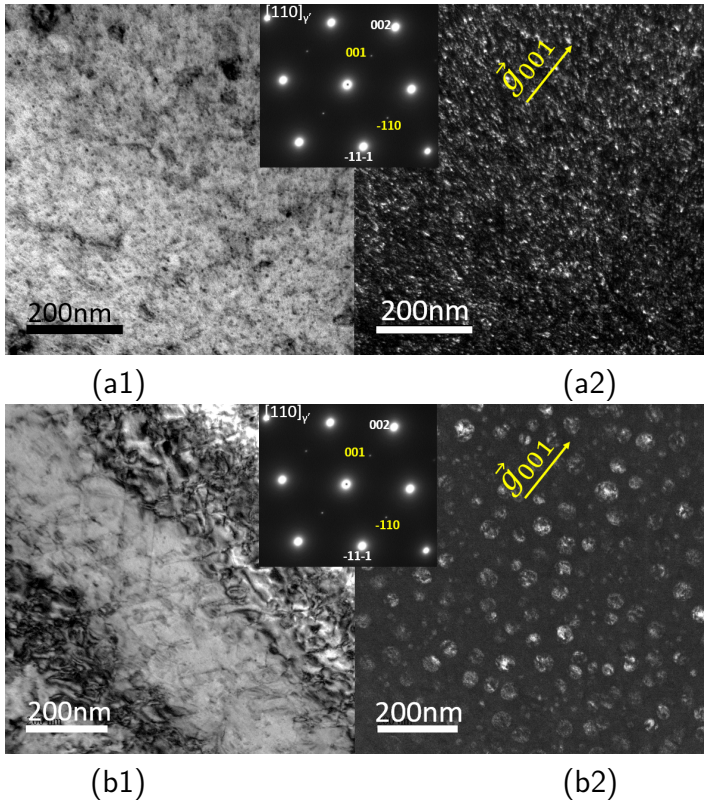

Figure 6.2: TEM bright field (a1 & b1) and corresponding dark field (a2 & b2) images of (a) aged ($850^o\,C$ for 20 mintues) and (b) deformed ($920^o\,C$, $0.01\,s^{-1}$) sample. Both dark field images were recorded using (001) weak superlattice reflection.

These images are recorded on the same grain. While Fig. 6.2-a2 shows fine and densely distributed γ', Fig. 6.2-b2 shows spherical particles having average size of 39.8 nm. Even though most of the observed regions have the latter form of spherical γ' (see also Fig. 6.3 for EDX maps, it is thought-provoking that there are regions within the same grain where a finer and denser γ' population is observed. This inhomogeneity can be either associated with that of the deformation or due

to a zone depleted of γ' forming elements. As highlighted by Militzer *et al.* [145], vacancy concentration levels during hot deformation might attain as much as 40 times that of equilibrium concentrations for a given temperature. Thus, any inhomogeneity in the dislocation density within a grain might cause local variations in precipitation characteristics. For the calculations performed within this study, only the spherical γ' population is considered to have an effect on the dislocation path.

Figure 6.3 gives the elemental maps (EDX maps) recorded on samples $920^o\,C$-$20'$ (a) and $940^o\,C$-$30'$ (b). γ' can be associated with the Cr depleted and Al/Ti rich zones. Only Cr, Al and Ti elements are presented to highlight the contrast. As mentioned in the experimental section, 920 and $940^o\,C$ are the temperatures at which the nose and asymptote of γ-γ' transformation line is located on the TTT diagram, respectively. Based on Fig. 6.3-b, the γ' obtained during pre-aging treatment is preserved to a large extent during deformation at $940^o\,C$. In contrast, γ' observed in $920^o\,C$-$20'$ is much well defined, indicating a contribution of deformation to γ' growth when the deformation takes place in the precipitation window (below $940^o\,C$). The effect of deformation on the nucleation of γ' might be considered based on Fig. 6.2-a2; however, further examination would be necessary. Furthermore, considering the overall volume fraction of γ' before deformation, forced nucleation of γ' is of low probability.

6.1.2 Deformation

One of the objectives of TEM characterization in this study is to understand which dislocation-particle interaction mechanism(s) is active. This is particularly important when evaluating the effect of aging on the integrated/overall mechanical response of the alloy.

To this end, the weak-beam technique has been used. Based on the observations, dislocation bowing and looping can be clearly observed, while cutting cannot be ruled out. Figure 6.4 shows a set of bright field images obtained from sample $920^o\,C$-$20'$. While Fig. 6.4-a gives an overview, the upper arrow on the image given in Fig. 6.4-b2 shows a

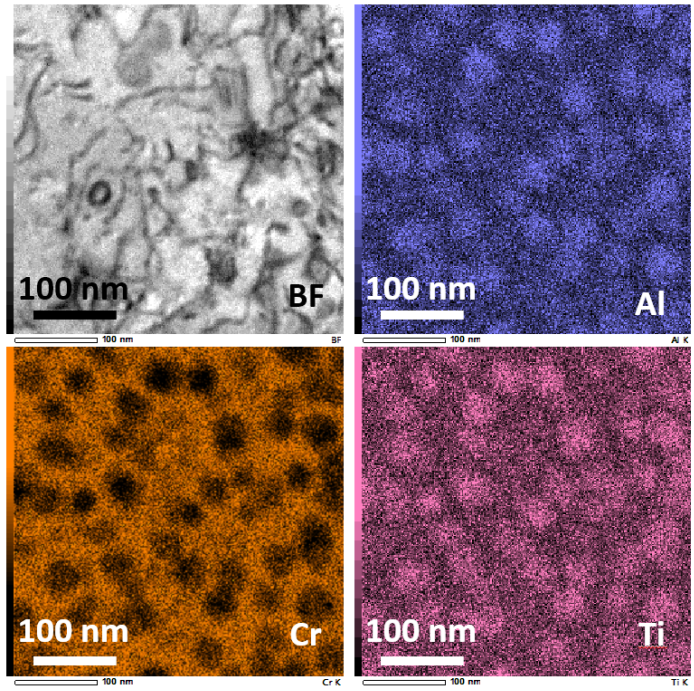

(a)

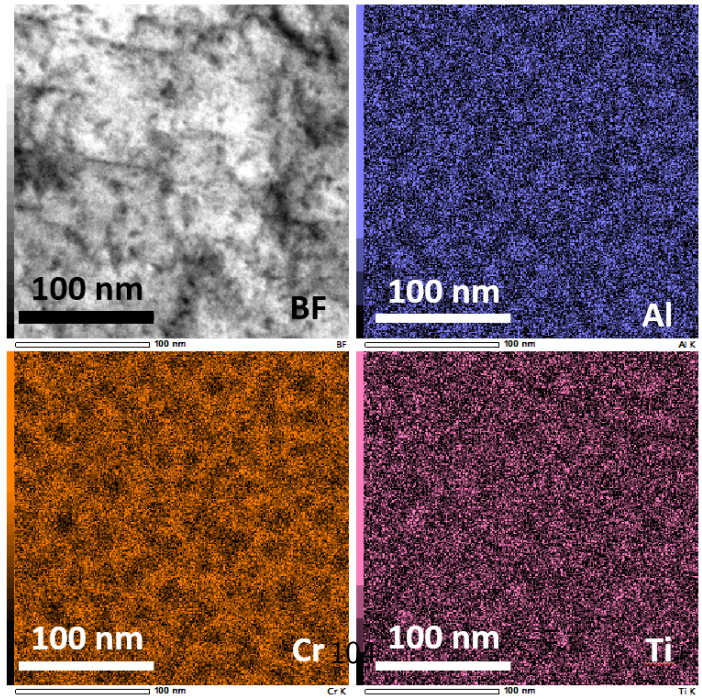

(b)

Figure 6.3: EDX maps of aged and deformed samples: (a) $920^o\,C$-$20'$, (b) $940^o\,C$-$30'$

dislocation bowing around a precipitate and the lower one shows a dislocation cutting a precipitate (the dashed line given is $[1\overline{12}]$). This result is interesting because Zickler et al. [114] reported the experimental and predicted room temperature yield strength of 718Plus for aging times up to 200 minutes at $825^o\,C$. These authors highlight that the predictions based on Orowan mechanism overestimate the experimental values more than 1.5 times for all aging times. In their work they conclude that Orowan mechanism becomes active only after 50 minutes of aging time at $825^o\,C$. Compared to this, in the current case while 20 minutes pre-aging time is rather short, traces of Orowan mechanism can be clearly observed.

Furthermore, Fig. 6.5 shows bright field and weak beam dark field images of $920^o\,C$-$20'$ sample. In the DF images Fig. 6.5-a2&b2 some characteristic fringes (a zoomed image is also given on the inset of Fig. 6.5-a2) are clearly visible. There may be many reasons causing the formation of these fringes. They could be attributed to Moiré, to stacking fault bounded by partial dissociations, Shockley dislocations resulting from perfect dislocation dissociation, etc. The fringes could appear during the shearing of precipitates by the matrix dislocations, recalling the Condat-Decamps mechanism [146, 147].

It is well established [148] that the stacking fault alternate parallel bright and dark fringes, the outer of which does not have the same contrast, when the image is recorded in dark field mode, the image is called asymmetric. The insert in dark field image of Fig. 6.5-a2 point out a series of alternate bright and dark fringes, the outer fringes have the same bright contrast. Based on this behavior, the stacking fault are excluded, thus we are left with the Moiré fringes. In the current case, the inter-fringes as well as the misorientation between the orthogonal direction to the fringes and the reflections (001) of the γ' (or the γ-matrix). A slight disorientation of less than 1 degree was detected. This configuration strongly argues in favor of mixed Moiré fringes (translation + rotation) obtained by the superposition of the matrix and precipitates. The departure to the exact cube-cube relationship should be attributed to stress relaxation during the shearing of the precipitates by the matrix

dislocations.

Additionally, a bright field TEM image of $940^o\,C$-$0'$ sample (sample with no prior aging) is shown in Fig. 6.6, presenting abundant a/2<110> matrix dislocations with evidence of cross slip (note the rigged appearance of the dislocations). This is an interesting detail as no significant precipitation is observed in this sample. Under normal circumstances, an increase in cross-slip probability, thus an increase in recovery parameter Ω, would be expected in an aged alloy relative to the solutionized one. Based on this in the current case, Ω is assumed to be independent of precipitation.

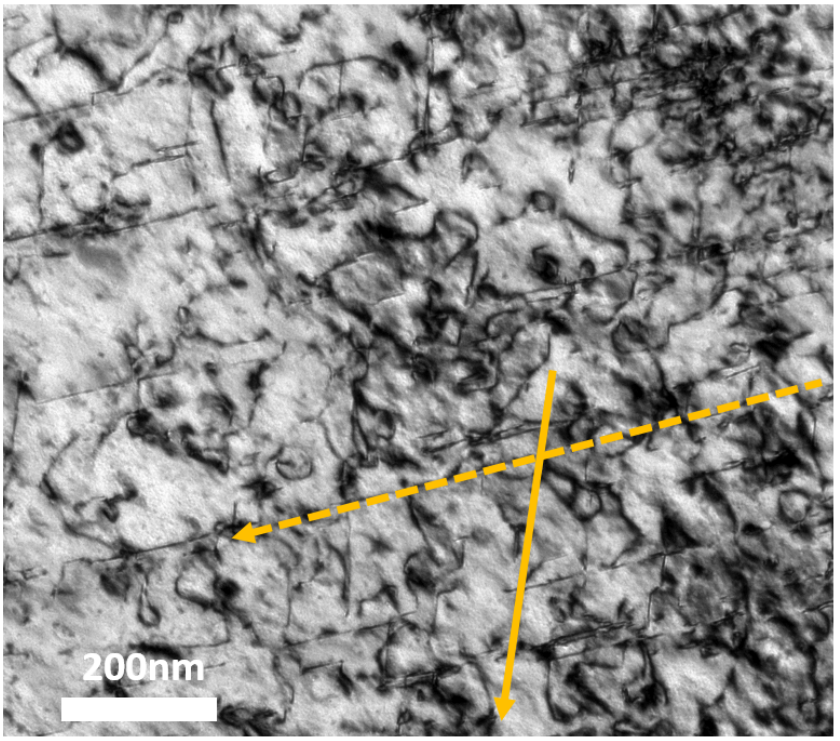

(a)

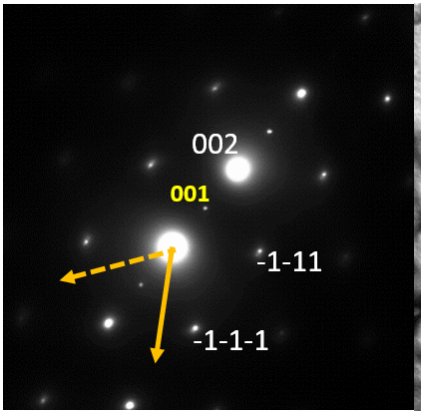

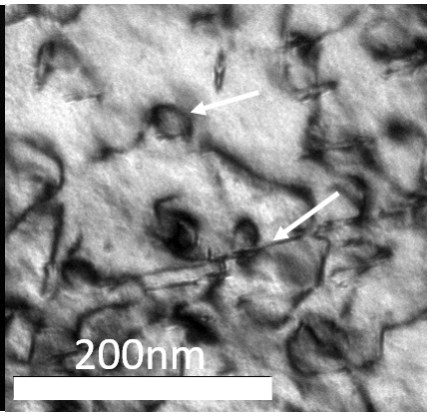

(b1) (b2)

Figure 6.4: (a) Bright field TEM image with approximate zone axis [011]. (b2) A close up view of a portion of the image shown on (a). (b1) is the recorded diffraction pattern of the image (b2).

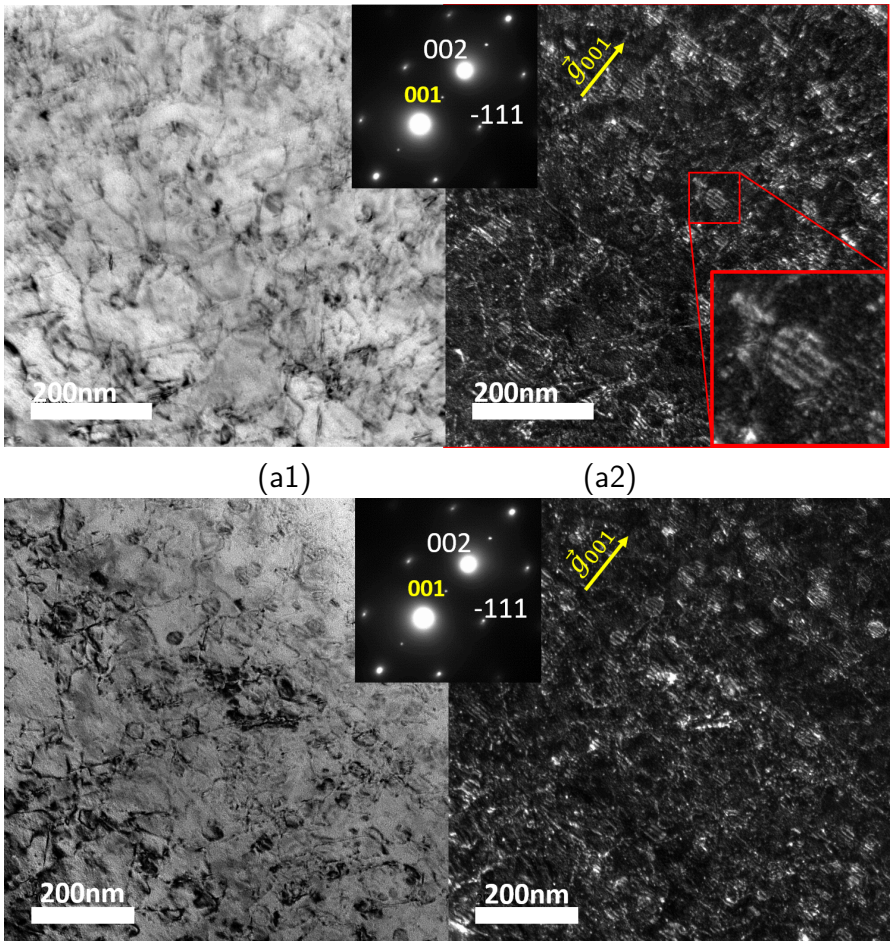

Figure 6.5: Bright field (a1 & b1) and weak beam dark field (a2 & b2) TEM images of 920^o C-$20'$ sample after deformation. Weak beam image (g-3g) g=001 recorded along zone axis close to [011].

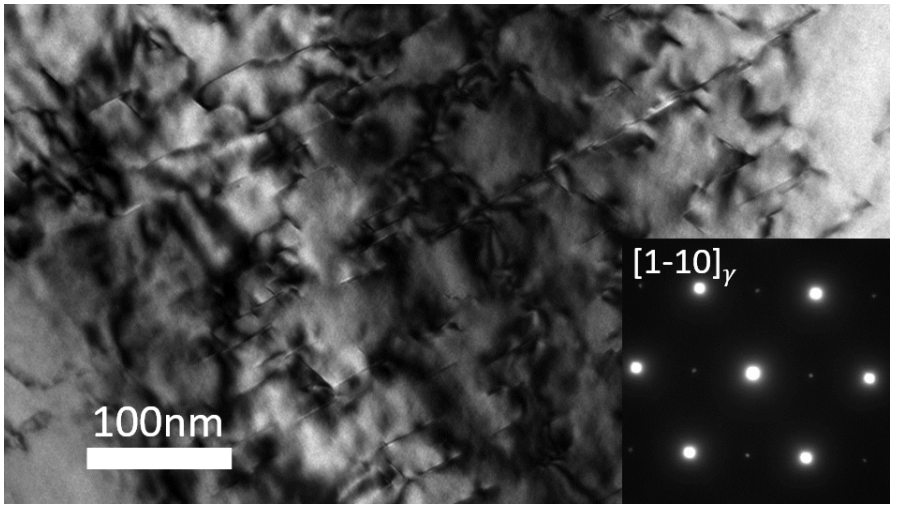

Figure 6.6: Bright field TEM image of $940^o\,C$-0′ sample. (a/2)$< 110 >$ type of matrix dislocations.

6.1.3 Morphology of γ', its Relationship with γ Matrix and Symmetry Analysis

The γ' precipitates adopt an usual cube-on-cube orientation relationship with the matrix where it develops as derived from the analyzed SAED diffraction patterns. This relationship can be expressed by the parallelism between the corresponding planes and can be expressed as follows:

$$(002)_\gamma \;//\; (001)_{\gamma'}$$
$$(1\bar{1}1)_\gamma \;//\; (1\bar{1}1)_{\gamma'}$$
$$(2\bar{2}0)_\gamma \;//\; (1\bar{1}0)_{\gamma'}$$

Trace analysis indicates that the γ' phase develops only one variant in each matrix grain (see Fig. 6.2-b2 as well). Figure 6.7 shows a high resolution image of a 30 minutes aged sample at $850^o\,C$ after solutionizing at $1050^o\,C$. The inset is the corresponding FFT recorded along [011] $_\gamma$ // [011] $_{\gamma'}$.

It is well established, through the group theory, that the morphology of phases, taking place in any medium (solid, liquid or gas) is of great importance in materials science. Understanding of both the equilibrium shape and the habit plane adopted by these phases in their medium is widely investigated [149–156]. This group theory will be applied here, based on the symmetry analysis, to explain the shape developed by the γ' phase and its variant number.

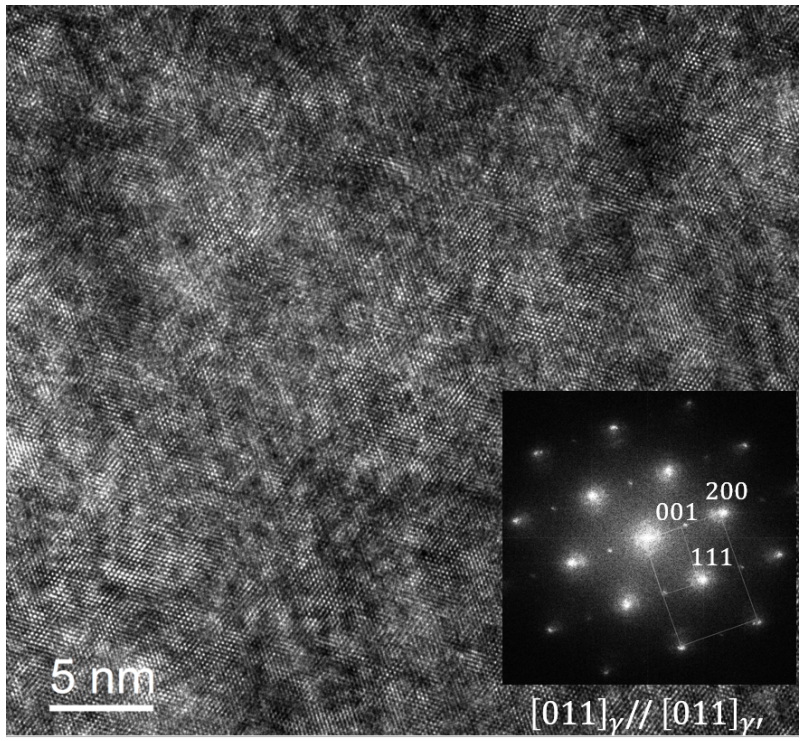

Figure 6.7: High Resolution TEM (HRTEM) image and its corresponding FFT recorded along $[011]_{\gamma}$ // $[011]_{\gamma'}$ zone axis.

When the point symmetry groups of γ matrix and γ' precipitates are considered (G^{γ} and $G^{\gamma'}$), if the precipitating phase adopts an orientation relationship with the matrix, the intersection point group (H) will be represented by their common symmetry elements. Usually denoted as

$H = G^{\gamma} \cap G^{\gamma'}$. H, the subgroup of the matrix and of the precipitate point groups the morphology of the precipitate together with the variant number n of the subgroupings. The latter helps to assess the number of variant(s) taking place in the matrix and satisfying the orientation relationship adopted between the matrix and the precipitate. The variant number n is the ratio $n = m/h$ where m and h are the orders G^{γ} and H, respectively. This analysis is summarized in Table 6.1. Accordingly, the point group of the matrix (G^{γ}) is $\frac{4}{m}\,\overline{3}\,\frac{2}{m}$ which is the same as that of the γ' ($G^{\gamma'}$). Obeying to the orientation relationship, the superimposition of the symmetry elements of the two $\frac{4}{m}\,\overline{3}\,\frac{2}{m}$ point groups preserve all symmetry elements leading to $H = \frac{4}{m}\,\overline{3}\,\frac{2}{m}$.

The fact that both G^{γ} and $G^{\gamma'}$ having the order of 48 leads to the variant number $n = 1$, indicating that there is only one variant of the γ' formation in γ matrix. This is in line with the observations, i.e., faceted spherical and cubic γ' in γ depending on the volume fraction. In the case of 718Plus, we observe mostly fine or faceted spherical precipitates, see Figs. 6.2-b2 and EDX maps in Fig. 6.3-a.

Table 6.1: Determination of H, the intersection point group, the elements of which are common to the point groups of γ and γ' phases. n is the number of variants; m, p and h are the orders of the point groups of matrix, precipitate and intersection group respectively.

Orientation Relationship	Superimposed symmetry elements	Shared symmetry elements	$H = G^{\gamma} \cap G^{\gamma'}$ with $n = \frac{m}{h}$
$(002)_{\gamma}$ // $(001)_{\gamma'}$	$\frac{4}{m} \parallel \frac{4}{m}$	$\frac{4}{m}$	
$(1\bar{1}1)_{\gamma}$ // $(1\bar{1}1)_{\gamma'}$	$\overline{3} \parallel \overline{3}$	$\overline{3}$	$\frac{4}{m}\overline{3}\frac{2}{m}$
$(2\bar{2}0)_{\gamma}$ // $(1\bar{1}0)_{\gamma'}$	$\frac{2}{m} \parallel \frac{2}{m}$	$\frac{2}{m}$	with $n = 48/48 = 1$

6.2 Set 2 Results: Tests with Holding Prior to the Deformation

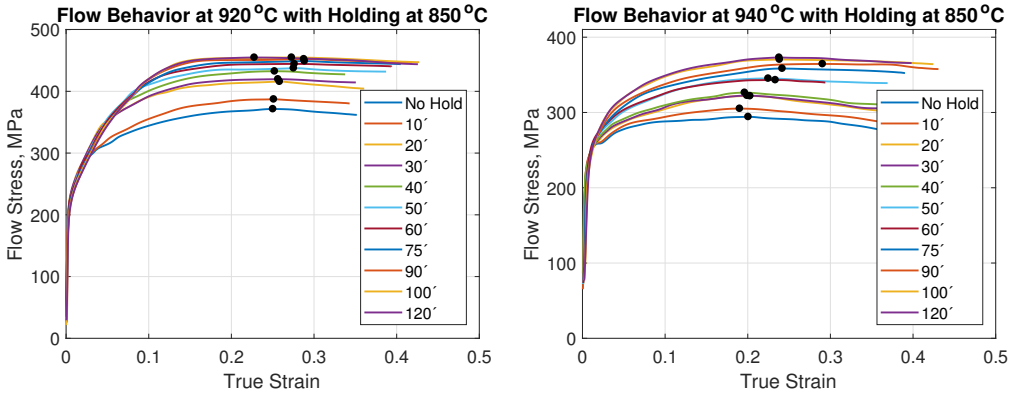

Figure 6.8: Hot flow response of different samples aged at $850^o\,C$ for different times. Left: $920^o\,C$, $0.01\,s^{-1}$; Right: $940^o\,C$, $0.01\,s^{-1}$.

As mentioned earlier, in a part of this work an attempt has been made to follow the effects of γ' particles on the high temperature flow behavior, quantify this effect and propose an appropriate model to mimic this effect. Flow curves of Set 2 tests are presented in Fig. 6.8.

A few details can be noted immediately by observing these flow curves. Firstly, a convergence in the flow behavior with longer aging times observed after almost two hours of aging. Secondly, some curves ($920^o\,C$-0′, $940^o\,C$-0′ and $940^o\,C$-10′) present a double yield at the very initial stages of deformation. This is observed in some of the flow curves of Set 1 as well (see Section 5.4).

The effect of aging seems to manifest itself on the flow curve as if there was an increase of the Zener-Hollomon parameter. This is accompanied by the vanishing of the aforementioned double yield and a slight change in the slope of the curves in the elastic section. The slope change and the "double yielding" behavior was also observed by Wen et al. [157] who compared the work hardening behavior of a Ni-base superalloy in

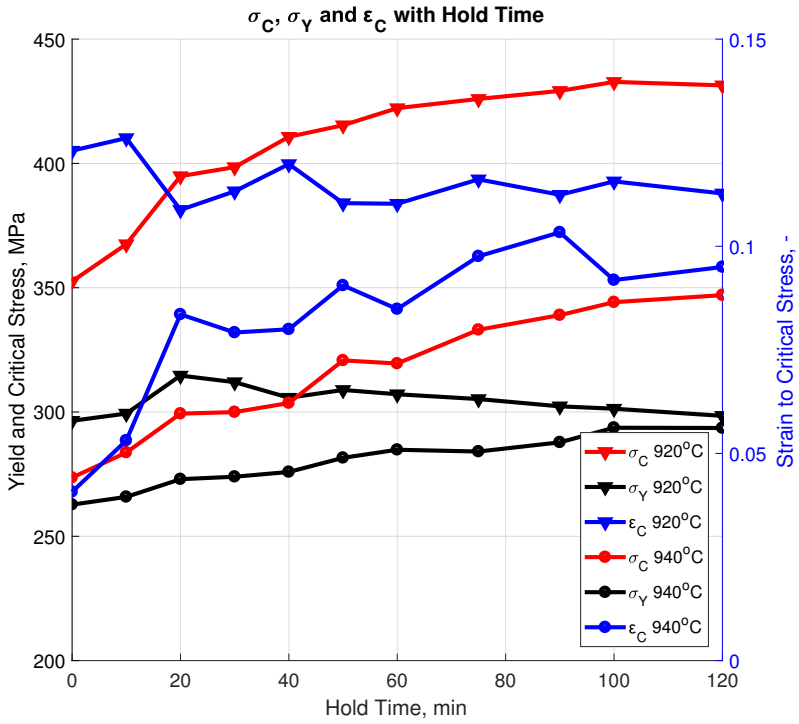

Figure 6.9: Strain to critical stress, critical stress and yield strength; plotted as a function of aging time.

the solutionized and aged state. This might be related to the diffusion of the γ' forming elements and deformation speed. However, this is out of the scope of the current investigation.

In 1979, Jonas and Weiss [87] presented a report, stating that the consideration of yield strength to observe the effect of precipitation and/or to estimate the precipitation kinetics is not the optimum method due to its insensitivity / oversensitivity. In the current case, yield strength against the aging time is presented; however, they are not used in any quantitative/numerical evaluation. Furthermore, these authors [87] found that strain to peak stress is a more reliable parameter to track the

effects of precipitation. The evolution of critical stress, yield strength and strain to critical stress is given in Fig. 6.9. The critical above analysis is found based on the formulation of Najafizadeh and Jonas [158].

Conversely to the findings of Jonas and Weiss [87], here the strain to critical stress does not decrease to converge a value. The decrease of the critical strain in their case (earlier start of DRX) is explained by the lack of dynamic precipitation. When the sample is held before deformation, as the static precipitation evolves, the matrix remains depleted of precipitate forming elements, thus reducing the potential of dynamic precipitation.

In the current investigation, the opposite is observed, i.e. longer aging times result in delays in the critical strain. While this is not the core point of the current work, this might a result of a combination of few facts. First, the precipitating phases in Nb microalloyed steels (Nb(C, N)) and superalloys are different in nature when their relationship with the matrix is considered. The coherency/semi-coherency for the precipitates in microalloyed steels is usually lost for precipitate sizes larger than $10\,nm$ [159]. Thus, with aging, precipitates formed prior to the deformation might not contribute the retardation of DRX as efficiently as the dynamically precipitating ones. Secondly, probably as Andersson et al. and Srinivasan et al. [89,160] reported, after solutionizing at relatively higher temperatures (above $1012^o\,C$) the subsequent δ/η precipitation becomes very sluggish (due to the growth of the original grains). This makes the microstructure starve the preferential DRX nucleation sites. Due to the absence of GB precipitates, the effect of γ' on DRX onset potentially become more pronounced. However, further investigation would be necessary to clarify this.

6.3 Including the Effect of γ' upon Modeling the DRV Behavior

In Section 4.1.5 a model is proposed to include the γ' effects. In this section, the results of this model are presented when applied to the current case. As mentioned previously, to employ a precipitation model

such as the one given in this work, one needs a description of the volume fraction and particle size of the precipitates. These can be obtained through numerical models for precipitation or based on experimental data. The radius data presented by Radis and Zickler *et al.* [113, 114] considering static precipitation are found to under-estimate the second particle radius when compared to the current findings below $940^o\,C$. Thus, the models that these authors presented are calibrated according to γ' radius observed in the deformed samples in this study. Accordingly, the volume fraction and precipitate radius values are summarized on Table 6.2.

Table 6.2: Calibration of γ' volume fraction and radius evolution of 718Plus with deformation time t

Temperature	Vol. Fraction	Radius
$< 940°$C	0.091	$3.1843\ t^{1/3}$
$> 940°$C	0.091	$2.9143\ t^{1/3}$

The resulting parameters of the model are summarized in Table 6.3. A comparison of measured and computed stress-strain curves for 0, 30 and 120 minutes of aging are shown in Fig. 6.10. The resultant mean error over the strain interval averaged through all conditions is $11.37\,MPa$, which is acceptable considering the modifications made to the base models. Although the deformation is assumed to be homogeneous, to account for the effect of precipitation, it was necessary to introduce more model parameters. While the number of parameters is quite high relative to the simplistic models, the model is still applicable. To simplify the treatment, the factor C can be accepted as a constant when the deformation duration is short relative to precipitation kinetics. Plausible values for this factor are given in Table 6.3.

Table 6.3: Model parameters and results.

Parameter	$920^o\,C - 0.01s^{-1}$	$940^o\,C - 0.01s^{-1}$	Unit
α	0.15	0.15	-
b	$2.56x10^{-10}$	$2.56x10^{-10}$	meters
m	3.1	3.1	-
C (when constant)	0.11	0.08	-
Ω	33.82	37.35	-
U	$8.020x10^{-4}$	$7.318x10^{-4}$	-
ρ_0	$1x10^{12}$	$1x10^{12}$	m/m^3
K_{prec} (no hold)	0	0	-
μ	Eq. (4.47)	Eq. (4.47)	GPa
w_q	0.75	0.75	-
w_r	0.82	0.82	-
γ_{APB}	0.111	0.111	J/m^2
β	0.29	0.31	-
k_c	0.08	0.09	-

To evaluate how f_{cut} evolves with aging time, the contribution of second phase particles is considered through Eq. 4.37 and 4.38 based on the change in σ_p of Eq. 4.33. This is summarized in Fig. 6.11. When calculating the contribution of yield stress at room temperature, the critical radius/aging time can be found by equating the Eqs. 4.37 and 4.38. When this is applied to the current case, one finds the critical aging time

to be 4000 seconds (taking $\beta = 1$ and $k_c = 1$). However, this would not correlate with the findings of the TEM study (recall Fig 6.4 where after 1200 seconds of aging it is possible to see bowing). After calibrating Eqs. 4.37 and 4.38 and using the Eq. 4.39 one finds that about 1200-1800 seconds of aging Orowan mechanism is active. The critical radius for similar alloys is reported to be around 12 nm [161, 162] which is in line with the current findings. However, the very same alloy was previously studied by Zickler *et al.* [11] for room temperature yield strength predictions and they reported particle shearing as the main mechanism governing the precipitation contribution. This raises the question whether high temperature deformation favors Orowan mechanism or not. Furthermore, the validity of the equations Eq. 4.37 and 4.38 to evaluate the particle strengthening at high temperatures can be questioned. From a physics based modeling, there should not be any calibration constants associated with contributions independent of strain.

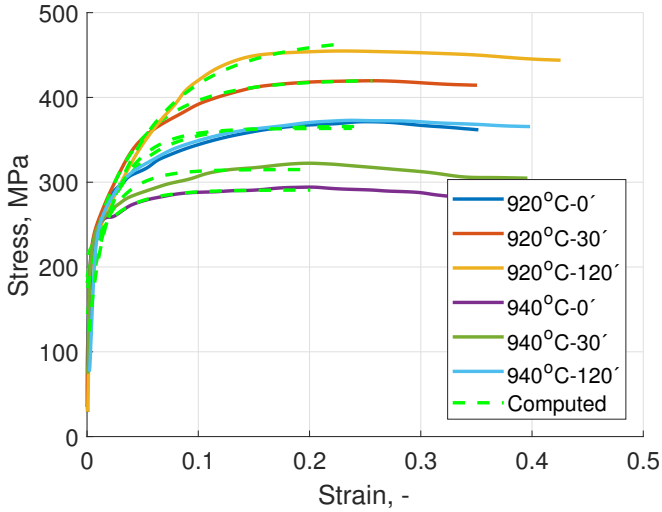

Figure 6.10: Measured and calculated flow curves based on model given in Section 4.1.5. Solutionized and aged specimens for 30 and 120 mins. are given.

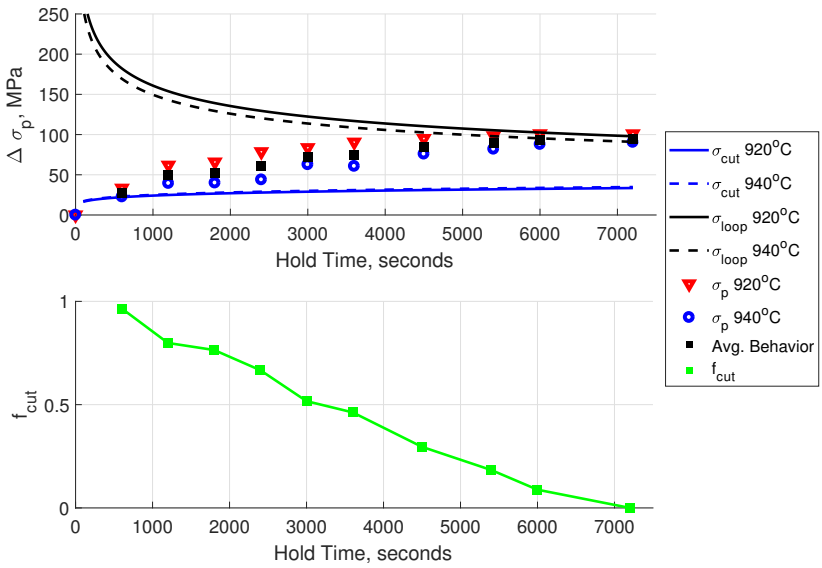

Figure 6.11: Increase in σ_p at 920 and $940^o\,C$ as a function of aging time. Breakdown of the calculated increase in σ_p (based on Eq. (4.33)) due to different contributing mechanisms (i.e. σ_{cut} and σ_{loop}) are given (continuous and dashed lines). Finally, activity of the cutting mechanism (f_{cut}) is presented as a function of aging time.

Chapter 7

Summary and Conclusions

7.1 Summary

The present work aims to contribute to a better understanding of the processes that are taking place during high temperature deformation on the alloy ALLVAC 718Plus®. Special emphasis was placed on the γ' precipitation during the course of deformation and the effect of this phenomenon on the deformation behavior of the alloy.

The results of compression tests which have been conducted within the temperature range of 900 - $1050^o\,C$ at strain rates of 1, 0.1, 0.01, 0.001 s^{-1} are used to understand the basic hot flow behavior of the alloy. Furthermore, stress relaxation tests in the range of 900 - $980^o\,C$ are employed to track the dynamic precipitation of γ'. Series of compression tests of pre-aged specimens with short hold times have been performed to understand the effect of this primary hardening phase (γ') on the deformation behavior of the alloy.

In Chapter 4, the 'weighted average approach' of modeling the whole flow curve is presented, which uses σ_{wh}, σ_{RX} and X_{RX} as inputs to represent the flow behavior in a wide range of strains. Moreover, various dislocation density based hardening models have been summarized to represent σ_{RX} in order to give a background as to how these models have been evolving. Extensions of these models (or derivaties) have been

proposed or adapted in order to obtain more physically based representations of phenomena taking place during hot deformation. These models have been applied to the selected material. Based on these it can be concluded that:

(1) When deformed at temperatures and strain rates which correspond to lower Zener-Hollomon parameters, 718Plus undergoes dynamic recrystallization. Regarding the baseline (precipitate-free initial microstructure) deformation behavior of this alloy, after the application of well known *Kinetic Equations*, a set of apparent material constants for hyperbolic sine model and two sets of material constants for physically based approach were reported (see Section 5.4.1). The apparent approach, produces a maximum 22.2 MPa difference between predicted and experimental peak stress. This value is lower for physically based approach with two sets of parameters. The comparison between the apparent approach and the physically based approach showed that one can detect the existence of precipitating particles via the latter more easily. Moreover, it is possible to say that the deformation process is controlled by dislocation glide and climb as long as there is no precipitation and deformation process is controlled by the self-diffusion of Nickel.

(2) The results obtained at $950^o\,C$ via the physically based approach might be a sign of an accelerated precipitation behavior due to the dynamic state of the material. Although individual n' values for different temperatures showed a variation in the apparent model, it did not show sensitivity over precipitation when the peak stress is calculated. However, the calculated stress values agreed well with the experimental data.

(3) The original Estrin-Mecking and Bergstrom model and Avrami formalism successfully describe the flow curve prior to the peak stress and DRX kinetics, respectively. Necessary material constants have been reported in Sections 5.4.2 and 5.4.3.

(4) Since the steady stress was not reached in some of the compression tests, the conventional steady stress definition was later omitted in the extended models, and instead of this, critical stress was used instead to calculate the σ_{RX}. This was found to be a better approach when compression tests are employed to extract material parameters.

(5) In a part of this work, an attempt to track the precipitation kinetics through stress relaxation tests has been made. However, with 10% pre-straining, precipitation did not manifest itself on the relaxation curves as strong as it is reported in the literature. It was concluded that it is impossible to track precipitation kinetics easily through stress relaxation tests. However, if rather than visual inspection, a fitting function of type $\sigma = \sigma_{init} - S'' \; ln(1 + \beta t)$ is used, deflection points of the relaxation curves from the fitted function can be accepted as precipitation initiation points (see Section 5.3.2).

(6) The proposed model to take into account γ' precipitation (Section 4.1.5 is fitted to the experimental stress strain curves up to the critical stress. The flow stress contribution of different dislocation precipitation interaction mechanisms are evaluated based on this and it is found that Orowan mechanism is activated around 1200 seconds aging time after which it quickly starts to dominate. This result is opposite to some of those reported in the literature (see Section 6.3) and can be due to experimental variations. Considering the current work alone, the hardening results presented in Chapter 5 and TEM studies presented in Chapter 6 are consistent.

(7) Upon the application of the model proposed to take into account the effect of γ' precipitation, one needs to have kinetic data of the evolution of the precipitates in hand. In the current case, some data regarding this was found in the literature. However, when the alloy is deformed in the window where γ' precipitation is possible, the data from the literature (regarding the evolution of precipitate volume fraction and radius) have to be calibrated (within this work, this calibration is performed based on TEM observations).

(8) A symmetry analysis of $\gamma - \gamma'$ is conducted and the variant number of γ' phase is reported as 1, meaning only faceted spherical or cubic γ' morphologies are possible.

(9) Within this study, only very fine (< 10 nm) or larger spherical γ' (size depends on aging time) is observed. Based on the TEM observations, after 1000 seconds of aging time; bowing, looping and cutting mechanisms are observed to be co-active.

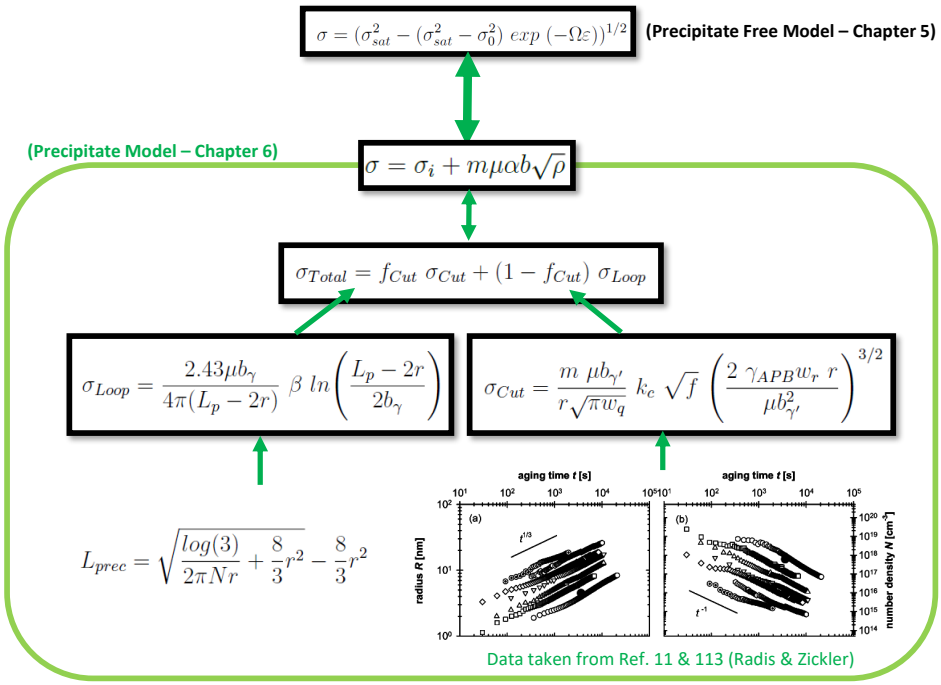

Figure 7.1: Higher level flow of the overall integration of the precipitation model.

(10) A simple sequence of the model application is as follows: One finds the hardening behavior of the precipitate free material considering Eq. 4.29. In order to include the precipitation hardening into the system one needs to evaluate Eq. 4.34 in time. The overall contribution of particle dislocation interaction mechanisms is estimated through Eq. 4.39. This in turn necessitates prior evaluation of Eqs. 4.38 and 4.37. To this end an approximate for L_{prec}; thus r and N must be evaluated. There are a number of models in the literature to estimate radius distribution and particle spacing. In this work, these are taken from the work by Radis and Zickler [11, 113]; however, calibrated as the precipitation is considered a dynamic (time/strain dependent) phenomenon. A high level flow of the described process is given in the Fig. 7.1.

7.2 Future Work

In order to further validate the models capability to predict precipitation contribution, more tests in the precipitation favoring windows must be made.

The model is applicable to other Ni-base superalloys as long as necessary modifications are made, such as estimation of D and μ (temperature dependent diffusion constant and shear modulus) and could be tried immediately on similar alloys such as Inconel 718.

Other models and experimental results for L_{prec}; thus r and N should be investigated in order to see the sensitivity of the overall behavior of the model to these.

Furthermore, in order for the model to be practically applicable to industrial processes, it should be implemented in a computational structural analysis tool by approaches described by Stockinger et al. [163] and by Huber et al. [164] or similar.

List of Publications

Publications included in this thesis

- Ozturk U., Redjaïmia A., Cabrera J. M., Calvo J. ''High Temperature Deformation Behaviour of 718PLUS^{TM}: Consideration of γ' Effects" *Materials Performance and Characterization - Special Issue on Recent Advances in Hot Deformation of Materials*, accepted.

- Ozturk U., Cabrera J. M., Calvo J. ''A Physically Based Model for High Temperature Deformation of Inconel 718Plus", in *in ASME Turbo Expo 2017 proceedings: Turbomachinery Technical Conference and Exposition (pp. V006T24A012-V006T24A012). American Society of Mechanical Engineers.*

- Ozturk U., Cabrera J. M., Calvo J. ''High temperature deformation of Inconel 718Plus" *Journal of Engineering for Gas Turbines and Power* , 139(3), 032101.

Other relevant publications and conference contributions

Journal Articles

- Paramo-Kanetas, P., Ozturk, U., Calvo, J., Cabrera, J. M., Guerrero-Mata, M., ''High-temperature deformation of delta-processed In-

conel 718." *Journal of Materials Processing Technology*255, 204-211, 2018.

Presentations

- Utkudeniz Ozturk, ''Modeling High Temperature Deformation Behaviour of Inconel 718PlusTM: Consideration of Precipitation Effects" THERMEC 2018, Paris, France, June 2018.
- Utkudeniz Ozturk, ''718Plus and its Response to Hot Forming Operations" International Network Meeting of the European School of Materials, Saarbruecken, Germany, April 2017.
- Utkudeniz Ozturk, ''High temperature deformation of Inconel 718Plus" Turbo Expo 2016, Seoul, South Korea, June 2016.
- Utkudeniz Ozturk, ''A Physically Based Model for High Temperature Deformation of Inconel 718Plus" Turbo Expo 2017, North Carolina, USA, June 2017.

Bibliography

[1] C. Sims and S. Norman, *Book Chapter, Superalloys II: High-temperature materials for aerospace and industrial power*. Wiley Publishing, 1987.

[2] C. Sims, "A history of superalloy metallurgy for superalloy metallurgists," *Superalloys, TMS; The Minerals, Metals Materials Society*, pp. 399–419, 1984.

[3] S. J. Patel, "A century of discoveries, inventors, and new nickel alloys," *The Journal of the Minerals, Metals & Materials Society*, vol. 58, no. 9, pp. 18–20, 2006.

[4] R. Decker, "The evolution of wrought age-hardenable superalloys," *The Journal of the Minerals, Metals & Materials Society*, vol. 58, no. 9, pp. 32–36, 2006.

[5] J. C. Lippold, *Welding metallurgy and weldability*. John Wiley & Sons, 2014.

[6] D. Paulonis, "Alloy 718 at Pratt Whitney historical perspective and future challenges," *Superalloys 718, 625, 706 and Various Derivatives, TMS; The Minerals, Metals Materials Society*, 2001.

[7] R. C. Reed, *The superalloys: fundamentals and applications*. Cambridge University Press, 2008.

[8] A. Jena and M. Chaturvedi, "The role of alloying elements in the design of nickel-base superalloys," *Journal of Materials Science*, vol. 19, no. 10, pp. 3121–3139, 1984.

[9] A. Taylor and R. Floyd, "The constitution of nickel-rich alloys of the nickel chromium aluminium system," *Journal of the Institute of Metals*, vol. 81, no. 9, p. 451, 1953.

[10] N. Greeves, "Chemtube3d.com/solidstate/sscu3au.htm," 2018.

[11] G. A. Zickler, R. Radis, R. Schnitzer, E. Kozeschnik, M. Stockinger, and H. Leitner, "The precipitation behavior of superalloy ati allvac 718plus," *Advanced Engineering Materials*, vol. 12, no. 3, pp. 176–183, 2010.

[12] V. Munjal and A. Ardell, "Precipitation hardening of ni-12.19 at.% al alloy single crystals," *Acta Metallurgica*, vol. 23, no. 4, pp. 513–520, 1975.

[13] N. Mott and F. N. Nabarro, "An attempt to estimate the degree of precipitation hardening, with a simple model," *Proceedings of the Physical Society*, vol. 52, no. 1, p. 86, 1940.

[14] E. Nembach and G. Neite, "Precipitation hardening of superalloys by ordered gamma prime particles," *Progress in Materials Science*, vol. 29, no. 3, pp. 177–319, 1985.

[15] R. Ricks, A. Porter, and R. Ecob, "The growth of γ' precipitates in nickel-base superalloys," *Acta Metallurgica*, vol. 31, no. 1, pp. 43–53, 1983.

[16] L. Singhal and J. Martin, "The formation of ferrite and sigma-phase in some austenitic stainless steels," *Acta Metallurgica*, vol. 16, no. 12, pp. 1441–1451, 1968.

[17] R. Ecob, A. Porter, and R. Ricks, "The measurement of precipitate/matrix lattice mismatch in nickel-base superalloys," *Scripta Metallurgica*, vol. 16, no. 9, pp. 1085–1090, 1982.

[18] R. Jeniski Jr and R. Kennedy, "Development of ati allvac® 718plus® alloy and applications," in *Second Symposium on Recent Advantages of Nb-Containing Materials in Europe*, pp. 1–10, 2006.

[19] R. Kennedy, "Allvac® 718plus: Superalloy for the next forty years," *Superalloys, TMS; The Minerals, Metals Materials Society*, vol. 718, no. 706, pp. 1–14, 2005.

[20] E. A. Loria, *Proceedings of the International Symposium on Superalloys 718, 625, 706 and Various Derivatives*. TMS; The Minerals, Metals Materials Society, 2001.

[21] C. McKamey, C. Carmichael, W. Cao, and R. Kennedy, "Creep properties of p & b -modified alloy 718," *Scripta Materialia*, vol. 38, no. 3, pp. 485 – 491, 1998.

[22] H. Sakamoto, K. Meguro, A. Tanaka, and A. Imai, "Journal de physique iv colloque c8, supplement au journal de physique iii, 5 (1995), p," *Journal de Physique III*, pp. 581–597, 1995.

[23] W. Cao and R. Kennedy, "Improving stress rupture life of alloy 718 by optimizing Al, Ti, P and B contents," *Superalloys 718, 625, 706 and Various Derivatives, TMS; The Minerals, Metals Materials Society*, pp. 455–464, 2001.

[24] W.-D. Cao, "Solidification and solid state phase transformation of allvac® 718plus^{TM} alloy," *Superalloys*, vol. 718, no. 625,706, pp. 165–177, 2005.

[25] X. Xie, G. W. J. Dong, C. Xu, W. Cao, and R. Kennedy, "Structure stability study on a newly developed nickel-base superalloy—allvac 718plus^{TM}," in *Sixth International Special Emphasis Symposium on Superalloys 718, 625, 706 and Derivatives, TMS; The Minerals, Metals Materials Society*, pp. 179–191, 2005.

[26] X. Xie, C. Xu, G. Wang, J. Dong, W. Cao, and R. Kennedy, "TTT diagram of a newly developed nickel-base superalloy-allvac 718plus^{TM}," *Superalloys 718, 625, 706 and Derivatives, TMS; The Minerals, Metals Materials Society*, 2005.

[27] R. Ding, "Grain boundary segregation in Ni-base (718 Plus) superalloy," *Materials Science and Technology*, vol. 26, no. 1, pp. 36–40, 2010.

[28] W. Cao and R. Kennedy, "Role of chemistry in 718-type alloys–Allvac® 718plus alloy development," *Superalloys 2004, TMS; The Minerals, Metals Materials Society*, pp. 91–99, 2004.

[29] C. Stotter, C. Sommitsch, J. Wagner, H. Leitner, I. Letofsky-Papst, G. A. Zickler, W. Prantl, and M. Stockinger, "Characterization of δ-phase in superalloy allvac 718plustm," *International Journal of Materials Research*, vol. 99, no. 4, pp. 376–380, 2008.

[30] E. Pickering, H. Mathur, A. Bhowmik, O. Messé, J. Barnard, M. Hardy, R. Krakow, K. Loehnert, H. Stone, and C. Rae, "Grain-boundary precipitation in allvac 718plus," *Acta Materialia*, vol. 60, no. 6-7, pp. 2757–2769, 2012.

[31] L. Whitmore, H. Leitner, E. Povoden-Karadeniz, R. Radis, and M. Stockinger, "Transmission electron microscopy of single and double aged 718plus superalloy," *Materials Science and Engineering: A*, vol. 534, pp. 413–423, 2012.

[32] J. Cabrera, J. Ponce, and J. Prado, "Modeling thermomechanical processing of austenite," *Journal of Materials Processing Technology*, vol. 143–144, pp. 403 – 409, 2003. Proceedings of the International Conference on the Advanced Materials Processing Technology.

[33] D. Raabe, "Recovery and recrystallization: phenomena, physics, models, simulation," in *Physical Metallurgy*, pp. 2291–2397, Elsevier, 2014.

[34] F. J. Humphreys and M. Hatherly, *Recrystallization and related annealing phenomena*. Elsevier, 2012.

[35] P. Wilson, *Recent developments in the study of recrystallization*. IntechOpen, 2013.

[36] S. Medeiros, Y. Prasad, W. G. Frazier, and R. Srinivasan, "Microstructural modeling of metadynamic recrystallization in hot working of IN 718 superalloy," *Materials Science and Engineering: A*, vol. 293, no. 1-2, pp. 198–207, 2000.

[37] A. Porter and B. Ralph, "The recrystallization of Ni-base superalloys," *Journal of Materials Science*, vol. 16, no. 3, pp. 707–713, 1981.

[38] E. Mittemeijer, *Fundamentals of Materials Science: The Microstructure–Property Relationship Using Metals as Model Systems*. Springer, Berlin, 2010.

[39] R. Doherty, D. Hughes, F. Humphreys, J. Jonas, D. J. Jensen, M. Kassner, W. King, T. McNelley, H. McQueen, and A. Rollett, "Current issues in recrystallization: a review," *Materials Science and Engineering: A*, vol. 238, no. 2, pp. 219–274, 1997.

[40] H. McQueen, "Development of dynamic recrystallization theory," *Materials Science and Engineering: A*, vol. 387, pp. 203–208, 2004.

[41] T. Sakai, A. Belyakov, R. Kaibyshev, H. Miura, and J. J. Jonas, "Dynamic and post-dynamic recrystallization under hot, cold and severe plastic deformation conditions," *Progress in Materials Science*, vol. 60, pp. 130–207, 2014.

[42] T. Sakai and J. J. Jonas, "Overview no. 35 dynamic recrystallization: mechanical and microstructural considerations," *Acta Metallurgica*, vol. 32, no. 2, pp. 189–209, 1984.

[43] M. Luton and C. Sellars, "Dynamic recrystallization in nickel and Ni-Fe alloys during high temperature deformation," *Acta Metallurgica*, vol. 17, no. 8, pp. 1033–1043, 1969.

[44] A. Dehghan-Manshadi, M. R. Barnett, and P. Hodgson, "Hot deformation and recrystallization of austenitic stainless steel: Part i. dynamic recrystallization," *Metallurgical and Materials Transactions A*, vol. 39, no. 6, pp. 1359–1370, 2008.

[45] L. Blaz, T. Sakai, and J. Jonas, "Effect of initial grain size on dynamic recrystallization of Cu," *Metal Science*, vol. 17, no. 12, pp. 609–616, 1983.

[46] D. Ponge and G. Gottstein, "Necklace formation during dynamic recrystallization: mechanisms and impact on flow behavior," *Acta Materialia*, vol. 46, no. 1, pp. 69–80, 1998.

[47] K. Huang and R. Logé, "A review of dynamic recrystallization phenomena in metallic materials," *Materials & Design*, vol. 111, pp. 548–574, 2016.

[48] M. El Wahabi, L. Gavard, F. Montheillet, J. Cabrera, and J. Prado, "Effect of initial grain size on dynamic recrystallization in high purity austenitic stainless steels," *Acta Materialia*, vol. 53, no. 17, pp. 4605–4612, 2005.

[49] A. Dehghan-Manshadi and P. Hodgson, "Dependency of recrystallization mechanism to the initial grain size," *Metallurgical and Materials Transactions A*, vol. 39, no. 12, p. 2830, 2008.

[50] M. Ohashi, T. Endo, and T. Sakai, "Effect of initial grain size on dynamic recrystallization of pure nickel," *Journal of the Japan Institute of Metals*, vol. 54, no. 4, pp. 435–441, 1990.

[51] A. Fernández, P. Uranga, B. López, and J. Rodriguez-Ibabe, "Dynamic recrystallization behavior covering a wide austenite grain

size range in Nb and Nb–Ti microalloyed steels," *Materials Science and Engineering: A*, vol. 361, no. 1-2, pp. 367–376, 2003.

[52] H.-T. Lee and W.-H. Hou, "Influence of precipitated phase formation on recrystallization behavior of superalloy 718," *Materials Transactions*, vol. 53, no. 7, pp. 1334–1342, 2012.

[53] P. A. Beck and P. R. Sperry, "Strain induced grain boundary migration in high purity aluminum," *Journal of Applied Physics*, vol. 21, no. 2, pp. 150–152, 1950.

[54] R. Sandström and R. Lagneborg, "A controlling factor for dynamic recrystallisation," *Scripta Metallurgica*, vol. 9, no. 1, pp. 59–65, 1975.

[55] J. W. Christian, *The theory of transformations in metals and alloys*. Newnes, 2002.

[56] R. Honeycombe and R. Pethen, "Dynamic recrystallization," *Journal of the Less Common Metals*, vol. 28, no. 2, pp. 201–212, 1972.

[57] P. Bernard, S. Bag, K. Huang, and R. E. Logé, "A two-site mean field model of discontinuous dynamic recrystallization," *Materials Science and Engineering: A*, vol. 528, no. 24, pp. 7357–7367, 2011.

[58] O. Beltran, K. Huang, and R. E. Logé, "A mean field model of dynamic and post-dynamic recrystallization predicting kinetics, grain size and flow stress," *Computational Materials Science*, vol. 102, pp. 293–303, 2015.

[59] M. Drury and F. Humphreys, "The development of microstructure in al-5% mg during high temperature deformation," *Acta Metallurgica*, vol. 34, no. 11, pp. 2259–2271, 1986.

[60] A. Wusatowska-Sarnek, H. Miura, and T. Sakai, "Nucleation and microtexture development under dynamic recrystallization of copper," *Materials Science and Engineering: A*, vol. 323, no. 1-2, pp. 177–186, 2002.

[61] H. Miura, H. Aoyama, and T. Sakai, "Effect of grain-boundary misorientation on dynamic recrystallization of cu–si bicrystals," *Journal of the Japan Institute of Metals(Japan)*, vol. 58, no. 3, pp. 267–275, 1994.

[62] J. Calvo, M. Penalva, and J. M. Cabrera, "Characterization of strain-induced precipitation in inconel 718 superalloy," *Journal of Materials Engineering and Performance*, vol. 25, no. 8, pp. 3409–3417, 2016.

[63] A. Thomas, M. El-Wahabi, J. Cabrera, and J. Prado, "High temperature deformation of inconel 718," *Journal of Materials Processing Technology*, vol. 177, no. 1, pp. 469–472, 2006.

[64] W. Liu, M. Yao, and Z. Chen, "Effect of cold rolling on the precipitation behavior of δ phase in inconel 718," *Metallurgical and Materials Transactions A*, vol. 30, no. 1, pp. 31–40, 1999.

[65] Y. Mei, Y. Liu, C. Liu, C. Li, L. Yu, Q. Guo, and H. Li, "Effects of cold rolling on the precipitation kinetics and the morphology evolution of intermediate phases in inconel 718 alloy," *Journal of Alloys and Compounds*, vol. 649, pp. 949–960, 2015.

[66] H. Monajati, F. Zarandi, M. Jahazi, and S. Yue, "Strain induced γ' precipitation in nickel base superalloy udimet 720 using a stress relaxation based technique," *Scripta Materialia*, vol. 52, no. 8, pp. 771–776, 2005.

[67] C. Chen and J. Yang, "Nano-carbide precipitation strengthening in a newly developed HSLA steel," *Yoke and. Corp.*, 2006.

[68] S. Azadian, L.-Y. Wei, and R. Warren, "Delta phase precipitation in inconel 718," *Materials Characterization*, vol. 53, no. 1, pp. 7–16, 2004.

[69] Y. Huang and T. G. Langdon, "The evolution of delta-phase in a superplastic inconel 718 alloy," *Journal of Materials Science*, vol. 42, no. 2, pp. 421–427, 2007.

[70] D. Cai, W. Zhang, P. Nie, W. Liu, and M. Yao, "Dissolution kinetics of δ phase and its influence on the notch sensitivity of inconel 718," *Materials Characterization*, vol. 58, no. 3, pp. 220–225, 2007.

[71] E. McDevitt, "Effect of temperature and strain during forging on subsequent delta phase precipitation during solution annealing in ati 718plus alloy," in *7th International Symposium on Superalloy*, vol. 718, pp. 307–319, 2010.

[72] O. Covarrubias, "Microstructural and mechanical effects of thermo-mechanical processing on ati 718plus® contoured rings," in *Advanced Materials Research*, vol. 278, pp. 271–276, Trans Tech Publ, 2011.

[73] O. Messé, J. Barnard, E. Pickering, P. Midgley, and C. Rae, "On the precipitation of delta phase in allvac® 718plus," *Philosophical Magazine*, vol. 94, no. 10, pp. 1132–1152, 2014.

[74] A. Casanova, N. Martín-Piris, M. Hardy, and C. Rae, "Evolution of secondary phases in alloy ati 718plus^{TM} during processing," in *MATEC Web of Conferences*, vol. 14, p. 09003, EDP Sciences, 2014.

[75] A. Casanova, M. Hardy, and C. Rae, "Morphology and kinetics of grain boundary precipitation in alloy ati 718plus®," in *8th International Symposium on Superalloy 718 and Derivatives*, pp. 573–586, Wiley Online Library, 2014.

[76] R. Bullough, R. Newman, J. Wakefield, and J. Willis, "Precipitation on a dislocation," *Nature*, vol. 183, no. 4653, p. 34, 1959.

[77] M. Zhang, J. Dong, Z. Bi, Q. Yu, and Y. Zhang, "The effect of primary gamma prime distribution on grain growth behavior of GH720Li alloy," *Superalloy 718 and Derivatives*, pp. 766–779, 2010.

[78] L. Brown and R. Ham, *Strengthening Mechanisms in Crystals*. Wiley, 1971.

[79] H. Gleiter and E. Hornbogen, "Precipitation hardening by coherent particles," *Materials Science and Engineering*, vol. 2, no. 6, pp. 285–302, 1968.

[80] E. Orowan, "Discussion in the symposium on internal stresses in metals and alloys, inst," *Metals, London*, vol. 451, 1948.

[81] J. Fisher, E. W. Hart, and R. Pry, "The hardening of metal crystals by precipitate particles," *Acta Metallurgica*, vol. 1, no. 3, pp. 336–339, 1953.

[82] M. Ahmadi, E. Povoden-Karadeniz, L. Whitmore, M. Stockinger, A. Falahati, and E. Kozeschnik, "Yield strength prediction in ni-base alloy 718plus based on thermo-kinetic precipitation simulation," *Materials Science and Engineering: A*, vol. 608, pp. 114–122, 2014.

[83] R. W. Hertzberg, *Deformation and fracture mechanics of engineering materials*. Wiley, 1989.

[84] J. Jonas, R. Holt, and C. Coleman, "Plastic stability in tension and compression," *Acta Metallurgica*, vol. 24, no. 10, pp. 911–918, 1976.

[85] J. M. Cabrera, *Caracterización mecánico-metalúrgica de la conformación en caliente del acero microaleado de medio carbono 38 MnSiVS5*. Universitat Politècnica de Catalunya, 1995.

[86] P. Páramo-Kañetas, U. Özturk, J. Calvo, J. M. Cabrera, and M. Guerrero-Mata, "High-temperature deformation of delta-processed inconel 718," *Journal of Materials Processing Technology*, vol. 255, pp. 204–211, 2018.

[87] J. Jonas and I. Weiss, "Effect of precipitation on recrystallization in microalloyed steels," *Metal Science*, vol. 13, no. 3-4, pp. 238–245, 1979.

[88] U. Ozturk, J. M. Cabrera, and J. Calvo, "High-temperature deformation of inconel 718plustm," *Journal of Engineering for Gas Turbines and Power*, vol. 139, no. 3, p. 032101, 2017.

[89] D. Srinivasan, L. U. Lawless, and E. A. Ott, "Experimental determination of TTT diagram for alloy 718plus^{TM}," *Superalloys, TMS; The Minerals, Metals Materials Society*, pp. 759–768, 2012.

[90] C. B. Carter and D. B. Williams, *Transmission electron microscopy: Diffraction, imaging, and spectrometry*. Springer, 2016.

[91] M. Klinger and A. Jäger, "Crystallographic tool box (crystbox): automated tools for transmission electron microscopists and crystallographers," *Journal of Applied Crystallography*, vol. 48, no. 6, pp. 2012–2018, 2015.

[92] U. Kocks and H. Mecking, "Physics and phenomenology of strain hardening: the fcc case," *Progress in Materials Science*, vol. 48, no. 3, pp. 171–273, 2003.

[93] A. Seeger, J. Diehl, S. Mader, and H. Rebstock, "Work-hardening and work-softening of face-centred cubic metal crystals," *Philosophical Magazine*, vol. 2, no. 15, pp. 323–350, 1957.

[94] Z. Basinski, "Thermally activated glide in face-centred cubic metals and its application to the theory of strain hardening," *Philosophical Magazine*, vol. 4, no. 40, pp. 393–432, 1959.

[95] U. Kocks, "A statistical theory of flow stress and work-hardening," *Philosophical Magazine*, vol. 13, no. 123, pp. 541–566, 1966.

[96] Y. Bergström, "A dislocation model for the stress-strain behaviour of polycrystalline α-fe with special emphasis on the variation of the densities of mobile and immobile dislocations," *Materials Science and Engineering*, vol. 5, no. 4, pp. 193–200, 1970.

[97] W. Roberts and Y. Bergström, "The stress-strain behaviour of single crystals and polycrystals of face-centered cubic metals—a new dislocation treatment," *Acta Metallurgica*, vol. 21, no. 4, pp. 457–469, 1973.

[98] H. Mecking and U. Kocks, "Kinetics of flow and strain-hardening," *Acta Metallurgica*, vol. 29, no. 11, pp. 1865–1875, 1981.

[99] Y. Bergström and H. Hallén, "An improved dislocation model for the stress-strain behaviour of polycrystalline α-fe," *Materials Science and Engineering*, vol. 55, no. 1, pp. 49–61, 1982.

[100] N. M. Ghoniem, J. Matthews, and R. J. Amodeo, *A dislocation model for creep in engineering materials*. Institute of Plasma and Fusion Research, University of California, Los Angeles, 1989.

[101] U. Kocks, "Laws for work-hardening and low-temperature creep," *Journal of Engineering Materials and Technology*, vol. 98, no. 1, pp. 76–85, 1976.

[102] W. Roberts, "Dynamic changes that occur during hot working and their significance regarding microstructural development and hot workability," *American Society for Metals,*, pp. 109–184, 1984.

[103] J. J. Jonas, X. Quelennec, L. Jiang, and E. Martin, "The avrami kinetics of dynamic recrystallization," *Acta Materialia*, vol. 57, no. 9, pp. 2748–2756, 2009.

[104] X. Quelennec, N. Bozzolo, J. J. Jonas, and R. Loge, "A new approach to modeling the flow curve of hot deformed austenite," *ISIJ International*, vol. 51, no. 6, pp. 945–950, 2011.

[105] D. Bailey and W. Flanagan, "The relationship between dislocation density and flow stress in materials deforming by a peierls-nabarro mechanism," *PhilosophicalMagazine*, vol. 15, no. 133, pp. 43–49, 1967.

[106] G. Engberg and L. Lissel, "A physically based microstructure model for predicting the microstructural evolution of a C-Mn steel during and after hot deformation," *Steel Res Int*, vol. 79, no. 1, pp. 47–58, 2008.

[107] L. Lissel, G. Engberg, and U. Borggren, "Modeling precipitation and its effect on recrystallization during hot strip rolling of Nb steels," in *3rd Int. Conf. on Thermomechanical Processing of Steels, Padua, Italy, 12-13 september, 2008*, 2008.

[108] L. Bäcke, *Modeling the microstructural evolution during hot deformation of microalloyed steels*. PhD thesis, KTH, 2009.

[109] B. Dutta, E. Palmiere, and C. Sellars, "Modelling the kinetics of strain induced precipitation in Nb microalloyed steels," *Acta Materialia*, vol. 49, no. 5, pp. 785–794, 2001.

[110] M. Fisk, A. Lundbäck, J. Andersson, and L.-E. Lindgren, "Finite element analysis using a dislocation density based flow stress model coupled with model for precipitate evolution," in *International Symposium on Superalloy 718 and Derivatives: 28/09/2014-01/10/2014*, pp. 155–168, John Wiley & Sons, 2014.

[111] Y. Bergström, Y. Granbom, and D. Sterkenburg, "A dislocation-based theory for the deformation hardening behavior of dp steels: impact of martensite content and ferrite grain size," *Journal of Metallurgy*, vol. 2010, 2010.

[112] B. Sonderegger, I. Holzer, E. Kozeschnik, and C. Sommitsch, "Particle distance distributions and their effect on precipitation strengthening," *Computer Methods in Materials Science*, vol. 11, no. 1, pp. 148–153, 2011.

[113] R. Radis, G. A. Zickler, M. Stockinger, C. Sommitsch, and E. Kozeschnik, "Interaction of the precipitation kinetics of δ and γ'phases in nickel-base superalloy ati allvac® 718plustm," in *Materials Science Forum*, vol. 638, pp. 2712–2717, Trans Tech Publ., 2010.

[114] G. A. Zickler, R. Schnitzer, R. Radis, R. Hochfellner, R. Schweins, M. Stockinger, and H. Leitner, "Microstructure and mechanical properties of the superalloy ATI Allvac® 718Plus," *Materials Science and Engineering: A*, vol. 523, no. 1, pp. 295–303, 2009.

[115] V. Mohles, D. Rönnpagel, and E. Nembach, "Simulation of dislocation glide in precipitation hardened materials," *Computational Materials Science*, vol. 16, no. 1-4, pp. 144–150, 1999.

[116] C. M. Sellars and W. M. Tegart, "Relationship between strength and structure in deformation at elevated temperatures," *Mem Sci Rev Met*, vol. 63, no. 9, 1966.

[117] C. Sellars and W. McG, "Tegart. on the mechanism of deformation," *Acta Metallurgica*, vol. 14, pp. 1136–1138, 1966.

[118] W. F. Hosford and R. M. Caddell, *Metal forming: mechanics and metallurgy*. Cambridge University Press, 2011.

[119] J. Cabrera, J. Jonas, and J. Prado, "Flow behaviour of medium carbon microalloyed steel under hot working conditions," *Materials Science and Technology*, vol. 12, no. 7, pp. 579–585, 1996.

[120] H. J. Frost and M. F. Ashby, *Deformation mechanism maps: the plasticity and creep of metals and ceramics*. Pergamon press, 1982.

[121] J. Sah, G. Richardson, and C. Sellars, "Quantitative correlation between high temperature strength and the kinetics of dynamic recrystallization," *Indian J. Technol.*, vol. 11, no. 10, pp. 445–452, 1973.

[122] W. Roberts, H. Boden, and B. Ahlblom, "Dynamic recrystallization kinetics," *Metal Science*, vol. 13, no. 3-4, pp. 195–205, 1979.

[123] F. Montheillet, "Modelling discontinuous and continuous dynamic recrystallization," *Materials Transactions, JIM*, vol. 41, no. 1, pp. 109–112, 2000.

[124] H. Stüwe and B. Ortner, "Recrystallization in hot working and creep," *Metal Science*, vol. 8, no. 1, pp. 161–167, 1974.

[125] S. Brown and J. Wlassich, "Application of invariant set theory to," *Metallurgical Transactions A*, vol. 23, no. 8, pp. 2091–2103, 1992.

[126] X.-M. Chen, Y. Lin, D.-X. Wen, J.-L. Zhang, and M. He, "Dynamic recrystallization behavior of a typical Ni-based superalloy during hot deformation," *Materials & Design*, vol. 57, pp. 568–577, 2014.

[127] D. Cram, H. Zurob, Y. Brechet, and C. Hutchinson, "Modelling discontinuous dynamic recrystallization using a physically based model for nucleation," *Acta Materialia*, vol. 57, no. 17, pp. 5218–5228, 2009.

[128] F. Chen, K. Qi, Z. Cui, and X. Lai, "Modeling the dynamic recrystallization in austenitic stainless steel using cellular automaton method," *Computational Materials Science*, vol. 83, pp. 331–340, 2014.

[129] S. Rahimi, M. King, and C. Dumont, "Stress relaxation behaviour in in718 nickel based superalloy during ageing heat treatments," *Materials Science and Engineering: A*, vol. 708, pp. 563–573, 2017.

[130] Z. Wang, A. D. Stoica, D. Ma, and A. M. Beese, "Stress relaxation in a nickel-base superalloy at elevated temperatures with in situ neutron diffraction characterization: Application to additive manufacturing," *Materials Science and Engineering: A*, vol. 714, pp. 75–83, 2018.

[131] S.-B. Kim, J. Shackleton, M. Preuss, P. Withers, A. Evans, and G. Bruno, "Stress relaxation of shot-peened udimet 720li under solely elevated-temperature exposure and under isothermal fatigue," *Metallurgical and Materials Transactions A*, vol. 36, no. 11, pp. 3041–3053, 2005.

[132] H. Mirzadeh, J. M. Cabrera, and A. Najafizadeh, "Modeling and prediction of hot deformation flow curves," *Metallurgical and Materials Transactions A*, vol. 43, no. 1, pp. 108–123, 2012.

[133] H. Mirzadeh, J. Cabrera, J. Prado, and A. Najafizadeh, "Hot deformation behavior of a medium carbon microalloyed steel," *Materials Science and Engineering: A*, vol. 528, no. 10, pp. 3876–3882, 2011.

[134] H. Mirzadeh, J. M. Cabrera, and A. Najafizadeh, "Constitutive relationships for hot deformation of austenite," *Acta Materialia*, vol. 59, no. 16, pp. 6441–6448, 2011.

[135] L. M. Suave, J. Cormier, P. Villechaise, A. Soula, Z. Hervier, D. Bertheau, and J. Laigo, "Microstructural evolutions during thermal aging of alloy 625: impact of temperature and forming process," *Metallurgical and Materials Transactions A*, vol. 45, no. 7, pp. 2963–2982, 2014.

[136] L. M. Suave, J. Cormier, D. Bertheau, P. Villechaise, A. Soula, Z. Hervier, and F. Hamon, "High temperature low cycle fatigue properties of alloy 625," *Materials Science and Engineering: A*, vol. 650, pp. 161–170, 2016.

[137] A. Laasraoui and J. Jonas, "Prediction of steel flow stresses at high temperatures and strain rates," *Metallurgical Transactions A*, vol. 22, no. 7, pp. 1545–1558, 1991.

[138] M. El Wahabi, J. Cabrera, and J. Prado, "Hot working of two aisi 304 steels: a comparative study," *Materials Science and Engineering: A*, vol. 343, no. 1, pp. 116–125, 2003.

[139] Y. Tan, Y. Ma, and F. Zhao, "Hot deformation behavior and constitutive modeling of fine grained inconel 718 superalloy," *Journal of Alloys and Compounds*, vol. 741, pp. 85–96, 2018.

[140] Y. Lin, F.-Q. Nong, X.-M. Chen, D.-D. Chen, and M.-S. Chen, "Microstructural evolution and constitutive models to predict hot deformation behaviors of a Ni-based superalloy," *Vacuum*, vol. 137, pp. 104–114, 2017.

[141] Y.-S. Na, J.-T. Yeom, N.-K. Park, and J.-Y. Lee, "Simulation of microstructures for alloy 718 blade forging using 3d fem simulator," *Journal of Materials Processing Technology*, vol. 141, no. 3, pp. 337–342, 2003.

[142] D. Furrer, R. Goetz, and G. Shen, "Modeling and simulation of alloy 718 microstructure and mechanical properties," in *Proceedings of the 7th international symposium on Superalloy*, vol. 718, 2010.

[143] D. Huang, W. Wu, D. Lambert, and S. Semiatin, "Computer simulation of microstructure evolution during hot forging of waspaloy and nickel alloy 718," in *Proceedings of Symposium: Microstructure Modeling and Prediction During Thermomechanical Processing, Indianapolis, November*, pp. 4–8, 2001.

[144] A. Loyda, G. Hernández-Muñoz, L. Reyes, and P. Zambrano-Robledo, "Microstructure modeling of a ni-fe-based superalloy during the rotary forging process," *Journal of Materials Engineering and Performance*, vol. 25, no. 6, pp. 2128–2137, 2016.

[145] M. Militzer, W. Sun, and J. J. Jonas, "Effect of deformation-induced vacancies on recrystallization," in *Materials Science Forum*, vol. 113, pp. 163–168, Trans Mech Publ, 1993.

[146] M. Condat and B. Décamps, "Shearing of γ' precipitates by single a/2$< 110 >$ matrix dislocations in a γ/γ' ni-based superalloy," *Scripta Metallurgica*, vol. 21, no. 5, pp. 607–612, 1987.

[147] B. Decamps, S. Raujol, A. Coujou, F. Pettinari-Sturmel, N. Clement, D. Locq, and P. Caron, "On the shearing mechanism of γ' precipitates by a single (a/6) $< 112 >$ shockley partial in ni-based superalloys," *Philosophical Magazine*, vol. 84, no. 1, pp. 91–107, 2004.

[148] M. Whelan and P. Hirsch, "Electron diffraction from crystals containing stacking faults: I," *Philosophical Magazine*, vol. 2, no. 21, pp. 1121–1142, 1957.

[149] P. Bellon, J. Chevalier, E. Augarde, J. Andre, and G. Martin, "Substrate-driven ordering microstructure in ga x in1- x p alloys," *Journal of Applied Physics*, vol. 66, no. 6, pp. 2388–2394, 1989.

[150] G. Van Tendeloo, O. Lebedev, M. Hervieu, and B. Raveau, "Structure and microstructure of colossal magnetoresistant materials," *Reports on Progress in Physics*, vol. 67, no. 8, p. 1315, 2004.

[151] O. Skiba, A. Redjaimia, J. Dulcy, J. Ghanbaja, G. Marcos, N. Caldeira-Meulnotte, and T. Czerwiec, "A proper assessment of TEM diffraction patterns originating from Cr N nitrides in a ferritic matrix," *Materials Characterization*, vol. 144, pp. 671–677, 2018.

[152] M. Gouné, A. Redjaïmia, T. Belmonte, and H. Michel, "Identification and characterization of a novel Mn–N nitride formed in Fe–Mn–N alloy," *Journal of applied crystallography*, vol. 36, no. 1, pp. 103–108, 2003.

[153] A. Redjaimia, A. Proult, P. Donnadieu, and J. Morniroli, "Morphology, crystallography and defects of the intermetallic χ-phase precipitated in a duplex ($\delta+\ \gamma$) stainless steel," *Journal of Materials Science*, vol. 39, no. 7, pp. 2371–2386, 2004.

[154] A. Mateo, L. Llanes, M. Anglada, A. Redjaimia, and G. Metauer, "Characterization of the intermetallic g-phase in an AISI 329 duplex stainless steel," *Journal of Materials Science*, vol. 32, no. 17, pp. 4533–4540, 1997.

[155] K. Kaneko, K. Inoke, K. Sato, K. Kitawaki, H. Higashida, I. Arslan, and P. Midgley, "Tem characterization of ge precipitates in an Al–1.6 at% Ge alloy," *Ultramicroscopy*, vol. 108, no. 3, pp. 210–220, 2008.

[156] W. Cao and G. R. Barsch, "Landau-ginzburg model of interphase boundaries in improper ferroelastic perovskites of d 4 h 18 symmetry," *Physical Review B*, vol. 41, no. 7, p. 4334, 1990.

[157] D.-X. Wen, Y. Lin, J. Chen, X.-M. Chen, J.-L. Zhang, Y.-J. Liang, and L.-T. Li, "Work-hardening behaviors of typical solution-treated and aged ni-based superalloys during hot deformation," *Journal of Alloys and Compounds*, vol. 618, pp. 372–379, 2015.

[158] A. Najafizadeh and J. J. Jonas, "Predicting the critical stress for initiation of dynamic recrystallization," *ISIJ International*, vol. 46, no. 11, pp. 1679–1684, 2006.

[159] P. Gong, E. J. Palmiere, and W. M. Rainforth, "Characterisation of strain-induced precipitation behaviour in microalloyed steels during thermomechanical controlled processing," *Materials Characterization*, vol. 124, pp. 83–89, 2017.

[160] J. Andersson, G. Sjöberg, L. Viskari, and M. Chaturvedi, "Effect of different solution heat treatments on hot ductility of superalloys-part 2–Allvac 718plus," *Materials Science and Technology*, vol. 28, no. 6, pp. 733–741, 2012.

[161] Y. Han and M. Chaturvedi, "A study of back stress during creep deformation of a superalloy inconel 718," *Materials science and Engineering*, vol. 85, pp. 59–65, 1987.

[162] M. Sundararaman, P. Mukhopadhyay, and S. Banerjee, "Deformation behaviour of γ'' strengthened inconel 718," *Acta Metallurgica*, vol. 36, no. 4, pp. 847–864, 1988.

[163] M. Stockinger, *Mikrostrukturelle Simulation des Gesenkschmiedens von Nickelbasis-Legierungen (Microstructural Simulation of Die Forging of Nickel Base Alloys; in German)*. PhD thesis, Ph. D. Thesis, Technical University of Graz, 2003.

[164] D. Huber, *Untersuchung des meta–dynamischen Rekristallisationsverhaltens der Nickelbasislegierung Allvac 718Plus und Optimierung der numerischen Gefügesimulation in DEFORM 2D*. PhD thesis, Ph. D. Thesis, Montanuniversität Leoben, 2009.